The Dissertation Committee for Varun Pattani Certifies that this is the approved version of the following dissertation:

Understanding Cell Death Response to Gold Nanoparticle-mediated Photothermal Therapy in 2D and 3D *in vitro* Tumor Models for Improving Cancer Therapy

Committee:

James W. Tunnell, Supervisor

Andrew Dunn

Kenneth Diller

John Pearce

Sunil Krishnan

Understanding Cell Death Response to Gold Nanoparticle-mediated Photothermal Therapy in 2D and 3D *in vitro* Tumor Models for Improving Cancer Therapy

by

Varun Pattani, B.S., M.S.E.

Dissertation

Presented to the Faculty of the Graduate School of

The University of Texas at Austin

in Partial Fulfillment

of the Requirements

for the Degree of

Doctor of Philosophy

The University of Texas at Austin

December 2013

Dedication

To my Mom, Dad, and Sister

Acknowledgements

I would like to thank my family including my sister, Kiran Pattani, my mother, Kalyani Pattani, and my father, Paresh Pattani. I appreciate their strong encouragement, support and love throughout the years while keeping me grounded and modest, and especially for teaching me the strong morals and values that make me who I am today. They instilled in me the love for education and knowledge, as well as the value of being dedicated, perseverant and a well-rounded individual, which inspired me to spend the considerable amount of time I spent getting my doctorate.

I would like to thank my friends from high school (especially Alex Willard, Ann Kennedy, Chris Verlinden, and Isaac Zaworksi) and Cornell (especially Ben Pelleg, James Swirhun, Lee Stein and Preeti Nalavade) for their support from afar, advice and most of all for keeping things in perspective. I would also like to thank my friends here in Austin from fellow graduate students at The University of Texas (especially Tushar Sharma, Sam Lim, and Shams Kazmi) for their ongoing support as we went through this journey together. In addition, I would like to thank the ultimate frisbee teams here at UT and locally (especially Abhi Kudva, Warren Hornbuckle, Jacob Lohman, Matthew Bierschenk, Hayley Manning, Suede Kam and Stephanie Redfern) for giving me an output for my energy and getting me in shape and, thus, keeping me sane, being a strong support group outside of academia, and also for building my teamwork and coaching skills.

I would like to thank my previous advisor, Dr. Tania Vu at OHSU, from the lab I worked in during my undergraduate degree, because the work we did there inspired me to

go into graduate school and continue working in research. Similarly, I would like to thank all of my current and past colleagues in the Biophotonics Lab for their help and advice throughout especially from Priya Puvanakrishnan and Jaesook Park for training me and helping me along in the fields of nanotechnology and cell culturing. Also, I would like to thank Narasimhan Rajaram, Sheldon Bish, Manu Sharma, Tim Erickson, Brandon Nichols, Bin Yang, Ricky Hennessey, and Sam Lim for their help in the laboratory and putting up with any problems that occurred. Additionally, I would like to acknowledge our collaborators, Nanospectra Biosciences Inc., for their support in providing the nanoparticles and biofunctionalization, Dr. Pengyu Ren here at UT, Dr. Colin Hessel and Dr. Brian Korgel in Chemical Engineering at UT, and Dr. Sunil Krishnan at MD Anderson. Also I would like to thank my committee for their help and guidance and taking their time to read and assess my project, Dr. Andrew Dunn, Dr. John Pearce, Dr. Kenneth Diller, and Dr. Sunil Krishnan.

Finally and importantly, I am extremely grateful to my supervisor, Dr. James W. Tunnell, for his invaluable guidance and support during the hard times when it seemed like there was no progress, and through the good times when we were able to obtain meaningful results. I really appreciate all the assistance, advice and the brainstorming sessions regarding research and personal life. Overall, Dr. Tunnell has been an extremely great mentor helping me tremendously and I believe we will have a great relationship continuing on into the future.

Understanding Cell Death Response to Gold Nanoparticle-mediated Photothermal Therapy in 2D and 3D *in vitro* Tumor Models for Improving Cancer Therapy

Varun Pattani, PhD

The University of Texas at Austin, 2013

Supervisor: James W. Tunnell

Gold nanoparticles, a class of plasmonic nanoparticle, have increasingly been explored as an imaging and therapeutic agent to treat cancer due to their characteristic surface plasmon resonance phenomenon and penchant for tumor accumulation. Photothermal therapy has been shown as a promising cancer treatment by delivering heat specifically to the tumor site via gold nanoparticles. In this study, we demonstrate that gold nanorod (GNR)-mediated photothermal therapy can be more effective through the understanding of cell death mechanisms. By targeting GNRs to various cellular localizations, we explored the association of GNR localization with cell death pathway response to photothermal therapy. Furthermore, we compared the 2D monolayer experiments with 3D *in vitro* tumor models, multicellular tumor spheroids (MCTS), to mimic the structure of *in vivo* tumors. With MCTS, we evaluated the cell death response with GNRs distributed only on the periphery, as seen in typical *in vivo* studies, and distributed evenly throughout the tumor.

We demonstrated that GNR localization influences the cell death response to photothermal therapy by showing the power threshold necessary to induce significant apoptotic and necrotic increases was lower for internalized GNRs than membrane-bound

GNRs. Furthermore, apoptosis was found to increase with increasing laser power until the necrotic threshold and decreased above it, as necrosis became the dominant cell death pathway response. A similar trend was revealed with the 3D MCTS; however, the overall cell death percentages were lower, most likely due to the upregulated cell repair response and varied GNR distributions due to the presence of cell-cell and cell-matrix interactions. Furthermore, the uniformly distributed GNRs induced more apoptosis and necrosis than GNRs located in the MCTS periphery. In conclusion, we quantitatively analyzed the cell death pathway response to GNR-mediated photothermal therapy to establish that it has some dependence on GNR localization and distribution to gain a more thorough understanding of this response for photothermal therapy optimization.

Table of Contents

List of Figures

Chapter 1: Introduction

1.1 MOTIVATION

Scientists and physicians have long sought a cure for cancer, the second leading cause of death in the United States. This goal remains elusive despite decades of oncological research. In this study, our focus is on colon cancer, which has a low survival rate. It has been recently estimated that 142,820 men and women will be diagnosed with colorectal cancer in the year 2013 alone; 50,830 of which will die of the disease (*1*). The volatility and unpredictability of cancer contributes to the difficulty in treating the disease effectively. Furthermore, all current techniques have potentially devastating side effects. The most prevalent approved methods of treating cancer - chemotherapy, radiation, and surgery - have not improved cancer survival rates significantly over the past 10 years due to their limitations in convenience and effectiveness (*2*). Both chemotherapy and radiation therapy target all highly proliferating cells within the body affecting not only cancer cells but also cells in hair follicles, gastrointestinal epithelium, and immune system. Radiation therapy is considerably more localized; however, chemotherapy is systemic and affects the whole body (*3-5*). As such, there is a great need for a therapeutic technique that can be utilized for many different types of cancer without causing significant side effects. The need for a minimally invasive, non-surgical, method of cancer therapy is currently a widely researched topic. Fortunately, this has increased the emphasis on developing more targeted and patient compliant treatments, such as gold nanoparticle-mediated photothermal therapy.

Thermal therapy, induced hyperthermia, has shown potential for the non-invasive treatment of cancer. Current hyperthermia-based procedures, including microwave and radio frequency heating, use elevated temperatures (ranging from 40-47° C) to ablate

diseased tissue, such as cancerous tumors (*6, 7*). Hyperthermia elicits cell death, induces thermotolerance, alters signal transduction pathways and sensitizes the tumor cells to other therapeutics such as radiation and chemotherapy. The thermal effect is more effective in cancers because they have a lower thermotolerance than noncancerous tissue due to their poor blood supply, thus, are more susceptible to heating (*8, 9*). Thermal therapy provides broad heating to the tissue making it difficult to localize for targeting a specific tumor site, resulting in undesired collateral damage.

Recently, photothermal therapy has been explored as an effective method of utilizing heat to treat cancer. Differing from conventional thermal therapy, photothermal therapy provides localized "hot spots" within the tumor at much higher temperatures on the surface of the exogenous agents, which can be targeted specifically to diseased tissue limiting collateral damage. The most common exogenous agent utilized for photothermal therapy is the gold nanoparticle (GNP). Studies have demonstrated that GNPs are extremely effective photothermal agents, converting light radiation into thermal energy at a high efficiency, and a successful cancer therapeutic *in vitro* and *in vivo* due to their passive and active targeting abilities (*10-16*). However, the cell death mechanisms in response to photothermal therapy are not well understood.

1.2 Problem Statement

The goal of this thesis is to obtain a greater understanding of the cellular response to the localized photothermal heating from the irradiated gold nanorods (GNRs). This understanding is necessary for the optimization of photothermal therapy to increase its effectiveness as a cancer treatment. Our objectives include: (1) determining the photothermal therapy dependence on GNR localization and then (2) determining the cell death pathway response to GNR localization and differing photothermal parameters. F,

we determine the photothermal thresholds for (1) initiating the apoptotic cascade and (2) when necrosis becomes the dominant cell death pathway. To better understand this process, we explore the cell death response due to photothermal therapy in monolayer cell cultures and multicellular tumor spheroids (3D cell structures, to mimic *in vivo* tumors). The cell death response to tumor spheroids is compared to the monolayer studies to comprehend the differences and similarities. Overall, we aim to show that through the quantitative analysis of the cellular death pathway response to GNR-mediated photothermal therapy we will be able to optimize and improve cancer therapy.

1.3 PLASMONIC NANOPARTICLES

Nanoparticles have risen to prominence in cancer diagnostic and therapeutic research due to their atomic size, multifunctionality, and adjustable optical properties. They are composed of an assortment of materials fabricated on the nanoscale. In this size range, typical bulk methods to measure the electromagnetic properties do not apply to certain materials, including noble metal particles, known as plasmonic nanoparticles.

Plasmonic nanoparticles have been used extensively for biological imaging and detection. The preferred method of visualizing these plasmonic nanoparticles is through optical microscopy, as a result of their absorption and scattering properties. Scattering-based microscopy techniques, such as differential interference contrast and dark-field microscopy, were found to be more common because of their ease of use and availability. However, two-photon microscopy, a luminescence-based technique, implements thin optical sectioning, which allows for higher resolution three-dimensional images than other optical microscopy techniques. Thus, the ideal choice of microscopy technique for imaging plasmonic nanoparticles depends on the application and obtainable resources, making two-photon microscopy our choice.

Surface plasmon resonance (SPR) is a unique property utilized for the detection and imaging of plasmonic nanoparticles, first realized by Gustav Mie in 1908 (*17*). Plasmonic nanoparticles absorb and scatter light regulated by the SPR characteristic frequency. The incident light electric field induces the collective oscillation of the conduction electrons on the nanoparticle surface. Consequently, the nanoparticle electric field is enhanced and displaced by the collective oscillation of the surface conduction electrons allowing for the nanoparticle absorption during the non-radiative decay (*18-20*). Adversely, nanoparticle Rayleigh scattering corresponds specifically to the electromagnetic energy emanated by the oscillating electric field (*19*).

The SPR characteristic frequency depends strongly on the physical and electromagnetic properties of the plasmonic nanoparticle. Studies have investigated the effect on SPR frequency based on metal type, geometry (*21-23*), inter-nanoparticle coupling (*24-26*), nanoparticle surface functionalization, and the nanoparticle and surrounding medium dielectric properties(*27, 28*). Utilizing these characteristics, the SPR frequency can be tuned from the ultraviolet (UV) to the infrared (IR). Typically, hemoglobin (absorbing in the visible, ~533 nm), melanin (absorbs in the UV) and water (absorbs from the mid-IR to IR) are the most prominent molecular absorbers in the body. Thus, between UV and IR wavelengths, the near infrared wavelength (NIR, 600-1000 nm) range, known as the therapeutic window, is the most desired for biological applications because there is less interference, from scattering and absorption (*29*).

After excitation, the metal nanoparticle electron relaxation is achieved through the non-radiative decay pathway of the plasmon oscillations, leading to two different effects: heat and luminescence. The rapid localized heating uniformly heats the nanoparticle surroundings. It is a photothermal effect that is proportional to the power of the incident light electromagnetic field (*21*). The luminescence, on the other hand, can be utilized as a

contrast mechanism to image plasmonic nanoparticles. The nanoparticle Rayleigh scattering is also effective as a contrast mechanism for imaging and determining the plasmonic nanoparticle structure.

The optical properties and peak SPR frequency can be modeled for gold nanoparticles using solutions to Maxwell's equations. The SPR-dependent values, including nanoparticle geometry and the dielectric properties of the nanoparticle and surrounding media, are necessary to model the nanoparticle effectively. Mie theory is widely used as an exact solution to Maxwell's equations for homogenous concentric spheres (*17*). It has also been expanded to solve for spheres with layered distributions of different materials. According to Mie theory, small spherical nanoparticles exhibit only one peak plasmon resonance frequency, whereas anisotropic particles exhibit two or more peak plasmon bands based on their shape.

Typically, the discrete dipole approximation (DDA), based on the lattice dispersion relation, is used to determine the optical properties and SPR frequency of non-spherical, anisotropic nanoparticles. DDA models the geometry of the nanoparticle as a finite array of polarizable points, which act as dipoles due to the incident electric fields (*30, 31*). Draine and Flatau developed the DDSCAT program to use the DDA to solve for the absorption and scattering of electromagnetic waves by targets of arbitrary geometry (*32*). This approximation has been used to study colloids of both gold and silver (*33*) as well as GNRs (*34-37*).

1.4 GOLD NANOPARTICLES

1.4.1 Optical Properties

GNPs are a class of plasmonic nanoparticles, which exhibit this localized enhanced SPR phenomenon, when fabricated on the nanoscale. As discussed, the incident

electric field induces collective oscillations of surface conduction electrons on the GNP in resonance with the incident electric field (*18-20, 22, 38*). The SPR characteristic frequency depends strongly on the physical properties of the GNP as well as the electromagnetic properties of the GNP and the surrounding medium dielectric properties, which can be modeled using Mie theory and DDA.

The resulting values from both Mie theory and DDA are absorption and scattering efficiencies for each wavelength modeled. The wavelength that corresponds to the maximum absorption efficiency is the peak SPR frequency. When added together for each wavelength, the absorption and scattering efficiencies amount to the extinction efficiency, the total attenuation by the nanoparticle. The ratio of the absorption and scattering efficiency values, respectively, with the total extinction values indicate the percentage of light absorbed or scattered at each wavelength. With the scattering and absorption efficiency values, determining the optical scattering and absorption cross-section is straightforward:

$$\sigma_s = Q_s * \sigma_g$$

$$\sigma_a = Q_a * \sigma_g$$

where the σ_s and σ_g are the optical scattering and absorption cross-sections, Q_s and Q_a are the scattering and absorption efficiencies, and σ_g is the geometric cross-section, which can be measured (*39*). The wavelengths at which nanoparticles strongly scatter or absorb are directly based on these results, as we have modeled in this study, which are exploited for several different imaging techniques.

GNPs have been fabricated in many different shapes and sizes. The most basic form, gold nanospheres, is a solid, spherical colloid, which can range in size anywhere in the nanoscale. Nanospheres tend to absorb light in the visible region of the spectra and their peak SPR frequency is relatively untunable. The peak SPR frequency depends on

the particle radii but large changes in the radii only slightly influence the frequency (*21*). According to Mie theory, gold nanospheres have a higher absorption component than scattering due to their small size, but are still effective in both scattering-based and luminescence-based imaging techniques. As the nanosphere size increases, the scattering component increases and the absorption component decreases. This trend is seen in all geometries of GNPs; therefore, it has been stated that, generally, smaller GNPs (<50 nm) are absorption dominant whereas larger GNPs (>50 nm) are scattering dominant (*19, 22, 23*).

Several groups have fabricated other GNPs with tunable peak SPR frequencies, including gold nanoshells. The pioneering work on gold nanoshells was performed by research groups from Rice University. The nanoshell SPR frequency is tunable because it is composed of a silica core coated with a gold shell (*40-42*). Adjusting the shell thickness to total diameter ratio alters the peak SPR frequency, making it possible to tune the frequency into the NIR. These particles are relatively large, with sizes on the order of 100 nm. Due to their larger size, these nanoparticles have a stronger scattering component than absorbing. Even though the scattering component is dominant, the absorption cross-section of nanoshells is still much larger than typical fluorescent molecules (*22, 40*). As a modification on traditional nanoshells, one group has also fabricated hollow gold nanoshells with a hollow core and a gold shell, which are still tunable, but smaller than typical gold nanoshells, on the order of 40-50 nm (*43, 44*).

GNRs are another frequently used tunable particle, composed of solid gold in a pill-shape, ranging in size characteristically from 20-50 nm. These nanoparticles are smaller than typical nanoshells and, as a result, are absorption dominant, which is essential for luminescence-based imaging techniques (*45*). Even though the scattering is dominated by the absorption, the scattering component is strong enough to be imaged by

many scattering-based techniques. Due to their pill shape, GNRs have a longitudinal (along the length of the GNR) axis and a transverse (along the width of the GNR) axis. Accordingly, each axis has a SPR peak frequency, but because of their relative sizes the longitudinal axis SPR peak is much stronger than the transverse axis SPR peak (*46*). By increasing the aspect ratio (ratio of the length and width dimension) the SPR peak wavelength progresses to longer wavelengths, and can be tuned to the NIR (*22, 47, 48*). At the peak SPR frequency, GNRs have strong absorption and scattering, which has been exploited for imaging and photothermal therapy. In this study, we utilized GNRs, due to their smaller size for targeting purposes, tunable NIR peak SPR frequency, strong contrast in two-photon imaging and high photothermal transduction efficiency (*49*).

1.4.2 Gold Nanoparticle Delivery

Gold is widely used in metal nanoparticle fabrication for biological applications because it is inert and biocompatible. In fact, for many years, gold was ingested as an anti-inflammatory agent and arthritic treatment (*50*). GNPs have been observed to preferentially accumulate within solid tumors due to their design. The enhanced permeability and retention effect (EPR) is a phenomenon found in most solid tumors, which maintains that molecules within a certain size range accumulate in the tumor site at a higher rate than normal tissue (*51-53*). Due to the fast-growing nature, tumors outgrow the original vascular structure and require more nutrients; therefore, tumors enhance proliferation by inducing angiogenesis to increase the flow of nutrients that reach the cancer cells. However, the new tumor blood vessels are crudely formed and tend to contain fenestrations on the order of 0.5-1.5 μm that form between the endothelial cells lining the blood vessel (*52-54*). GNPs, designed with size dimensions smaller than these fenestrations, “leak” through the newly formed tumor blood vessels into the tumor tissue

at a much higher rate than normal tissue (*55*). Furthermore, the lymphatic system surrounding the tumors is insufficient and leads to the inability to remove waste. Therefore, GNPs, typically on the order of tens to hundreds of nanometers, penetrate through the blood vessel enhanced permeability and are retained in the tumor site due to the poor lymphatic system (*51, 55*).

In addition, the gold surface of GNPs allow for facile bioconjugation of antibodies, peptides and polymers through surface modification (*56-58*). Thus, to increase biocompatibility, several different polymers have been conjugated onto the GNP surface, with the most common being polyethylene glycol (PEG). PEG has a neutral surface charge and prevents adsorption of serum proteins, therefore increasing the circulation time in the blood significantly (*59-61*). Several toxicity studies have been performed *in vitro* and *in vivo* showing that most GNPs have negligible toxic effects (*60, 62-66*); and in fact, recent studies have shown that GNPs are non-toxic for up to 400 days (*67*). In addition, numerous groups have exploited this facile surface modification to conjugate cancer biomarkers onto the GNP surface (*68-74*). Several cancer biomarkers, including anti-EGFR and anti-HER2 antibodies, have been used to successfully actively target tumor cells *in vitro* (*70, 75-77*). By conjugating antibodies onto GNPs to target certain cancer cell types, studies have shown that the incident power necessary to induce cell death during photothermal therapy is reduced (*14, 43, 70*).

1.5 PHOTOTHERMAL THERAPY

Thermal therapy has shown potential as a tool for the treatment of solid tumors, due to cancerous cells having a low thermotolerance, compared to non-cancerous tissue, because of their poor blood supply (*8, 9*). Current hyperthermia-based procedures, including microwave and radio frequency (RF) heating, use elevated temperatures

(ranging from 42-47° C) to damage diseased tissue, such as cancerous tumors (*6, 7*). Both techniques provide a broad heating of the tumor; however, the heating is not specific to the tumor, elevating temperatures in surrounding normal tissue. Accordingly, it is desirable to focus the heat to within the tumor periphery. Due to the small GNP size, the emitted heat is confined (on the order of nanometers) to the immediate surroundings of the nanoparticle (*15*).

Recently, photothermal therapy has been explored as an effective method of utilizing heat to treat cancer. Photothermal therapy, a targeted approach of cancer hyperthermia therapy, specifically directs heat into the tumor. In this procedure, an endogenous or exogenous chromophore is excited by laser radiation resulting in the release of thermal energy. Differing from conventional thermal therapy, photothermal therapy provides localized "hot spots" within the tumor at much higher temperatures on the surface of the exogenous agents. If the photothermal agent can convert light into heat efficiently (photothermal transduction efficiency) then light can be delivered using a laser at sub-lethal powers while still inducing heat transfer from the agent to the tumor (*49*). Furthermore, the photothermal agent can be targeted to the tumor site such that the elevated temperature is localized to only the tumor immediate surroundings. As a result, to be an effective photothermal agent, the exogenous particle is required to be inherently inert, can be targeted to a tumor site, can be imaged, and have high photothermal transduction efficiency. Studies have demonstrated that GNPs fulfill those requirements (*10-12, 49, 78, 79*). In fact, GNP-mediated photothermal therapy has been extensively shown to efficiently kill cancer cells *in vitro*, by such processes as protein denaturation and cellular membrane disruption, and reduce tumor size *in vivo* (*15, 72, 76, 80-84*).

1.6 TWO-PHOTON MICROSCOPY

As discussed earlier, GNPs have strong scattering and absorption cross-sections that can be exploited as contrast mechanisms for imaging. Scattering-based microscopy techniques include bright-field, differential interference contrast, dark-field and reflectance confocal microscopy as well as optical coherence tomography. However, by utilizing the absorption properties of GNP, it is also possible to visualize the resulting luminescence emitted from the GNP, such as using two-photon microscopy.

A common disadvantage found in all optical microscopy techniques is diffraction-limited resolution. Diffraction is essentially the bending and spreading of waves, and occurs when an electromagnetic wave, such as light, is incident on a circular lens or mirror. As a result, the light does not focus to a singular point but rather an Airy disk. The Airy disk is observed at the best focused point as a circular spot of light. The diameter of the Airy disk and, consequently, the microscope resolution depends directly on the wavelength of light (λ) used to illuminate the sample:

$$d = \frac{\lambda}{2(n\sin\theta)}$$

where d is the resolution (and Airy disk diameter), n is the refractive index of medium from the objective to the sample, and θ is the angle at which the light is converging. Normally, with visible light the ideal resolution is limited to approximately 0.2 μm (micron to sub-micron range), therefore these optical techniques are known to be microscopic. GNPs are much smaller than this resolution limit; thus, with traditional microscopy, it is difficult to resolve them individually.

Two-photon microscopy (TPM) is a laser scanning fluorescence imaging modality that provides improvements over conventional wide-field and single photon fluorescence microscopy. In TPM, the basic idea is that at sufficiently high photon

densities, two photons with half the energy difference of an electronic transition – exciting fluorescent molecules – can be absorbed simultaneously, in a nonlinear process. Since the probability of the two photons to be absorbed simultaneously is quadratically dependent on the incident intensity, a femtosecond pulsed laser is used such that enough excitation photons are provided to induce two photon absorption. In addition, the two photons need to be tightly focused such that the excitation and resulting fluorescence generation is limited to an extremely small focal volume, usually accomplished using high numerical aperture objectives. This spatial confinement of both two photon absorption and subsequent emission results in the property of three-dimensional resolvability, owing to the reduction in out-of-focus signal generation and increase in the spatial resolution (*85*).

Due to the use of longer wavelength light, typically in the NIR (700-1000 nm), and the absorption volume being spatially confined to the focal region, TPM is well suited for higher depth imaging in optically thick biological samples. TPM generates less out-of-focus signal than either wide-field or confocal fluorescence resulting in improved sectioning for three-dimensional imaging and limited photobleaching. Typically, the resolution spatially and laterally is the same as a perfectly aligned confocal microscope without needing a pinhole, allowing for flexibility in detection geometry (*85, 86*).

GNPs were found to strongly absorb the two photons simultaneously in a non-linear process, due to the coupling of the localized SPRs, exciting the nanoparticle electrons to a higher energy state, thus, GNPs have a strong two-photon absorption cross-section. In the non-radiative relaxation process, these nanoparticles emit an extremely strong photoluminescence effect. One of the first studies utilizing GNPs as a contrast agent for TPM imaged gold nanospheres. The authors imaged different sized nanospheres (2.5, 15, 60 and 125 nm) under TPM and determined that the 60 nm particles exhibited

the strongest emission, whereas the 2.5 nm particles were the weakest by a factor of 3-4. The particles were found to be photostable and devoid of "blinking" effects. To illustrate that aggregation was artificially enhancing the two-photon emission, the authors used DFM to image 15 nm gold nanospheres coated with silica to reduce nanoparticle coupling (*87*).

One group in particular, Wei, Cheng and coworkers, has pioneered the use of GNRs specifically as a contrast agent for TPM. The authors characterized single GNRs with TPM by imaging at different excitation wavelengths. They determined that the GNR two-photon excitation correlated well with the longitudinal SPR band, and the emission was in the 400-650 nm region, nearly 60 times brighter than a fluorescent rhodamine molecule. Since GNR absorption is polarization dependent due to its shape, the authors also established that the GNRs have a cos^4 dependence on the excitation polarization (*88*).

The next studies presented by this group involved the *in vitro* imaging of GNRs using TPM as a method to determine the nanorod localization, similar to studies performed in this thesis. In one of their studies, the authors compared the cellular uptake of nanorods coated with cetyltrimethylammounium bromide (CTAB) – a typical surfactant used in the fabrication of GNRs – and nanorods coated with hydrophilic surfactants such as bis(*p*-sulfonatophenyl) phenylphosphine (BSP) and PEG. TPM was used to visualize the nanorod position and co-localized with phase contrast microscopy to visualize the oral epithelium cancer (KB) cells. Using single nanorod tracking, the CTAB nanorod uptake kinetics were determined and found to cause no adverse effects on the cell within a 5 day period. The CTAB nanorods were internalized at a much higher rate than the BSP and PEG nanorods (*89*). The authors furthered their studies by targeting the GNRs to the KB cells using folate conjugated onto the gold surface. TPM images of the

folate-conjugated nanorods show that their preferential binding to the cell surface of KB cells, which overexpress the folate receptor, compared to the negative control of NIH-3T3 cells, which do not express the folate receptor (*72*).

Intra-vital TPM imaging of surface blood vessels has been accomplished *in vivo*. One study compared the pharmacokinetics of linear PEG and branched PEG functionalized GNRs *in vivo*. Due to the GNR SPR frequency tuned to the NIR, it is possible to image deeper *in vivo* without interference from endogenous sources. In addition, the authors utilized TPM to determine the biodistribution of the nanorods in explanted organs, using autofluorescence to visualize the cells, from mice (*90*).

Several other groups have utilized TPM as a method of visualizing GNPs to determine their distribution and localization *in vitro*. One group imaged hamster ovary (CHO) cells, visualized using two photon autofluorescence, targeted by Concanavalin A conjugated 10 nm gold nanospheres (*91*). Using TPM, another group imaged anti-EGFR antibody conjugated nanorods targeted to unstained A431 cells, which were visualized using autofluorescence. The authors also characterized the difference in power necessary to image at the same signal level: autofluorescence in cells (~9 mW) and the GNRs (140 μW), showing that the GNRs are ~4000 times brighter (*75*).

In our lab, previous studies have used TPM to image the gold nanoshell distribution *ex vivo*, in excised tumors. First, the authors characterized nanoshells (135 nm in diameter) as an effective contrast agent for TPM. In the study, the authors intravenously injected gold nanoshells into the tail veins of tumored mice, with subcutaneous colorectal tumors, and excised the tumors to image the distribution of the gold nanoshells within the tumor. Intratumoral localization was performed by staining the blood vessels (Immunohistochemistry – IHC) and nuclei (YOYO). Three-dimensional

imaging was also performed, exploiting the thin optical sectioning capabilities of TPM, to illustrate that the nanoshells were found surrounding blood vessels in the tumor (*92*).

Our group has also followed up on this study by utilizing TPM to analyze and determine the cellular level biodistribution of gold nanoshell and nanorods (41 nm in length and 10 nm in width) in tumored mice. The authors excised the tumors with either gold nanoshells or nanorods and imaged multiple sections stained with hematoxylin and eosin (H&E – a common histopathological stain), YOYO for nuclei, or IHC for blood vessels. In addition, the authors imaged H&E stained liver and spleen slices with either gold nanoshells or nanorods. Through all of the TPM images, the authors determined that the nanoshells and nanorods had a heterogeneous distribution in the tumor with most accumulation near the tumor edge and unique patterns close to vasculature. The nanorods had a higher accumulation in the tumor core than the nanoshells, possibly due to their smaller size. However, in the liver and spleen, based on TPM images, there was a significant accumulation of both nanoshells and nanorods with no discernible difference between the two particle types (*93*).

1.7 Cell Death Pathways

The two primary pathways of cell death investigated in this study are necrosis and apoptosis (*94, 95*). Necrosis is defined as premature injury-related cell death due to external factors, whereas apoptosis is programmed cell death initiated by naturally causing extrinsic and intrinsic factors. Necrosis typically consists of rounding of the cell due to cytoplasmic swelling, as well as the disruption of organelle membranes. Subsequently, cell functions completely break down and the plasma membrane ruptures resulting in the cytoplasmic contents leaking into the extracellular space, leading to inflammation. During the final steps of necrotic cell death, the cells release pro-

inflammatory factors from the cytoplasm including alarmin molecules, heat-shock proteins, histones, and cytokines (*96, 97*).

Conversely, apoptosis, a type of programmed cell death, involves a complex signaling pathway induced through intracellular signaling, extracellular receptors and the mitochondria (*94, 95*). Apoptosis is a normal part of the cell cycle and is continuously induced in thousands of cells within the human body, although, it is inhibited in some form in cancer cells to allow for the unregulated growth seen in tumors. It can be instigated externally by cytokines through the tumor necrosis factor (TNF) family receptors, toxins, hormones, and growth factors. The intrinsic pathways are initiated by stress from heat, radiation, nutrient deprivation, hypoxia and viral infection (*98*).

The mitochondria are an essential component in the initiation of the apoptotic cascade (*99, 100*). When initiated, the outer mitochondrial membrane permeabilizes and releases SMAC (secondary mitochondria-derived activator of caspases), which impedes inhibitors of apoptotic proteins, and cytochrome c, which combines with APAF-1 (apoptotic protease activating factor) and pro-caspase 9 to form the apoptosome. The apoptosome then activates (by cleavage) caspase 9, which then activates the effector caspases that trigger the apoptotic process by cleaving structural proteins.

Apoptosis is a caspase-dependent form of programmed cell death leading to disassembly of the cell. Caspases are cysteine aspartic proteases involved directly in the apoptotic process. Inactive caspases are synthesized with a pro-domain and cleaving this pro-domain activates the caspase. The cleaving process is regulated by other proteins, death receptors, the apoptosome and other caspases (*101-103*). Caspases are divided into two groups: initiators and effectors (executioners).The initiator caspases, primarily caspase 8 and 9 (2 and 10 are less prominent), are activated early in the apoptotic cascade by death receptors and other indicators of external stress. These caspases are generally

responsible for activating the rest of the apoptotic cascade within the cell including the effector caspases (*104*). The effector caspases, primarily caspase 3 and 7, directly induce apoptosis within the cell by cleaving the cytoskeleton and structural protein substrates involved with DNA repair/fragmentation, signaling, and protein repair/transcription (*105*). The cleaving process leads to cytoplasmic condensation, nuclear shrinkage, DNA cleavage, membrane blebbing and plasma membrane permeabilization (*106*). The conclusion of apoptosis is recognized by cell shrinkage as the cellular contents are packed into membrane-enclosed apoptotic bodies targeted for removal by phagocytosis. Phagocytosis is initiated through externalized signaling molecules, cell death-associated molecules such as phosphatidylserine, which is a phospholipid transferred to the exoplasmic leaflet of the cell membrane by the enzyme scramblase, which recruit phagocytic cells to engulf the apoptotic bodies without inducing an inflammatory or immunogenic response (*107, 108*).

As seen in this study and most other contemporary studies, there is a binary assessment on cell death pathway type, either necrosis, premature inflammatory cell death, and apoptosis, programmed cell death. However, recent studies have found that cell death processes are more complex than previously understood. Two other programmed cell death pathways being explored further currently are pyroptosis and necroptosis (*107, 109-113*). In fact, it has been observed that these cell death processes are inherently inter-related and may not be mutually exclusive, which can cause difficulties in understanding the differences (*109*).

Pyroptosis is caspase 1-dependent programmed cell death, which leads to rapid cell lysis and release of cytosolic contents into the extracellular space resulting in an inflammatory response. Since this cell death pathway involves caspase activity it was not differentiated from apoptosis until recently, when it was determined that pyroptosis was

dependent only on caspase 1, which is not involved in apoptosis. Furthermore, mitochondrial permeabilization, cytochrome c and other caspases are not involved in this cell death process (*110*). Pyroptosis is a host cell death, stimulated by microbial infections and non-infectious molecules, which initiate the process through toll-like receptors, externally, and nod-like receptors, internally. Caspase 1 is activated, which cleaves structural proteins to produce plasma membrane pores, increasing the water influx, leading to cell swelling and osmotic lysis. This lysis allows for the release of inflammatory contents, such as secreted inflammatory cytokines (IL6 and IL8) (*109*).

Necroptosis, alternatively, is a caspase-independent programmed cell death that exhibits the same cell death morphology as necrosis. Necrosis is accidental cell death due to external injury, whereas, necroptosis is programmed and induced through cell death receptors such as CD 95 and tumor necrosis factor receptor 1 (TNFR1), which is the most studied (*107, 111-113*). This process is initiated after ligation of TNFR1 with TNF or other antibodies. At this point, the process may lead to cell repair, apoptosis or necroptosis. After ligation, receptor-mediated conformational changes occur recruiting the complex I, which chooses between cytoprotective and cytotoxic cascades. If continuing along the cytotoxic cascade, ligand-bound TNFR1 is internalized forming the death-inducing signaling complex (DISC) or complex II, which can stimulate either apoptosis or necroptosis. If caspase 8 is deleted, depleted or inhibited, a necroptosis-signaling complex is formed through kinase activity of receptor interacting protein 1 and 3 (RIPK1 and RIPK3) leading to necroptosis. Necroptosis is executed through such mechanisms as the lethal decline of ATP and reactive oxygen species generation (*107*). The cellular disintegration phase is similar to necrosis, except it occurs at a later stage preceding the defined signaling phase, in which oxidative bursting occurs, the mitochondrial membrane hyperpolarizes and the lysosomal and plasma membrane

permeabilizes and ruptures. This leads to spilling of intracellular contents and the inflammatory and immunogenic response (*111*).

Our investigation focuses on understanding the cell death pathways that occur due to GNR-mediated photothermal therapy, therefore we differentiate between inflammatory and non-inflammatory cell death processes. Consequently, in this study the preferred method of cell death is apoptosis, which will limit the extracellular damage due to a lack of inflammatory and immunogenic response. The photothermal parameters necessary to induce apoptotic cell death at significant levels were investigated in this study. For apoptosis and necrosis discrimination, we utilized a fluorescent assay kit composed of propidium iodide (PI) and YO-PRO-1, purchased from Life Technologies. The YO-PRO dye is a carbocyanine nucleic acid stain that can pervade into apoptotic cells due to the slight membrane permeability, whereas the PI is a DNA-binding stain that is excluded from cells with intact or slightly permeable membranes and will only infuse into the necrotic cells (*114*). We utilized a standard technique, flow cytometry, to obtain quantitative values for the fluorescence intensity, for each stain, per cell after photothermal treatment.

1.8 FLOW CYTOMETRY

Flow cytometry is the standard method of quantitatively identifying size, morphology and fluorescent intensity of individual cells (*115*). Fundamentally, the device utilizes microfluidic techniques to line up cells single-file such that we can probe the properties of individual cells. As each cell moves through the device, it is exposed to a laser at a specific wavelength and light is collected at an angle and on the opposite side to obtain side scattered and forward scattered light, respectively. The forward scattered light corresponds to the cell size and the scattered light corresponds to the cell density. These

two values are powerful; researchers have used this data for such things as identifying cell type and viability, based on morphology, as well as differentiating between cells. In addition to the scattering values, there are also PMT optical detectors with bandpass emission filters to detect fluorescent light emitting from the cell after excitation. Therefore, using flow cytometry, we can observe the relative amount of fluorescence intensity within each individual cell. As a result, flow cytometry has been used extensively for quantitatively analyzing cell death pathways in cancerous cells (*114, 116-120*). Furthermore, it has been used specifically for the assessment of drugs as an effective method of inducting apoptosis as a cancer therapeutic (*121-124*). Consequently, using the YO-PRO and PI stains we can quantitatively determine the fluorescence intensity in each cell and the necrotic or apoptotic nature of the cell (*114*). However, it has not been explored with regards to photothermal therapy to quantitatively understand the cell death pathway response to the localized heating, which will be performed in this study.

1.9 MULTICELLULAR TUMOR SPHEROIDS

A major shortcoming of GNP oncological research has been its reliance on two-dimensional monolayer cell culture for experimentation. Because GNRs must penetrate into three-dimensional *in vivo* tumors, the results yielded from monolayer experiments are not entirely applicable to tumor therapy. The solution to this problem exhibited in this experiment is the use of multicellular tumor spheroids (MTSs), matrix-embedded three-dimensional cell cultures used as *in vitro* models of tumors. MTSs offer great resemblance to the micro-regions of solid *in vivo* tumors in terms of structure and growth kinetics and thus serve as a more sensible medium for cancer therapy experimentation. MTSs were originally conceived in the 1940s and 50s, and then Sutherland et al. used

these tumor models to study the effectiveness of chemotherapeutic drugs in 1971 (*125, 126*). They have been overshadowed by easily produced monolayer cell cultures for the past few decades, but have recently undergone a resurgence due to their uniquely accurate modeling of tumor physiology (*127*). New techniques, such as nanotechnology-based drug delivery and imaging with two-photon microscopy, allowing thin optical sectioning and deeper optical imaging instead of having to physically section the MTS, lend themselves well to studies with MTSs. MTSs have also considerably expanded knowledge of tumor extracellular matrices, microenvironments, and tissue dynamics (*127-129*).

MTS retain the functional and morphological features of *in vivo* tumors, follow predictable growth kinetic patterns, and are easily mass-produced for large-scale studies, with MTS having minimal variations in size and shape. The ability of MTS to be produced on a large scale allows them to serve as an economical, cost-effective alternative to inducing cancer and harvesting tumors *in vivo*. Several growth regions characterize tumor structure and closely resemble analogous regions in tumors: a capillary zone of nutrient and oxygen transfer at the MTS surface, a zone of differentiation and cell growth directly below the surface of the MTS, a quiescent zone of cells in a state of quiescence and a central zone of necrotic cells (*125*).

MTS, like *in vivo* tumors experience an inward proliferation of cells during growth; exhibits clearly defined glucose, oxygen and nutrient gradients and accumulate metabolites and catabolites when healthy. Furthermore, MTS can become hypoxic in their most nutrient-deficient regions, and as a result of these substantial gradients, have been shown to be resistant to anti-cancer therapeutics at similar levels as *in vivo* tumors (*130, 131*). Analysis of cancer cells within MTSs has shown a higher degree of morphological and functional differentiation than cells grown in monolayer culture.

Another distinct advantage of MTS is the fact that they more accurately display the cell-cell and cell-matrix interactions seen in *in vivo* tumors. These cell-cell and cell-matrix interactions play a large role in tumor responses to drugs including enhancing the cellular repair, and monolayer cultures do not effectively take these external factors into account, making MTSs a much stronger model of cancerous tumors (*125*). The extracellular matrix (ECM) formation creates a barrier to drug and nanoparticle delivery. These MTS, like their counterparts in *in vivo* tumors, also displayed growth kinetics, distributions of biological response modifiers and survival signals, metabolic rates, and resistance to radiation therapy and chemotherapy. Furthermore, their response to treatment may be affected by potential penetration barriers (ECM), altered expression profiles or signaling pathways of particular targets, such as the variation of DNA damage and repair mechanisms. By varying the size of MTS for treatment, the MTS experiments can be focused on 3D cellular interactions and structure only or in combination with authentic pathophysiological milieu conditions (*127*). Consequently, MTS have been studied extensively as an effective *in vitro* model for economical, high throughput testing of drugs and cancer therapeutics (*132-135*). Primarily, these studies observe the overall drug distribution and examine the therapeutic effects, which are frequently affected by the ability of the therapeutic to distribute uniformly throughout the MTS (*136*). As a result, many studies explore methods of enhancing the penetration and uptake and inspect the therapeutic improvement (*137-140*). In this study, we will examine two different delivery techniques to understand the differences in cell death pathway responses to photothermal therapy with disparate GNR distributions.

Chapter 2: Nanoparticle-mediated Photothermal Therapy: Determining Photothermal Efficiency and Cell Death Dependence on Nanoparticle Localization

2.1 INTRODUCTION

In this chapter, we aim to compare the capability of nanoshells and nanorods to generate heat based on their number density, mass gold and optical density for photothermal therapy. We simulated the optical properties of multiple sizes of nanorod and nanoshell, including our sized GNPs, using the discrete dipole approximation (DDA) and Mie theory. The heating profiles were measured of GNPs suspended in tissue simulating phantoms during a photothermal heating cycle and compared to determine the heat generation when nanoshells and nanorods were at equivalent number densities. We determined that nanoshells generated more heat than nanorods at equivalent number densities and that it was necessary to have ~36 times the number of nanorods as nanoshells to generate the same amount of heat. However, at equivalent optical densities we determined that nanorods generate ~2 times as much heat as nanoshells and calculated that the nanorods have twice the photothermal transduction efficiency as nanoshells. We believe that these results can be a comprehensive aid in determining the optimal GNP geometry for photothermal therapy.

Our subsequent objective was to show that there is a dependence on GNR localization on the efficacy of nanoparticle-mediated photothermal therapy, by measuring the power and temperature thresholds for inducing damage. Photothermal therapy can induce cell damage, through either a necrotic or apoptotic pathway, at differing laser powers depending on the localization of GNRs. The apoptotic pathway seems ideal, because it should require less heating to induce and will cause intracellular damage, which means the damage can be localized without causing injury to the surrounding

tissue. Therefore, determining the nanoparticle localization that corresponds to specific cell damage pathways and lower laser power thresholds can increase the efficiency of photothermal therapy. We demonstrated this by measuring the laser fluence rate (W/cm^2), power density over a certain area, threshold difference between GNRs localized to the cell surface and GNRs internalized within the cell, affecting specific cell death pathways for photothermal destruction.

We utilized GNRs targeted to two different cancer cell components, extracellularly bound to the cell membrane and the internalized in the cell, which were localized to the perinuclear space. We confirmed localization of the GNRs using TPM and performed photothermal therapy by irradiating the cell samples containing GNRs with an NIR laser. The fluence rate and temperature thresholds for each GNR localization was determined to be significantly less in each case for the internalized GNRs. Through these experiments, we have determined that GNR-mediated photothermal therapy of cancer cells appears to depend on the localization of the GNR, which indicates that different cell death pathways and mechanisms are possibly being induced by the different GNR localizations. To further this study, we can determine whether the actual cell death pathway response is also dependent on GNR localization during photothermal therapy. Utilizing this knowledge, we can optimize GNR-mediated photothermal therapy by determining the ideal GNR location to induce cell death.

2.2 RELEVANT WORK

NIR absorbing plasmonic nanoparticles enhance photothermal therapy of tumors. In this procedure, systemically delivered gold nanoparticles preferentially accumulate at the tumor site and when irradiated using laser light, produce localized heat sufficient to damage tumor cells. Gold nanoshells and nanorods have been widely studied for this

purpose, and while both exhibit strong NIR absorption, their overall absorption and scattering properties differ widely due to their geometry.

Comparisons between nanoshells and nanorods have been studied previously (*10, 141-143*). Studies have determined that nanorods have a higher temperature increase per mass gold (*141*) and that the absorption cross-section of nanorods is two times higher than nanoshells (*142*). Furthermore, several studies have been published regarding the photothermal efficiency of GNPs (*10-12, 143, 144*). Both Cole et al. and Cheng et al. have compared gold nanoshells with nanorods but come to differing results. The Cheng study has a different formulation for determining the photothermal efficiency than we utilize in the current study, which is based on number density of the GNPs (as opposed to optical density) and finds that nanoshells are more efficient (*143*). Whereas, the Cole study follows a similar efficiency definition as we discuss in the current study, utilizing an energy balance equation to derive the efficiency based on previous work, to find that nanorods were more efficient than nanoshells (*10, 12, 144*). However, all of these studies disregard the multiple methods of comparison used to evaluate nanoparticles, as well as the size factor that greatly influences the GNP optical properties and the photothermal properties; as a result, we will explore those problems in greater detail within this study.

One group has studied the targeting abilities of folate-conjugated gold nanorods to KB (oral epithelium carcinoma) cells that overexpress the folate receptor (*72*). Using TPM the authors confirmed that the conjugated nanorods bound to the membrane of KB cells and were internalized with nuclear localization occurring after 6 hours incubation with the KB cells. The authors performed photothermal therapy on the samples with membrane bound gold nanorods and internalized nanorods, speculating that cell death is caused by membrane blebbing. It was determined that incident continuous wave (CW)

laser treatment for photothermal therapy with membrane bound nanorods required less power to induce cell damage than the internalized nanorods for irradiation types.

Recently another group measured the difference in cell damage pathways and photothermal therapy between gold nanospheres localized to the cytoplasm and targeted to the nuclei (*73*). In this study, the authors found that irradiated with a CW laser the nanospheres localized in the cytoplasm induced cell damage at energies of 108-114 J, whereas at 210 J the nanospheres targeted to the nuclei did not induce any cell damage. For the pulsed laser, the energy necessary to induce cell death in cytoplasm localized nanospheres was 0.8-1.0 mJ and 0.3-0.45 mJ for nuclear targeted nanospheres. Thus, we see that the nuclear targeted nanospheres are more effective in inducing cell damage when irradiated with a pulsed laser but less effective with a CW laser, and the energy necessary to cause damage is much less with a pulsed laser than a CW laser.

2.3 Experimental Methods

2.3.1 Nanoparticle Fabrication

Nanospectra Biosciences, Inc. (Houston, TX) provided concentrated nanoshell and nanorod solutions. The fabrication process for both GNPs has been discussed in detail previously (*145, 146*). To determine the GNP size, we imaged (Figure 1) dilute solutions using transmission electron microscopy (TEM). The dimensions were averaged over 300 individual particles, for both GNPs, measured in the TEM image using ImageJ (NIH Bethesda, MD). The nanoshells were found to have a total outer diameter of 145 nm ± 11.7 nm, with a silica core diameter of 120 nm (Figure 1). The nanorod dimensions were measured to be 25.8 nm ± 3.8 nm by 7.4 nm ± 0.9 nm, with an aspect ratio of 3.5 and an effective radius of 6.18 nm (Figure 1). The effective radius, r_{eff}, is defined as the radius of a sphere with an equivalent volume (V) as the nanorod:

$$r_{eff} = \left(\frac{3V}{4\pi}\right)^{\frac{1}{3}} \quad (2)$$

During the fabrication process, Nanospectra Biosciences modified the GNP surface with polyethylene glycol (PEG) to mimic the GNPs that are used *in vitro* and *in vivo*. To measure the extinction spectra and optical density for the nanoparticle solutions, we used a UV-Vis Spectrophotometer (Beckman Coulter DU720, Brea, CA).

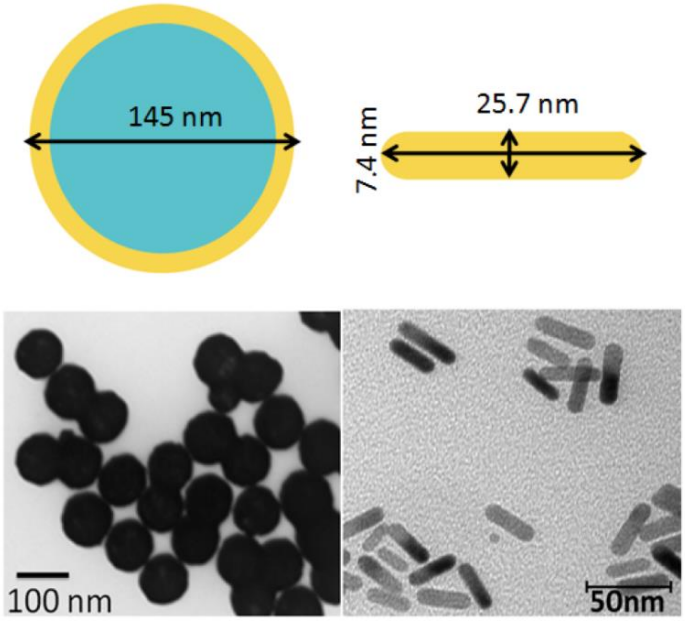

Figure 1: Gold Nanoparticles. Gold nanoshells were fabricated with a silica core and gold shell and using TEM imaging were measured to 145 nm in diameter. Gold nanorods were fabricated as a cylinder with hemispherical caps and measured using TEM a size of 25.7 nm by 7.4 nm.

2.3.2 Nanoparticle Optical Simulations

Using Mie theory and the discrete dipole approximation (DDA), we simulated nanoshell and nanorod optical properties, respectively. The dielectric function for bulk gold, determined by Johnson and Christy (J&C), was used for the nanoshell and nanorod

simulations (*147*). The dielectric function for bulk gold was corrected based on the small size of both the nanoshells and nanorods (*33*). The size correction includes an additional damping term in the dielectric function due to collisions of conduction electrons to the GNP surface (*33, 37*).

We used a DDA program, DDSCAT 7.0, to model nanorod optical properties using the lattice dispersion relation (*31*). The DDA program approximates the scattering and absorption of any arbitrary geometry by modeling the target as a series of polarizable points. The nanorod geometry was modeled as a cylinder surrounded by water (*34, 47*). The DDSCAT program divides the particle into I_d polarizable points (dipoles), which are on a lattice described by an interdipole distance d, based on the particle volume, V:

$$V = I_d d^3 \tag{3}$$

The number of dipoles is chosen by the following accuracy criterion:

$$|m|kd < 0.5 \tag{4}$$

where m is the particle's complex refractive index and k is the angular wave number ($k = \frac{2\pi}{\lambda}$), which all simulations performed in the DDSCAT software satisfy.

For the nanoshell optical properties, we utilized the Mie solution, because it is an exact solution to Maxwell's equations for concentric spheres. The nanoshells were modeled as an individual, gold-coated silica particle surrounded by water. To perform the calculations we used Maetzler's MATLAB Mie Theory code for coated spheres (*148*). The nanoshell dielectric function was divided in two parts: (1) the inner core of silica was derived by Malitson and (2) the same size-corrected dielectric function for the gold shell as derived by J&C (*147, 149*).

With the nanorod and nanoshell absorption and scattering efficiency from DDA and Mie Theory we were able to determine the expected absorption and scattering coefficient (μ_a and μ_s):

$$\mu_a = \sigma_a N = \sigma_g Q_a N \quad (5)$$

$$\mu_s = \sigma_s N = \sigma_g Q_s N \quad (6)$$

where σ_a and σ_s are the absorption and scattering cross-sections (cm^2) and N is the GNP number density (#/mL). The concentration of GNPs is known; thus, only the absorption cross-section needs to be determined, which is equivalent to the multiplication of σ_g, the geometric cross-section (cm^2), and Q_a, the absorption efficiency (Eq. 1). The absorption efficiency represents the ratio of the absorption and geometric cross-sections.

2.3.3 Experimental Procedures

We performed two sets of experiments to determine the concentration equivalency factor (ξ) in tissue phantoms and the photothermal transduction efficiency, respectively (defined later in this study). To simulate the environment within tissue, the GNPs in the experiments for the concentration equivalency factor were suspended in tissue phantoms at multiple concentrations. To calculate the photothermal transduction efficiency, it was necessary to have the sample of GNPs suspended in a non-absorbing and non-scattering media to simplify the solution for the photothermal transduction efficiency. As shown in Equation 8, the *OD* was included to correspond to the extinction of specifically the GNPs and not the sample as a whole. Additionally, scattering processes would increase the fluence at the solution surface, but also would attenuate the fluence deeper in the solution, which could cause artificial increases or decreases in photothermal efficiency. As a result, we conducted the experiments on GNPs in a 10%

trehalose solution, which has the same optical characteristics as water in the wavelength range of interest.

2.3.4 Concentration Equivalency Factor Experimentation

The concentration equivalency factor defines the relationship between the concentrations of nanorods and nanoshells when heat generated from both solutions are equivalent. To determine this value we have to find the amount of heat generated from nanorods and nanoshells at multiple concentrations, to find the concentration of nanoshells and nanorods at which the generated heat is equivalent. The temperature change at the end of the heating cycle for the nanoshells, dT_{NS}, and nanorods, dT_{NR}, indicate the heat generated by each particle type during the procedures. The ratio of the temperature change at a fixed concentration of nanoshells, dT_{NS}, (1x or 2x) to the temperature change of varying concentrations of nanorods, dT_{NR}, (5x – 80x). Thus, the concentration equivalency factor ($\xi = dT_{NS}/dT_{NR}$) is the ratio of the determined concentrations, respectively.

For this experiment, we prepared tissue phantom solutions composed of diluted 10% intravenous fat emulsion (Liposyn II 10%, *Abbott Laboratories*, North Chicago, IL) and 90% dH_2O, which mimicked the scattering properties of tissue. This dilution resulted in a solution with similar scattering values to normal human epithelial tissue, $\mu_s' = 1\ mm^{-1}$, at the irradiation wavelength (*150*). The experimental control was a sample with the intravenous fat emulsion dilution without GNPs. The GNPs were suspended in the tissue phantom solution at multiple concentrations including: 1x, 2x, 5x, 10x for the nanoshells and 5x, 10x, 20x, 40x, and 80x for the nanorods, where x is the nominal physiological concentration. The physiological value, $x = 1.14 \times 10^9$ GNPs/mL, is based on previous biodistribution studies of nanoshells in tumors in mice after intravenous

injection (*151, 152*). The corresponding concentration for nanorods is unknown; hence, in this study we determined the concentration of nanorods at which the same amount of heat is generated as nanoshells at the physiological concentration.

2.3.5 Photothermal Transduction Efficiency Experimentation

The photothermal transduction efficiency denotes a value for the efficacy of gold nanoparticles converting absorbed light radiation into thermal energy. For determining the photothermal transduction efficiency, we prepared a set of different samples. In this study, the GNPs solutions were suspended in 10% trehalose at a set optical density of 0.25 at the irradiation wavelength (808 nm). The control for this experiment was a solution of 10% trehalose. All GNP samples were pippetted into a 96-well plate (BD Falcon, Franklin Lakes, NJ).

The calculation of the photothermal transduction efficiency for both nanoshells and nanorods was conducted in a similar method to Roper and coworkers (*12*). Using an energy balance for our experimental system, we determined the photothermal transduction efficiency. The total energy balance is:

$$mC_p \frac{dT}{dt} = E_{in,np} + E_{in,sample} - E_{ext} \quad (7)$$

where m and C_p are the solvent (10% trehalose) mass and heat capacity and T is the sample temperature. $E_{in,np}$ is the energy input based on the heat dissipated by the nanoparticles in the solution:

$$E_{in,np} = I(1 - 10^{-OD})\eta \quad (8)$$

where I is the laser power, OD is the sample optical density at the excitation wavelength of 808 nm, and η is the photothermal transduction efficiency, fraction of absorbed light converted into heat. $E_{in,sample}$ is the energy input based on the heat generated by the solvent and sample well, which was measured independently following the same method

of solving for E_{ext} with the experimental control of trehalose solution. E_{ext} is the energy output based on the external heat flux between the sample and the surroundings:

$$E_{ext} = hA(T_{sample} - T_{amb}) \tag{9}$$

where h is the heat transfer coefficient, A is the sample well surface area, T_{sample} is the temperature of the sample, which in our case is the steady state maximum temperature, and T_{amb} is the ambient room temperature.

We determined the quantity, hA, by measuring the sample cooling after the laser was turned off. When the laser is turned off Equation 7 becomes:

$$mC_p \frac{dT}{dt} = -E_{ext} = -hA(T_{sample} - T_{amb}) \tag{10}$$

Rearranging Equation 10:

$$dt = -\frac{mC_p}{hA} \frac{dT}{(T_{max} - T_{amb})} \tag{11}$$

After integrating Equation 11:

$$t = -\left(\frac{mC_p}{hA}\right) \ln(T_{max} - T_{amb}) \tag{12}$$

From this equation, we can determine the characteristic rate constant:

$$\tau_{out} = \frac{mC_p}{hA} \tag{13}$$

such that:

$$T_{max} - T_{amb} = \exp\left(-\frac{t}{\tau_{out}}\right) \tag{14}$$

Thus, from the cooling data, we can determine the characteristic rate constant and solve for the heat transfer coefficient. At the steady state temperature, the rate of heating is equal to the rate of heat transfer out of the system:

$$E_{in,np} + E_{in,sample} = I(1 - 10^{-OD})\eta + E_{in,sample} = E_{ext}$$
$$= hA(T_{max} - T_{amb}) \tag{15}$$

As a result, the photothermal transduction efficiency can be solved for directly from the steady-state temperature experiments:

$$\eta = \frac{hA(T_{max} - T_{amb}) - E_{in,sample}}{I(1 - 10^{-OD})} \quad (16)$$

2.3.6 Instrumentation

We used an InSb infrared (IR) camera (FLIR Systems SC4000, Boston, MA) with a spectral range of 3-5 μm, to measure the heating characteristics of the sample. The IR camera was placed directly above the 96-well plate and a laser was mounted at an angle of approximately 30° such that the sample was irradiated completely while not interfering with the imaging (Figure 2). We used a fiber-coupled NIR (λ = 808 nm) diode-laser (ThorLabs L808P1WJ, Newton, NJ) rated for up to 1 W of power. Using a biconvex lens (Newport Corp., Irvine, CA) the laser spot was focused to 6 mm in diameter, approximately the same diameter as the well.

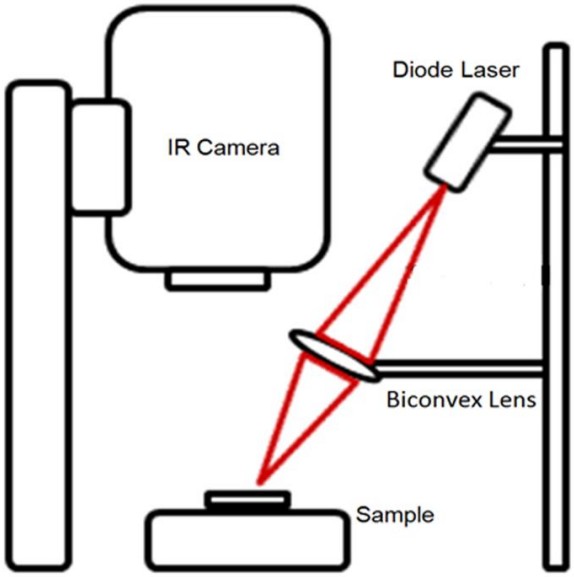

Figure 2: Instrumentation. Gold nanoparticle solutions were prepared in 96 well plates and illuminated at a slight angle by a diode laser (808 nm) focused onto the sample by a biconvex lens. An infrared (IR) camera was placed above the sample to measure the increase in temperature of the solution with respect to time.

2.3.7 Photothermal Experiments

Each sample was illuminated at a constant fluence rate of 2 W/cm^2. Prior to each experiment: we sonicated and mixed the sample thoroughly to create a uniform distribution of GNPs, and confirmed the laser power using a standard power meter (Newport Corp., Irvine, CA). We selected a region of interest at the laser spot center and solution to measure the sample heating and the cooling after the laser was turned off, using the ThermoVision software (FLIR Sys., Boston, MA). For the tissue phantom experiment, we heated all samples for 5 minutes, to mimic current *in vitro* and *in vivo* photothermal studies, and let the sample cool to room temperature for 10 minutes after the laser was turned off. For the photothermal transduction efficiency experiment, we heated the samples to steady state, which occurred after approximately 25 minutes of irradiations and let the samples cool to room temperature for around 20 minutes. All comparisons and analyses were performed in MATLAB (The Mathworks Inc., Natick, MA).

2.3.8 Cell Culture

In the second part of this study, we wanted to determine whether the PEG and CTAB GNRs were targeted to two separate localizations on and within human colorectal carcinoma cells. Human colorectal tumor cells (HCT-116, ATCC, Manassas, VA) were seeded in T25 flasks with cell culture media composed of McCoy's Modified Medium (Corning CellGro, Corning, NY) supplemented with 10% fetal bovine serum (FBS) and 1% penicillin-streptomycin-amphotericin B (Lonza, Basel, Switzerland) at 37°C with 5% CO_2. After the cells reached confluence, we detached the cells with 0.5% trypsin solution (Thermo Scientific HyClone, Waltham, MA) and centrifuged at 600 RPM for 5 minutes. The cells were seeded into 6-well plates containing a coverslip in each well. After the cells reached confluence on the slides, we removed the old media incubated them with

the respective GNRs (PEG and CTAB) immersed in McCoy's Media at a 0.25 optical density (OD) ranging from 6-24 hours. Then we removed the GNR-media solution and washed the cells with phosphate buffered saline (PBS) three times to ensure that all free GNRs were removed.

2.3.9 Two-Photon Imaging

The cellular nuclei were then stained with CellMask plasma membrane stain (Life Technologies, Carlsbad, CA) as a reference to demonstrate GNR location and the cells were fixed with a 4% paraformaldehyde solution. The coverslips were then placed on a glass slide with mounting media (Vectashield, Vector Laboratories, Burlingame, CA), sealed using nail polish, and imaged using TPM (Prairie Technologies, Middleton, WI). Imaging was done with an ultrafast pulsed femtosecond tunable Ti:Sapphire laser (Spectra Physics Mai-Tai, Irvine, CA). The laser was tuned to 800 nm to image the gold nanorods and 750 nm to image the plasma membrane stain. To image the emitted light, we used photomultiplier tubes (PMTs) with a 660 nm +/- 20 nm bandpass filter for the gold nanorods (Channel 1) and 595 nm +/- 50 nm bandpass filter for the plasma membrane stain (Channel 2). The cells were imaged with a water-immersion 60x objective (Olympus) with a 1.0 NA allowing for a high resolution and high magnification. All images were taken with the proprietary software (PrairieView) and analyzed with ImageJ.

2.3.10 Photothermal Therapy

After determining the GNR localization, we performed photothermal therapy on the HCT-116 cells with the respective GNRs. Here, cells were seeded from T-75 flasks as above, but into 12-well plates. Again, we let the cells grow to confluence before incubating the respective GNRs suspended in McCoy's media with the cells for 24 hours.

After removing the GNRs, we washed 3 times with PBS. We then irradiated each sample, while the overall temperature was maintained at 37° C on a hot plate, with a diode laser (λ = 808 nm) (ThorLabs, Newton, NJ) for 5 minutes while measuring the temperature of the laser spot size (0.2 mm) using an InSb infrared camera (FLIR Systems SC4000, Boston, MA) with a wavelength detection range of 3-5 μm. We increased the laser fluence rate from 5-40 W/cm^2 to determine the lowest fluence rate, or threshold, to induce cell death for the respective GNRs. The sample temperature increase measured at the fluence rate threshold for each respective GNR was determined as the temperature threshold. To allow for cell death pathways to transpire, we waited 24 hours after irradiation to stain for cell death and imaged thereafter using a bright-field microscope. To demonstrate cell death, we stained the cells with Trypan blue (Thermo Fisher Scientific, Waltham, MA), which stains nonviable cells with compromised membrane integrity and imaged under a bright-field microscope.

2.4 RESULTS

2.4.1 Gold Nanoparticle Optical Properties

The GNP optical properties were determined using simulations with the measured size parameters as input. The plots in Figure 3 illustrate the simulated optical efficiency spectra and measured extinction spectrum for GNS. The resonance peak wavelength was found to be the same for both the simulated and measured extinction spectra (780 nm) indicating the validity of the Mie theory simulation. The simulation (Figure 3a) shows the nanoshells are highly scattering (~75% of the extinction efficiency), and they have an absorption efficiency of 1.9 at the laser wavelength of 808 nm. Given the absorption efficiency, the calculation for the absorption cross-section follows from Equation 1, with a value of 3.1 x 10^{-10} cm^2.

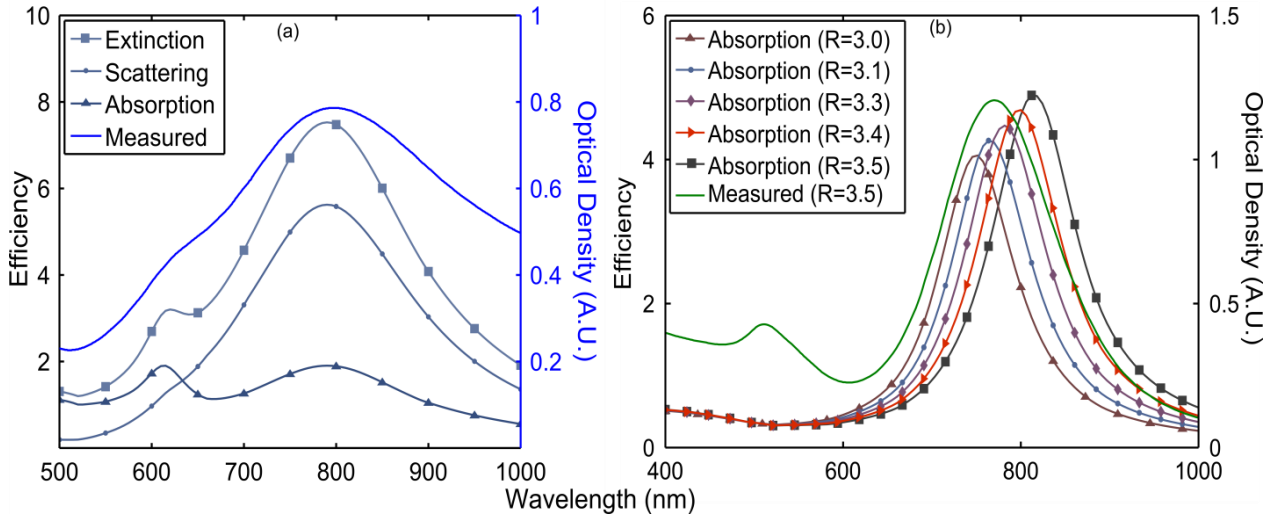

Figure 3: Gold nanoparticle optical properties. The extinction, absorption, and scattering efficiencies of gold nanoshells (a) and gold nanorods (b) were simulated using Mie theory and DDA, respectively. The gold nanoshell measured extinction spectra (a) peak matches with the peak of the efficiencies; additionally, gold nanoshells were found to be high scattering. Gold nanorods (b) were found to have virtually no scattering component (0.2% of extinction) for multiple aspect ratios (3.0–3.5), therefore, only shown is the absorption efficiency of the different aspect ratios in comparison to the measured optical density of our gold nanorods with an aspect ratio of 3.5.

Figure 3b illustrates the simulated absorption efficiency spectra as compared to the measured gold nanorod extinction spectrum. The simulated absorption efficiency shows a resonance peak wavelength that is red-shifted (812 nm) in comparison to that wavelength from the measured extinction spectrum (770 nm). We varied the nanorod length to change the aspect ratio from 3.5 to 3.0, resulting in a peak resonance blue shift. The aspect ratio that best matches the measured value was approximately 3.3. In all cases, the absorption efficiency accounted for approximately 99.8% of the extinction efficiency. These results suggest that nanorods in this size range are completely absorption dominated, and after simulating multiple aspect ratios we have found an

absorption efficiency that is a good indicator of the individual nanorods used in this study. We found the absorption efficiency value to be 4.9 for the nanorods, and utilizing Equation 1 the absorption cross-section was calculated as 8.7×10^{-12} cm^2.

2.4.2 Photothermal Heating

We measured the heating response of both gold nanoshells and nanorods in tissue simulating phantoms to determine the ξ factor. Figure 4 shows the temperature profiles for the nanoshells and nanorods for 5 minutes of heating and the subsequent cooling cycle. Both GNP types exhibit a significant temperature rise in comparison to the experimental control (0x) when illuminated by NIR light. The temperature change (after 5 minutes of heating) ranged from approximately 12°C to 42°C for concentrations of 1*x* to 10*x* of gold nanoshells. However, for the gold nanorods, the temperature change (after 5 minutes heating) ranged from approximately 3° C to 17°C for concentrations of 5*x* to 40*x*. The temperature change increased as the concentration increased.

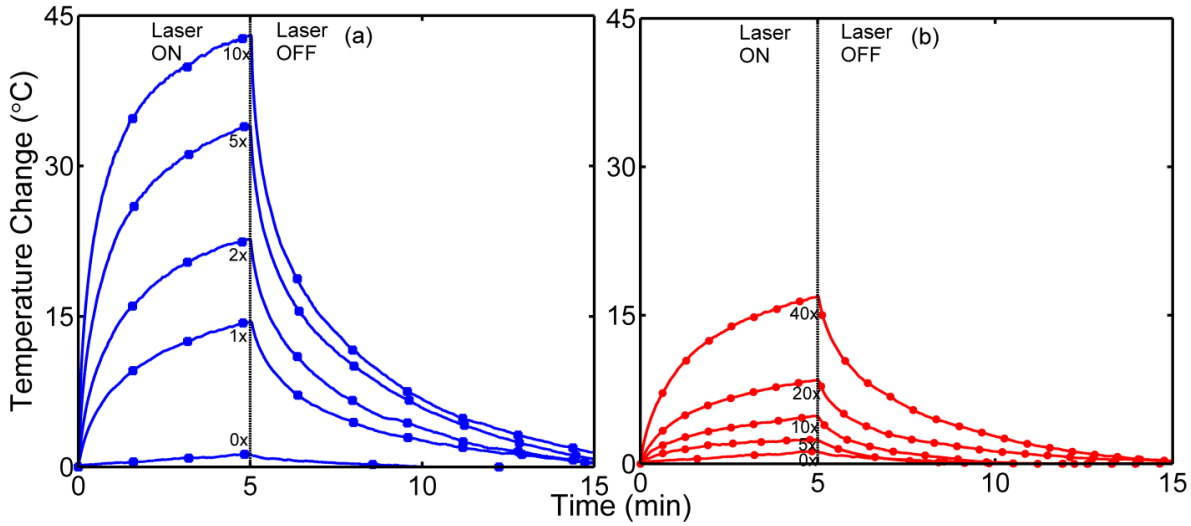

Figure 4: Gold Nanoparticle Temperature Change. (a) Measured temperature change of increasing concentrations (0x, 1x, 2x, 5x, and 10x) of gold nanoshells in tissue phantoms. (b) Measured temperature change of increasing concentrations (0x, 5x, 10x, 20x, 40x) of gold nanorods in tissue phantoms. All temperatures were measured during 5 minutes of illumination with a diode laser (λ = 808nm) at a fluence rate of 2 W/cm^2 and 10 minutes of cooling after the laser was turned off.

To determine the ξ factor, interpolation was performed for all nanorod concentrations between 5*x* and 80*x* using the power law (Figure 5). For the 1*x* nanoshell concentration, it is shown that the nanorod concentration when the ratio is equal to one is approximately 36. For the 2*x* nanoshell concentration, the nanorod concentration for heat generation equivalence is shown to be approximately 72. Therefore, we can conclude for these sized GNPs, to generate the equivalent heat, it is necessary to have a nanorod concentration 36 times the concentration of nanoshells. As with the per GNP heating abilities, the ξ factor is as a result of the larger nanoshell absorption cross-section (3.1 x 10^{-10} cm^2). In fact, when compared to the nanorod absorption cross-section, the nanoshell

absorption cross-section is approximately 35 times larger (3.1 x 10^{-10} cm^2/8.7 x 10^{-12} cm^2).

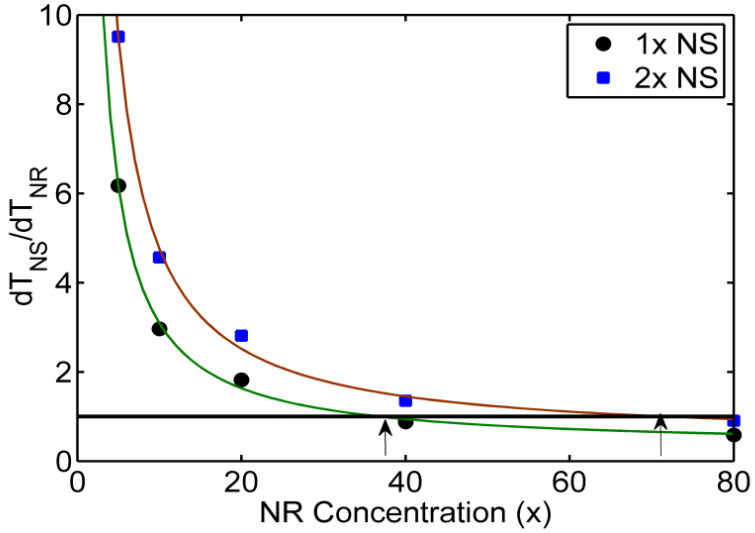

Figure 5: Concentration Equivalency Factor ξ. Plot shows the ratio of the temperature change of a single concentration of nanoshells (dT_{NS}) and the temperature change at multiple concentrations of gold nanorods (dT_{NR}). The green and red lines are power law interpolations of the different nanoshell concentrations (1x and 2x). The black line denotes when the ratio equals one. The intersection of the black line with the red and green lines (as demonstrated by the arrows), indicates the concentration equivalency factor.

2.4.3 Photothermal Transduction Efficiency

To determine the photothermal transduction efficiency we fit equation 14 to the cooling data to determine the characteristic rate constant and the heat transfer coefficient (Figure 6) based on Equation 13. Both samples of GNPs were diluted to an optical density of 0.25 (inset of Figure 7) at 808 nm in a 10% trehalose solution. Using Equation 16, the photothermal transduction efficiency for nanoshells and nanorods was determined to be ~25% and ~50%, respectively (Figure 7). Thus, nanorods are shown to be twice as efficient as nanoshells at converting the light radiation into thermal energy.

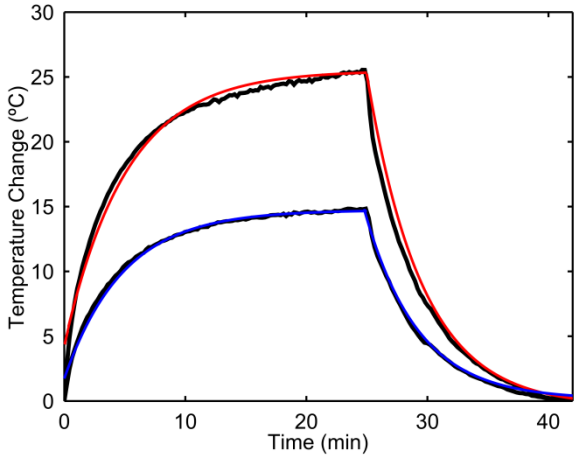

Figure 6: Steady-state Heating of Gold Nanoparticles. Gold nanoshell (lower temperature) and gold nanorods (higher temperature) were heated to steady-state using fluence of 2 W/cm^2 then let to cool down to room temperature. The heating and cooling temperature change were fit with exponentials to determine the heat transfer coefficient for solving the photothermal transduction efficiency.

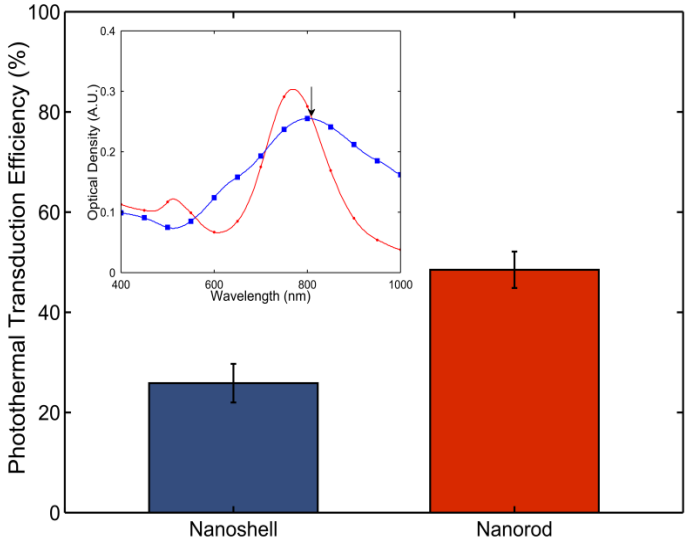

Figure 7: Photothermal Transduction Efficiency. Inset is of nanoshell (blue with squares) and nanorod (red with circles) extinction spectra diluted such that at 808 nm the optical density was the same (0.25) as denoted by the arrow. Bar plot of photothermal transduction efficiency shows gold nanorods (red, 50%) are twice as efficient at converting light into heat as gold nanoshells (blue, 25%). Error bars are standard deviation over multiple trials (n =3).

2.4.4 Gold Nanorod Absorbance

The first step for our *in vitro* photothermal therapy experimentation was choosing GNRs for studying as it is more efficient photothermally than gold nanoshells (Figure 7). As a result, we characterized two types of GNRs, the (1) PEG and (2) CTAB GNRs, and determining their location with respect to the cell. Using UV-Vis, we determined the respective GNR optical densities and found that the CTAB GNRs had a slightly red-shifted SPR peak in comparison to the PEG GNRs (Figure 8). This could be due to slight GNR aggregation in the sample measured. However, the shape of the curve with respect to wavelength was similar.

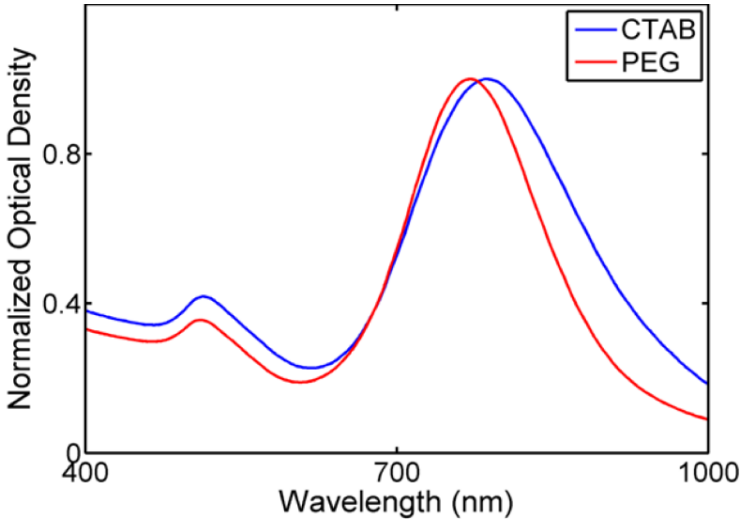

Figure 8: Absorbance spectra of CTAB and PEG GNRs. CTAB GNR peak SPR frequency is slightly red-shifted than the PEG GNRs.

2.4.5 Gold Nanorod Localization

To validate our hypothesis that CTAB GNRs would be more attracted to the cells than PEG GNRs due to their surface charge, we imaged human colorectal cancer cells that had been incubated with both GNRs, respectively, for 24 hours to determine GNR

location. Through experimentation, we determined that 24 hours was a desired incubation time, because it allowed for a high concentration of GNRs to interact with the cell without inducing cytotoxicity. TPM allows for three-dimensional imaging due to its thin optical sectioning as discussed previously. We imaged the samples at several depths from which we could determine if the GNRs were located on or within the plasma membrane in all three dimensions (Figure 9).

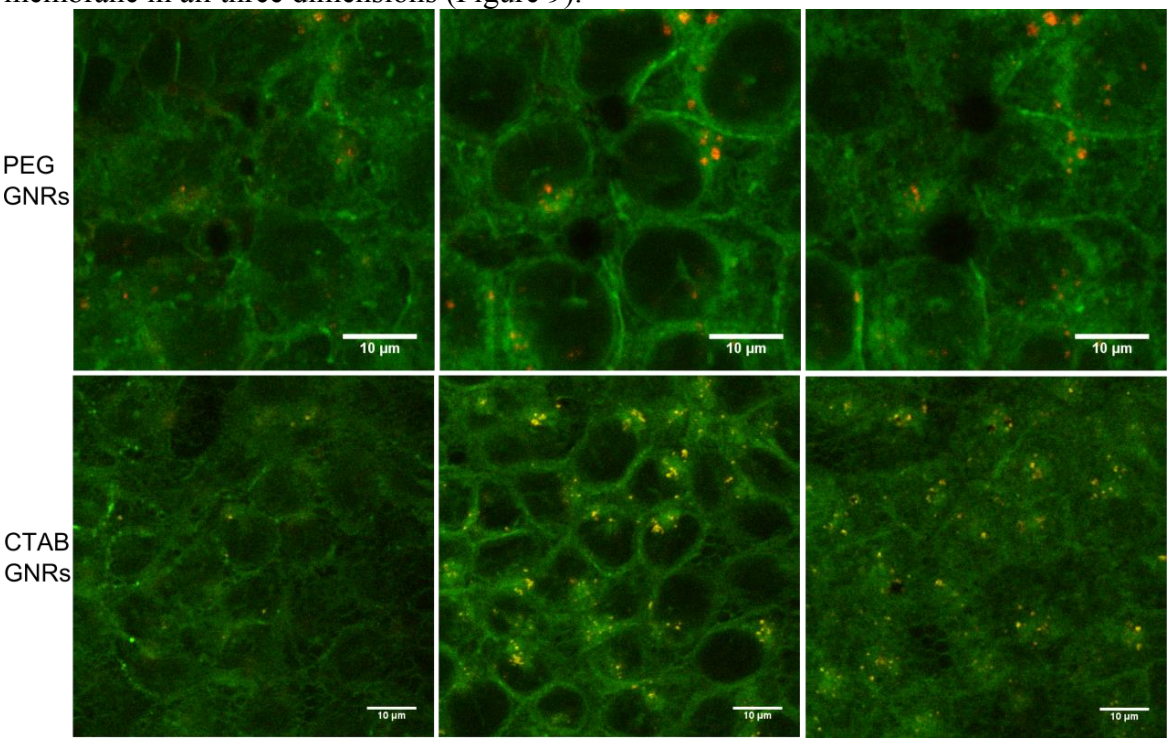

Figure 9: GNR Cellular Localization. Included in each set of 3 images is: (1) imaged above the cell, (2) in focus with the cell membrane (green), (3) image below the cell. The PEG GNRs (red) are shown to be in the extracellular space, most likely non-specifically bound to the cell. The CTAB GNRs (yellow) are shown to be internalized and within the cytoplasm and perinuclear region.

From the TPM images, it is clearly shown that the CTAB GNRs were within the cell membrane stain in the same imaging plane as the cells (Figure 9). Furthermore, the

CTAB GNRs were not in focus when imaged above and below in the Z-direction, therefore suggesting that the GNRs are not bound to the cell membrane. We observed that the GNRs seem to be aggregated, possibly localized to organelles within the perinuclear region (Figure 9). On the other hand, we detected that the PEG GNRs had limited internalization and seem to bind to the cell membrane at the 24 hour incubation time period. The PEG GNRs do not appear be within the cell membrane stain, but instead are limited to the extracellular space and are in focus when imaging below in the Z-direction, therefore suggesting that the PEG GNRs are bound to the cell membrane surface (Figure 9).

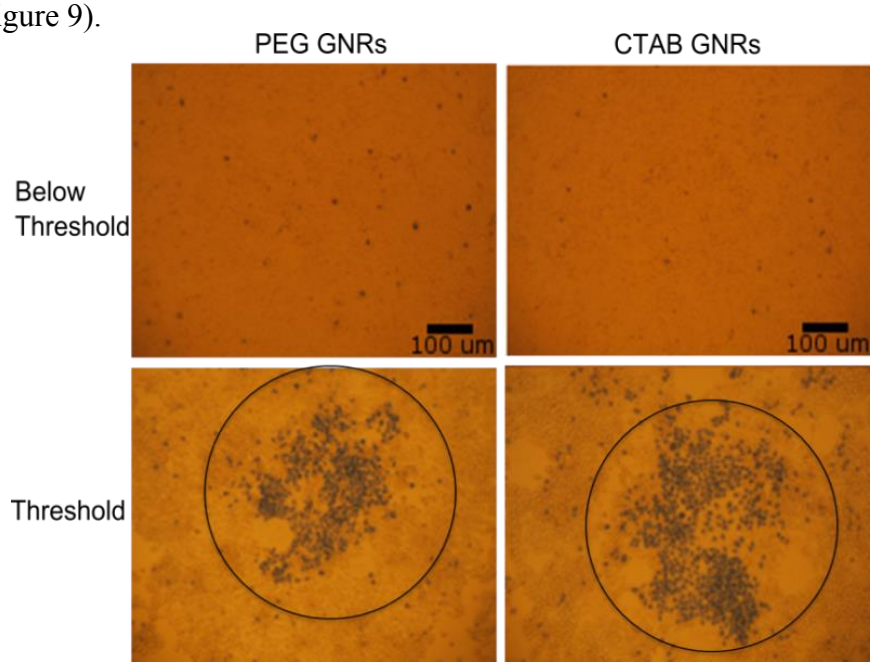

Figure 10: Fluence Rate Threshold Determination. For both the PEG and CTAB GNRs the photothermal therapy does not induce cell death (Trypan blue) until fluence rate threshold, 30 W/cm2 and 19 W/cm2, respectively.

2.4.6 *In Vitro* Photothermal Therapy

After determining that the CTAB and PEG GNR cellular localizations were significantly different, we performed photothermal therapy on the samples, to determine

if there was a dependence on localization. To determine the fluence rate threshold, we conducted several rounds of experimentation, increasing the fluence rate until we measured signs of cell death using the Trypan blue (Figure 10). We found the lowest fluence rate to induce cell damage for photothermal therapy of CTAB (internalized) GNRs was approximately 19 W/cm^2 with a temperature difference of 6.6°C ± 0.1°C (Figure 11). In addition, we determined that the fluence rate threshold to induce cell damage for photothermal therapy with PEG (membrane-bound) GNRs was approximately 30 W/cm^2, which corresponded to a temperature difference of 8.3°C ± 0.2°C (Figure 11). The difference in fluence rate and temperature thresholds indicates that there is a dependence on the GNR localization in initiating cellular death pathways during photothermal therapy.

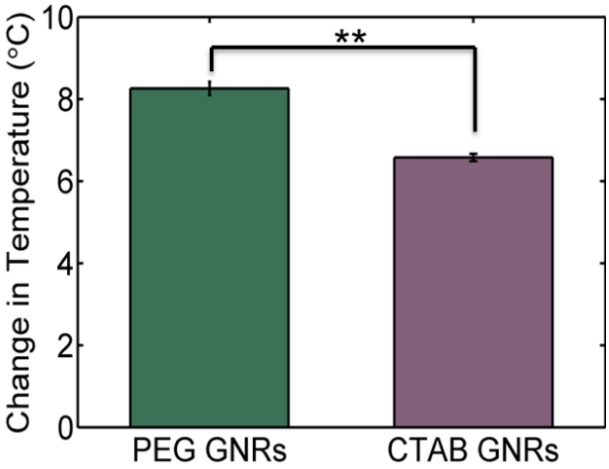

Figure 11: GNR heating during photothermal therapy. Showing there is a significant difference in the change in temperature for PEG and CTAB GNRs ($p < 0.001$)

2.5 DISCUSSION

2.5.1 Nanoparticle Optical Properties

In this study, we simulated the optical properties of our sized nanoshells with Mie theory and determined an approximation of our sized nanorod optical properties with DDA (Figure 3). The nanoshells are scattering dominated and have a much lower absorption component than nanorods, whereas the nanorods were completely absorption dominated. However, to accurately compare the absorption properties of both GNPs, the overall geometric cross-section needs to be incorporated to determine the absorption cross-section. We found the nanoshell absorption cross-section to be approximately 35 times larger than the nanorod absorption cross-section. Thus, we would expect the nanoshells to generate more heat than nanorods per particle when illuminated with NIR light, despite their lower absorption efficiency.

Based on this study and the study performed by Ungureanu and coworkers, it is apparent that DDA does not provide an accurate approximation to the optical properties of nanorods (*37*). In their study, they compared the simulated results with the measured extinction spectra of four different sized nanorods. The authors used four different shapes (cylindrical, hemispherically-capped cylinder, ellipsoid, and rectangular) and three different size-corrected dielectric functions for gold (J&C, Palik and Weaver) to model the gold nanorods (*147, 153, 154*). Based on their results, the authors found that the size-corrected J&C and cylindrical shape gave the best results, but, it still was not completely accurate. However, we still performed the DDA in this study with the size-corrected J&C dielectric and modeling the nanorod as a cylinder as shown in Figure 3b to show that the nanorod optical properties are absorption dominated.

There are a few areas of loss that are not accounted for in our model and experiment. Possible losses of heat generation include the metal distribution around the

GNP surface. When heated, the particle may elongate or compress, modifying the GNP geometry, which in turn may alter the optical properties and heating characteristics slightly. Additionally, since the temperature at the GNP surface cannot be determined, it is possible that there are heating effects in the direct surroundings of the GNPs. Even though the steady-state temperature is lower than boiling point due to losses to convection between the solution and air, the GNP surface temperatures can possibly reach boiling point. Consequently, phenomena such as localized evaporation could take place, which can cause cavitation bubbles. These steam pockets and cavitation bubbles may affect the GNP surroundings optically and physically, which is not taken into account in the experiment.

2.5.2 Photothermal Heating

In our photothermal tissue phantom experiments, the heat generated by different concentrations of both nanoparticle types was recorded. From these results, it was determined that the temperature increase was substantial and, most likely, would cause damage to cells as in all previous photothermal studies. Additionally, we observed that per individual GNP, the nanoshells, indeed, had the larger temperature change.

However, if we compare the GNP heating based on their respective mass of gold, we observe a different result. The mass per GNP of nanoshell is 1.34×10^{-8} μg and for nanorod is 1.91×10^{-11} μg. At the 80*x* concentration of nanorods there is 0.58 μg gold in solution, corresponding to a ~25°C temperature change. We also compared this data with the 1*x* concentration of nanoshells, which corresponds to a mass of 5.03 μg gold in solution, accounting for only the shell, and a temperature change of ~14.8°C. Even at approximately 10 times smaller than the sample with the lowest mass gold of nanoshells used in this study, the sample with the highest mass gold of nanorods has a significantly

greater increase in temperature. Therefore, the nanorods can generate more heat per μg gold in comparison to nanoshells.

This study was based on the known physiological dose of nanoshells that reach the tumor site *in vivo*. The heat generated by this concentration of nanoshells has been shown to be enough to cause cell death and a significant reduction in tumor size. In current literature, the same value is unknown for nanorods. As a result, the heat generation based on the physiologic dose of nanoshells was chosen as the low end threshold for determining the equivalent concentration of nanorods necessary to cause tumor ablation. According to the observed, to generate the equivalent amount of heat it is necessary to have 36 times the concentration of nanorods as the concentration of nanoshells, for these specific sizes of nanoshells and nanorods. When compared to the ratio of the simulated absorption cross-sections, it is remarkably similar.

Our obtained data suggests that to achieve the same heating, a substantially larger number of nanorods would need to be present at the tumor site. Since the two GNPs have different sizes and shapes, likely there will be differences in the number of GNPs that reach the tumor sites. The comparative targeting efficiency of nanoshells and nanorods is unknown; therefore, it is possible that at similar doses to nanoshells, more particles can reach the tumor site. Effectively, if nanorods can reach the tumor site at a rate of 36 times more than nanoshells, then this would negate the lower heat generation, and it would be more efficient in converting the available laser power into heat. The choice of GNP may be an application dependent process. For example, it may be desired to have smaller GNPs, for more effective targeting or larger GNPs, for more heating with fewer particles. Further studies need to be performed to determine the targeting efficiency of both GNP types.

2.5.3 Photothermal Transduction Efficiency

Another important finding in this study was the photothermal transduction efficiency. For this experiment, we heated both GNPs at the same optical density (at the illumination wavelength) to steady state and let cool to room temperature. The nanorods had a much larger temperature increase than nanoshells in this experiment as predicted by the simulations. The cooling data was modeled with a single exponential fit to determine the sample characteristic rate constant. Using this value, we determined the heat transfer coefficient, which in this model considers energy losses to the surroundings. Furthermore, we also modeled the control sample cooling data, which was heated to steady state, to determine the energy dissipated by the sample well. For our sized GNPs, it is important to note that these nanorods were found to be twice as efficient at transducing light radiation into thermal energy as nanoshells.

2.5.4 Gold Nanorod Absorbance

The GNRs used for the *in vitro* photothermal therapy experiment were fabricated with PEG and CTAB on the gold surface. During characterization, the optical density of both GNRs was measured and we determined that the profile was the same but the peak SPR frequency was shifted to a longer wavelength for the CTAB GNR (Figure 8). It is possible, that this is due to the CTAB GNRs being slightly less stable when removed from a solution with free CTAB as was performed to lessen the cytotoxicity. Therefore, there may be slight aggregation, which can lead to red-shifting of the optical density. However, to account for these differences, the GNR solutions were mixed to 0.25 OD at 808 nm to correspond with the laser wavelength for photothermal therapy, for all experiments.

2.5.5 Gold Nanorod Localization

In addition, since CTAB GNRs are cationic and the PEG GNRs are neutral, we hypothesized that the CTAB GNRs would be highly attracted to the cell due to the negative charge of the cellular membrane, whereas the PEG GNRs would only be non-specifically bound to the cell. Furthermore, CTAB is a surfactant and lipophilic, which allows it to pass through the lipophilic plasma membrane into the cell. The CTAB GNRs were found to be internalized, using TPM, assembled in the perinuclear region, possibly near the mitochondria or nuclei. We believe that the initial attraction of the CTAB GNRs to the cell is due to the ionic differences in charge as discussed above (*155*). TPM images show that PEG GNRs were found at a lesser strength than the CTAB GNRs and primarily bound to the surface of the cell (Figure 9). PEG induces a neutral GNR surface charge such that the GNR can freely move about *in vivo* without being recognized as foreign object. However, this also indicates that the PEG GNRs will only non-specifically bind the cell surface and at a lesser extent than the CTAB GNRs.

2.5.6 *In Vitro* Photothermal Therapy

In our subsequent photothermal studies, we show that internalized GNRs, 19 W/cm^2, required significantly less laser power to induce cell death than the membrane-bound GNRs, 30 W/cm^2 (Figure 11). We believe that this disparity is due to the different GNR localizations inducing different cell death pathways during photothermal therapy. Other groups have shown similar results that location plays a role in the power necessary to cause cell death (*72, 73*). Huang et al. compared gold nanospheres targeted to the cytoplasm and nuclei and found that it depended on the laser delivery method, either using a pulsed or a CW laser. However, in the Tong et al. study the authors suggest that membrane-bound GNRs result in cell death at a lower power than internalized GNRs, which is contrary from what we found. The authors make some assumptions in their

study, such as using a pulsed laser in CW mode is only an approximation to actual CW laser. Therefore there are still pulses, albeit on the millisecond level, which could still induce photodestructive effects, such as bubble formation. Additionally, the final concentration of the internalized and membrane-bound GNRs is unknown; therefore it is possible that the final GNR concentrations skewed the results. We believe that internalized GNRs should induce cell death with a lower temperature difference and power, because the GNRs would utilize the highly localized heating within the cell in close proximity to the most susceptible cellular components that induce apoptosis, the mitochondria and nuclei.

Therefore, in this study, we sought to determine whether final concentration skewed our results. As a result, we measured the temperature change to show that the temperatures required to induce cell death was statistically different for both the internalized (6.6°C) and membrane-bound (8.3°C) GNRs ($p<0.001$, Figure 11). Since the temperatures reach steady-state, we can assume the sample is undergoing an adiabatic reaction, therefore:

$$Q_{in} = \mu_a * \Psi = Q_{out} = \Delta T \rho C_p$$

where Q is thermal energy, μ_a is the absorption coefficient, Ψ is the fluence rate, ΔT is the change in temperature, ρ is the density of the solution (essentially water), and C_p is the heat capacity of the solution. The density and heat capacity of the membrane-bound and internalized samples are identical, and the absorption coefficient is directly proportional to the concentration. Therefore, we solve for the effective concentration:

$$\mu_a \propto C_{eff} \propto \frac{\Delta T}{\Psi}$$

If we compare the ratio of the C_{eff} for both the membrane-bound (0.3) and internalized (0.34) GNRs, we get a 12% difference in concentration. However, if we look at the ratio

of the fluence rate thresholds for both GNRs we demonstrate a 37% difference. Therefore, we believe that the concentration is not the primary source of the difference in the fluence rate threshold. As a result, this indicates that the difference is because GNR-mediated photothermal therapy is dependent on GNR localization.

2.6 CONCLUSION

Nanoparticle heating dynamics depend on a combination of factors that include their overall geometry and optical absorption efficiency. Ultimately, the appropriate choice of nanoparticle will depend on the application and the particle's targeting kinetics. In this study, we determined the optical absorption efficiency for nanorods and the adjusted optical absorption efficiency for nanoshells per particle. Yet, due to the larger size of nanoshells, their absorption cross-section is much larger than nanorods. As a result, the nanoshells have a much larger increase in temperature than the nanorods on a per particle basis. Additionally, a higher nanorod concentration is required for equivalent heating of nanoshells, for the GNP sizes tested. However, in comparing the effectiveness of converting light radiation into thermal energy, the nanorods are twice as efficient. Both GNPs have utility in photothermal therapy depending on each particle's ability to reach the tumor site. Therefore, with the information from this study, an educated choice can be determined on which GNP to use for photothermal therapy *in vivo* based on the respective GNP targeting efficiency.

In addition, we determined that PEG GNRs were found to non-specifically bind to cell surface and CTAB GNRs were found to be internalized. The internalized GNRs had a lower fluence rate and thermal threshold for cell death during photothermal therapy than surface bound GNRs. To prove that the final concentration was not the primary factor in the fluence rate threshold difference we determined the thermal threshold

difference. In conclusion, we have shown that localization of the GNR may be a factor in inducing different mechanisms or pathways of cell death during photothermal therapy. As a result, we have continued our studies in determining the effect of photothermal therapy and GNR localization on the cell death pathway response.

Chapter 3: Cell Death Pathway Dependence on Nanoparticle Localization during Photothermal Therapy

3.1 Introduction:

In this portion of the study, we aim to show that not only is the power necessary to induce damage for GNR-mediated photothermal therapy dependent on GNR localization, as shown in Chapter 2, but also that the cell death pathways are dependent. GNRs have been shown to induce localized heating to only the immediate surroundings; therefore, we believe the location should significantly affect the power necessary to induce damage and cell death pathways. Since the heat will be localized to certain organelles, essential to cell death processes, different cell death pathways could be induced. To perform this study, we targeted GNRs to different cellular localizations by varying the GNR incubation time with the cells. We confirmed GNR localization with TPM and performed photothermal therapy with a NIR diode laser. After irradiation, our final step involved quantitatively analyzing the cell damage threshold to determine the percentage of apoptotic and necrotic cells using flow cytometry. Utilizing this knowledge, we can better optimize GNR-mediated photothermal therapy by developing a better understanding of cell death pathway response to GNR localization.

3.2 Relevant Work

Previous studies have indicated that GNP-mediated photothermal therapy is dependent on the localization of GNPs and investigated the effect on cell death pathways (*72, 73, 156*). Using folate-conjugated GNPs, one group showed that membrane-bound GNPs required a lower energy threshold necessary to induce damage during photothermal therapy than internalized GNPs (*72*). In another study, GNPs in the cytoplasm were shown to more effective at inducing cell death than GNPs in the nuclei with CW laser irradiation, but the opposite effect was observed for pulsed laser

irradiation (*73*). The authors demonstrated that the induction of apoptosis and necrosis is dependent on the localization of GNPs and the laser delivery method using qualitative assessments by imaging stained cells, with only necrosis being observed with the pulsed laser irradiation for both localizations. However, in a different study, the authors observed that apoptosis could actually be induced with pulsed laser irradiation and that necrosis had a higher energy threshold to induce damage than the apoptotic threshold (*156*). Due to the lack of quantitative analytical studies executed regarding the subject of cell death response to photothermal therapy, we believe that it is necessary to for a comprehensive study performing quantitative cell death pathway measurements on the effect of photothermal therapy.

3.3 Materials and Methods

3.3.1 Gold Nanorod Synthesis

We followed the same gold nanorod synthesis as previously done by Nikoobakht et al and Jana et al in a Ag(I) –assisted growth method (*145, 157*). Briefly, we made an aqueous gold seed particle solution is prepared by adding 250 μL of 0.01 M $HAuCl_4$ (Sigma Aldrich, St. Louis, MO) to 9.75 mL of aqueous 0.1 M cetyl trimethylammonium bromide (CTAB, Sigma Aldrich, St. Louis, MO) solution in a vial, while stirring. Then we made a 0.01 M $NaBH_4$ (CTAB, Sigma Aldrich, St. Louis, MO) solution by placing DI water in a vial, equilibrating it in an ice bath, adding the $NaBH_4$, and mixing it rapidly. 600 μL of the aqueous 0.01 M $NaBH_4$ is added to the gold seed particle solution and stirred for 2 min. Next, an aqueous growth solution is prepared by combining 9.5 mL of 0.1 M CTAB, 75 μL of 0.01 M $AgNO_3$ (Sigma Aldrich, St. Louis, MO), 500 μL of 0.01 M $HAuCl_4$, and 55 μL of 0.1 M ascorbic acid (Sigma Aldrich, St. Louis, MO) in a 15 mL centrifuge tube. Upon adding ascorbic acid, we inverted the tube two times to mix,

creating a colorless solution due to partial reduction of the gold salts. 12 μL of the gold seed solution was then added to this growth solution followed by slowly inverting it two times to mix, which was incubated at 27 °C overnight without stirring. The resulting GNR solution was centrifuged three times at 8000 RPM for 20 minutes to remove excess CTAB, to reduce the chance of cytotoxicity, and concentrated the solution in 15 mL of DI H_2O. We measured the dimensions by averaging over 300 individual particles analyzed in ImageJ (NIH Bethesda, MD) using transmission electron microscopy (TEM, FEI Tecnai, Hillsboro, OR) images. We measured the optical density (OD) or absorbance of the solution using a UV-Vis Spectrophotometer (Beckman Coulter DU720, Brea, CA)

3.3.2 Cell Culture

Human colorectal tumor cells (HCT-116, ATCC, Manassas, VA) were seeded in T25 flasks with cell culture media composed of McCoy's Modified Medium (Corning CellGro, Corning, NY) supplemented with 10% fetal bovine serum (FBS) and 1% penicillin-streptomycin-amphotericin B (Lonza, Basel, Switzerland) at 37°C with 5% CO_2. After the cells reached confluence, we detached the cells with 0.5% trypsin solution (Thermo Scientific HyClone, Waltham, MA) and centrifuged at 600 RPM for 5 minutes. For TPM imaging, seeded into 12 well plates with coverslips placed in each well and for photothermal therapy, cells were seeded into 96 well plates. After reaching ~90% percent confluence, we incubated GNRs in fresh culture medium at 0.5 optical density (OD) with the cells.

3.3.3 Two-Photon Imaging

For TPM imaging, depending on exposure time, we removed the GNR media after 1.5 hours and let the cells incubate further in fresh media for varied exposure times to allow for the cellular internalization processes to occur. We allowed the cells incubate

further for 0, 1.5, 4.5, 10.5 and 22.5 hours for a total of 1.5, 3, 6, 12 and 24 hours post-GNR exposure. After GNR incubation, we removed the media and washed three times with PBS and fixed the cells in 4% paraformaldehyde (PFA, Fisher Scientific, Waltham, MA) for 10 minutes. After fixation, we washed with PBS three times and stained the cells with a plasma membrane stain (CellMask, Life Technologies, Carlsbad, CA) for 20 minutes and washed again with PBS three times. Then we removed the coverslip from the bottom of the well and mounted it on a glass slide with Vectashield mounting medium (Vector Laboratories, Burlingame, CA) and sealed it with nail polish. Imaging was performed under a TPM (Prairie Technologies, Middleton, WI) with an ultrafast pulsed femtosecond tunable Ti:Sapphire laser (Spectra Physics Mai-Tai, Irvine, CA). The laser was tuned to 800 nm to image the gold nanorods and 750 nm to image the plasma membrane stain. To image the emitted light, we used photomultiplier tubes (PMTs) with a 660 nm +/- 20 nm bandpass filter for the gold nanorods (Channel 1) and 595 nm +/- 50 nm bandpass filter for the plasma membrane stain (Channel 2). The cells were imaged with a water-immersion 60x objective (Olympus) with a 1.0 NA allowing for a high resolution and high magnification. All images were taken with the proprietary software (PrairieView) and analyzed with ImageJ (NIH, Bethesda, MD).

3.3.4 Photothermal Therapy

For photothermal therapy fluence rate threshold experiments we incubated the GNR with cell culture medium for the full 1.5, 3, 6, 12, and 24 hours before performing the experiments. Then, we irradiated the cells with an 808 nm CW diode laser, focused to a spot size of 0.16 μm diameter, for five minutes at different fluence rates, ranging from 20-50 W/cm^2. During irradiation, we placed the 96 well plates on a heated plate to keep the cells at 37°C. As a control, we also irradiated cells without GNRs at 50 W/cm^2. To

assess damage, we used Trypan Blue which is a visible light stain that is excluded from live, viable cells and allowed into cells with membrane damage, which indicates necrotic cell death. To allow for all death processes to occur, we waited 24 hours after laser irradiation and stained the cells with Trypan Blue for 5 minutes and washed with PBS 3 times. Then we imaged the cells under a bright-field microscope to evaluate the damage.

3.3.5 Flow Cytometry

To probe cell death pathway initiation after photothermal therapy we incubated the GNRs in a similar method as for TPM imaging, removing the GNR media after 1.5 hours and let the cells incubate further in fresh media for varied exposure times (namely 0, 4.5 and 22.5 hours post-GNR incubation) to allow for the cellular internalization processes to occur. To analyze the cell death pathways, we stained for apoptosis and necrosis using the Vybrant Apoptosis Assay Kit #4 (Life Technologies) including YO-PRO-1 (YP, 491/509 nm) and Propidium Iodide (PI, 535/617 nm). YP is able to pass through the slightly permeable membrane in apoptotic cells and emits a moderate fluorescence whereas PI can only stain cells with compromised membrane integrity indicating necrosis. One hour after photothermal therapy, we washed, trypsinized, centrifuged the cells in microcentrifuge tubes, and then stained the cells with a solution containing YP and PI for 30 minutes on ice. We chose one hour after photothermal treatment because of a study showing that apoptosis and necrosis measurements depend on time after cell injury, in which the authors found that the apoptotic maximum was approximately one hour after treatment (*158*). As a control, we stained cells with no external effects (negative control), cells exposed to 1 hour of UV radiation (apoptotic positive control) and cells exposed to 30 minutes of lysis buffer (Promega, Madison, WI). To quantitatively measure the YP and PI fluorescence we used a flow cytometer (BD

Accuri C6, Franklin Lakes, NJ) with PMTs and bandpass filters at 530 nm +/- 15 nm (FL1) for YP and >670 nm (FL3) for PI. Cells that are alive have low amounts of YP or PI fluorescence. Apoptotic cells have only moderate YP fluorescence and necrotic cells have high YP and PI fluorescence.

3.4 RESULTS

3.4.1 Gold Nanorod Characterization

We first characterized the GNRs using TEM to determine the size and UV-Vis to measure the spectra to confirm that these GNRs were optimal for cellular delivery, imaging, and photothermal therapy. Analyzing TEM images (inset of Figure 12) with ImageJ, we measured the size of the GNRs to be approximately 47 nm in length and 15 nm in width. As shown in the absorbance plot (Figure 12) the transverse SPR frequency stayed constant around 530 nm and we tuned the longitudinal peak SPR frequency to a sharp peak located around 780 nm, by modifying the aspect ratio to approximately 3.

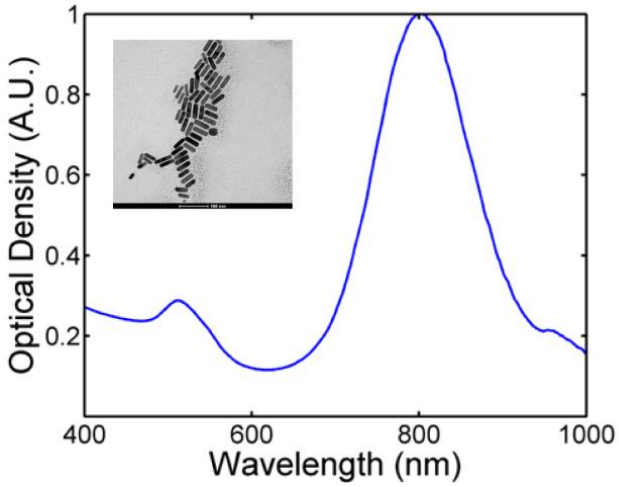

Figure 12: Absorption spectra for fabricated gold nanorods. Inset: TEM image of fabricated gold nanorods

3.4.2 Gold Nanorod Localization

Next, we determined the localization of the GNRs in cancerous cells after different durations. To do this, we imaged the cells using TPM after incubation with 0.5 OD GNRs for a range of times: 1.5, 3, 6, 12, and 24 hours. We found that the concentration correlated to 0.5 OD was ideal because there was no apparent cytotoxicity within 96 hours of incubation yet it was sufficient to induce photothermal damage. TPM is optimal because of its thin optical sectioning, which allows us to image above the cell, within the cell and below the cell to accurately define the GNR location. We found that the GNRs were found in different cellular regions at the different time points as the cellular internalization process advanced.

In Figure 13, we show three slices for each significant time point from a TPM Z-stack going through the cells. The Z-stack consists of a slice at the top (1) of the cell, within (2) the cell and at the bottom (3) of the cell. The Channel 1 PMT, colored as red, detected the GNRs primarily, and the Channel 2 PMT, colored as green, detected the cell membrane stain. At the 1.5 hour time point, the GNRs were observed to start to bind and accumulate on the cell membrane (Figure 13). After 3 hours of GNR incubation, we found the GNRs to be mainly accumulated on cell membrane similar to the 1.5 hour time point, but at a higher GNR volume. Internalization was more prominent after 6 hours (Figure 13) of GNR incubation with GNRs starting to aggregate inside the cell close to the cell membrane, most likely in lysosomes. At 12 hours (Figure 13) after incubation, the GNRs were fully internalized in cells and appeared to be not as aggregated, spread throughout the cell, possibly escaping from lysosomes. Finally, at the 24 hour time point (Figure 13), the GNRs seem to be accumulating near organelles within the cellular perinuclear region, possibly nuclei or mitochondria.

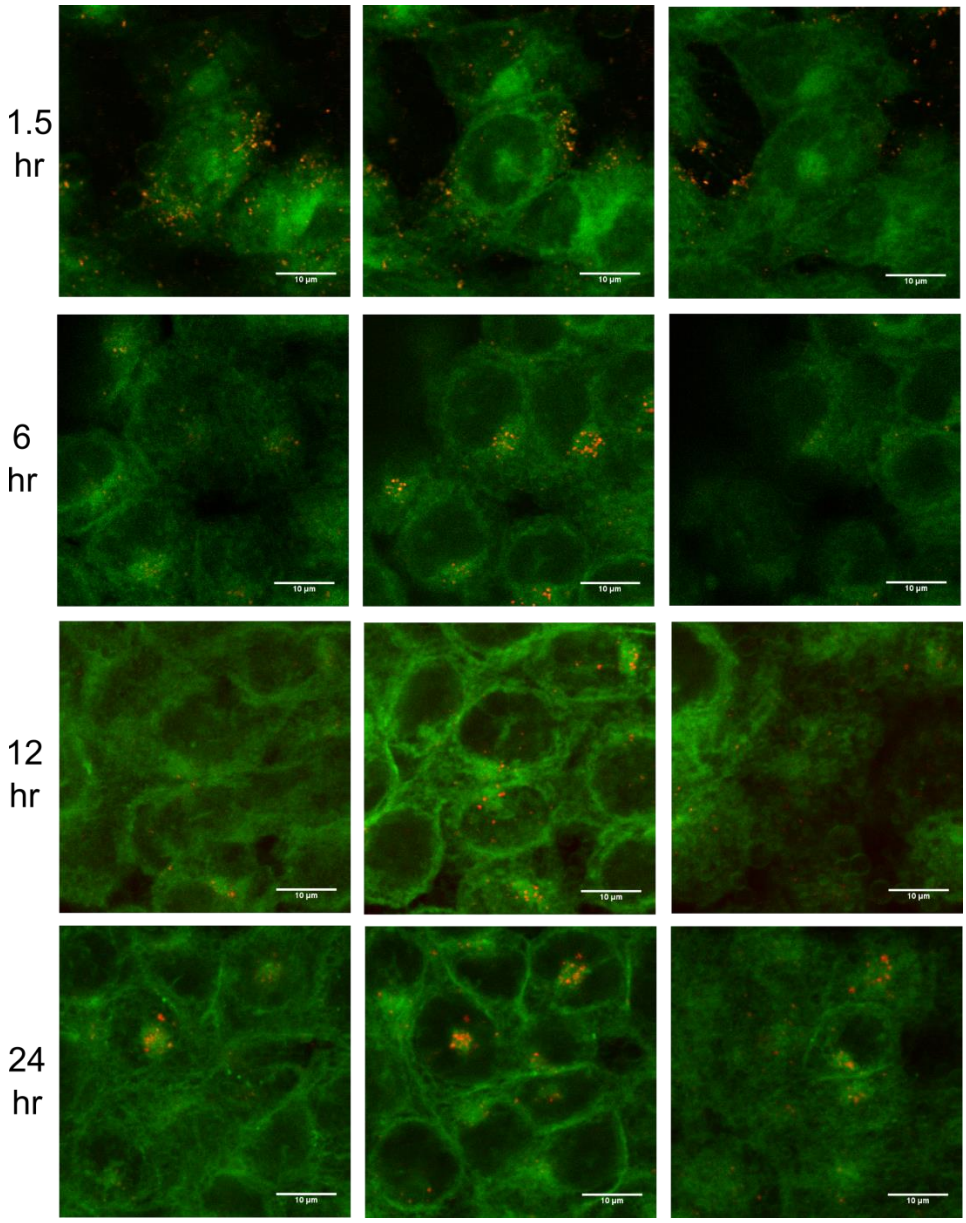

Figure 13: GNR Internalization. All sets show three images through the cell: left is the directly above the cells, middle is 4 µm to visualize inside the cell, right is 4 µm more to directly below the cell. The 1.5 hr incubated GNRs (red) were bound to the top, sides and bottom of cells (green, cell membrane). The 6 hr incubated GNRs were internalized into lysosomes within the cell. The GNRs were escaping from lysosomes into the cytoplasm at 12 hour GNR incubation. The final set shows GNRs internalized within the cell and accumulation in the perinuclear area near specific organelles after 24 hour GNR incubation

3.4.3 Gold Nanorod-Mediated Photothermal Threshold Determination

After determining the cellular location of GNRs at the specific time points, we performed photothermal therapy on the samples. To determine the fluence rate threshold, we conducted several rounds of experimentation, increasing the fluence rate (by 2.5 W/cm^2) until we detected signs of cell death using Trypan blue and bright-field imaging. This process is demonstrated in Figure 14 with a below fluence rate threshold image showing no cell death and at fluence rate threshold image, we can clearly perceive cell death. As controls, we incubated (1) cells with GNRs for 24 hours and irradiated (2) cells without GNRs with the NIR laser at 50 W/cm^2, both of which were shown not to induce cell death. We found that the fluence rate threshold for the 1.5, 3, 6, 12, and 24 time points were 47.5 W/cm^2, 45 W/cm^2, 40 W/cm^2, 40 W/cm^2 and 37.5 W/cm^2, respectively (Figure 15). The fluence rate thresholds were confirmed with three experimental replicates to show that each threshold was significantly different from the other time points. Therefore, we determined that the fluence rate threshold for damage decreases with increasing incubation time, as can be seen in Figure 15, which indicates a threshold dependence on GNR cellular localization.

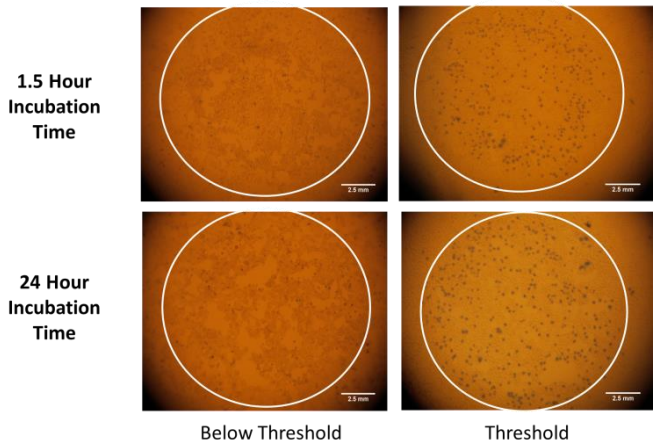

Figure 14: Cell Death Threshold. Showing that below the threshold at 1.5 and 24 hour GNR incubation points there is no cell death with Trypan blue but at the threshold we see cell death from Trypan blue.

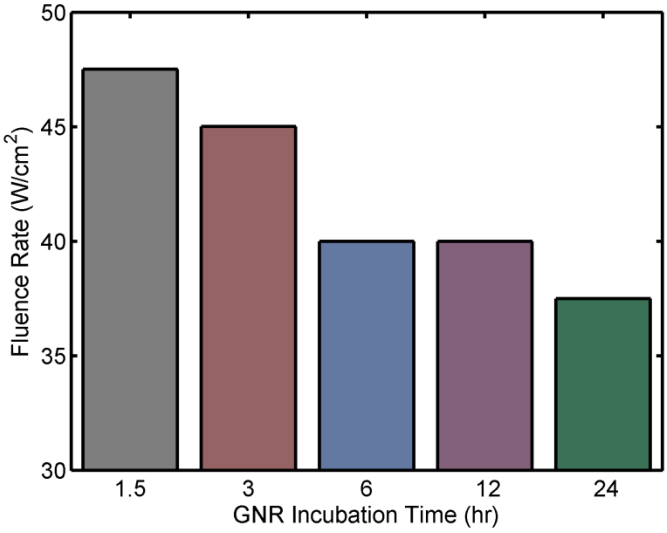

Figure 15: Cell Death Threshold dependence on GNR localization. The fluence rate at which cell death starts to occur depends on the GNR incubation time, which is shown to be directly proportional to the GNR localization

3.4.4 Quantitative Analysis of Cell Death Pathways

Next, after showing that the cell death is influenced by GNR cellular localization with Trypan blue staining, we quantitatively analyzed the cell death pathway response to GNR-mediated photothermal therapy using flow cytometry. For this experiment, we removed the GNRs after 1.5 hours incubation and let the cells incubate the rest of the exposure time (0, 4.5 and 22.5 hours post-GNR incubation) to allow for the cellular internalization processes to occur. We chose those time points, because they were significantly different in terms of GNR localization: membrane-bound (1.5 hours), aggregated in lysosomes (6 hours) and localized in the perinuclear region (24 hours). The extra step of removing GNRs after 1.5 hours of incubation was performed to avoid possible influences on threshold from final concentration differences in the cell after the GNR incubation. We performed flow cytometry on the cell samples after photothermal therapy to obtain quantitative values for the number of apoptotic and necrotic cells, and

we obtained log-log plots (Figure 16) with the apoptotic stain intensity on the x-axis and the necrotic stain intensity on the y-axis.

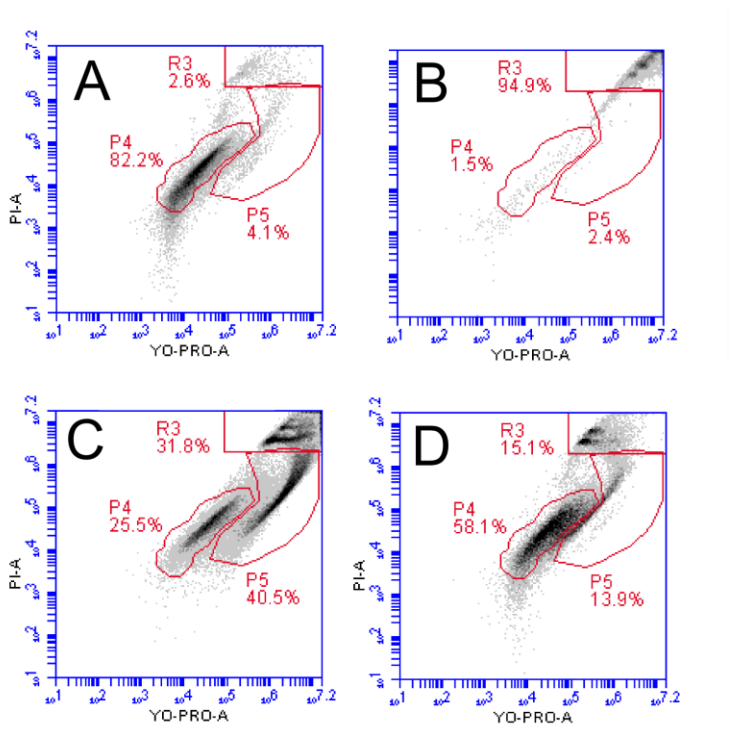

Figure 16: Flow Cytometry region determination. Log-log plot of fluorescence intensity, apoptosis stain (YP) on the x-axis and necrosis stain (PI) on the y-axis, (A) shows the negative control of only cells stained. (B) shows the necrotic positive control to determine the necrotic region. (C) shows the apoptotic positive control to determine the live, apoptotic and necrotic regions. (D) Representative sample of cells incubated with GNRs for 6 hours and exposed to 40 W/cm^2 irradiation.

After gating out the debris, we are left with three distinct regions, which are indicative of live cells, apoptotic cells and necrotic cells. To determine the three different cell regions, we performed control experiments using just stained cells (negative control), cells exposed to 1 hour of UV radiation (apoptotic positive control), and cells lysed with lysis buffer (necrotic positive control), as shown in Figure 16A, B and C respectively.

After determining the regions, we analyzed the cell samples after photothermal therapy and determined the percentage of cells (of the total in all three regions) for live, necrotic and apoptotic cells. These values were averaged over three replicates for 1.5, 6 and 24 hour time points over several fluence rates (35-50 W/cm^2) and compared to each other in bar plots (Figure 17).

From Figure 17 it is clear to see that the necrotic threshold (~50%) is highest for the shortest time point as was shown in the previous experiment. The necrotic threshold for the 1.5 hour time point was 50 W/cm^2 (close to the 47.5 W/cm^2 threshold for the previous experiment), the 6 hour was 47.5 W/cm^2 and the 24 hour was 42.5 W/cm^2. However, the apoptotic percentage was significantly less than the necrotic percentages. Apoptosis thresholds followed a similar trend as the necrotic thresholds, as the longer incubation times had a lower apoptotic fluence rate threshold. Furthermore, the longer incubation times had the higher apoptotic percentages at the threshold, ~18.5% for 24 hour incubation time at 37.5 W/cm^2 (~3x the control), ~13% for 6 hour incubation time at 40 W/cm^2 (~2x the control), and ~9.2% for 1.5 hour incubation time at 42.5 W/cm^2 (~1.5x the control).

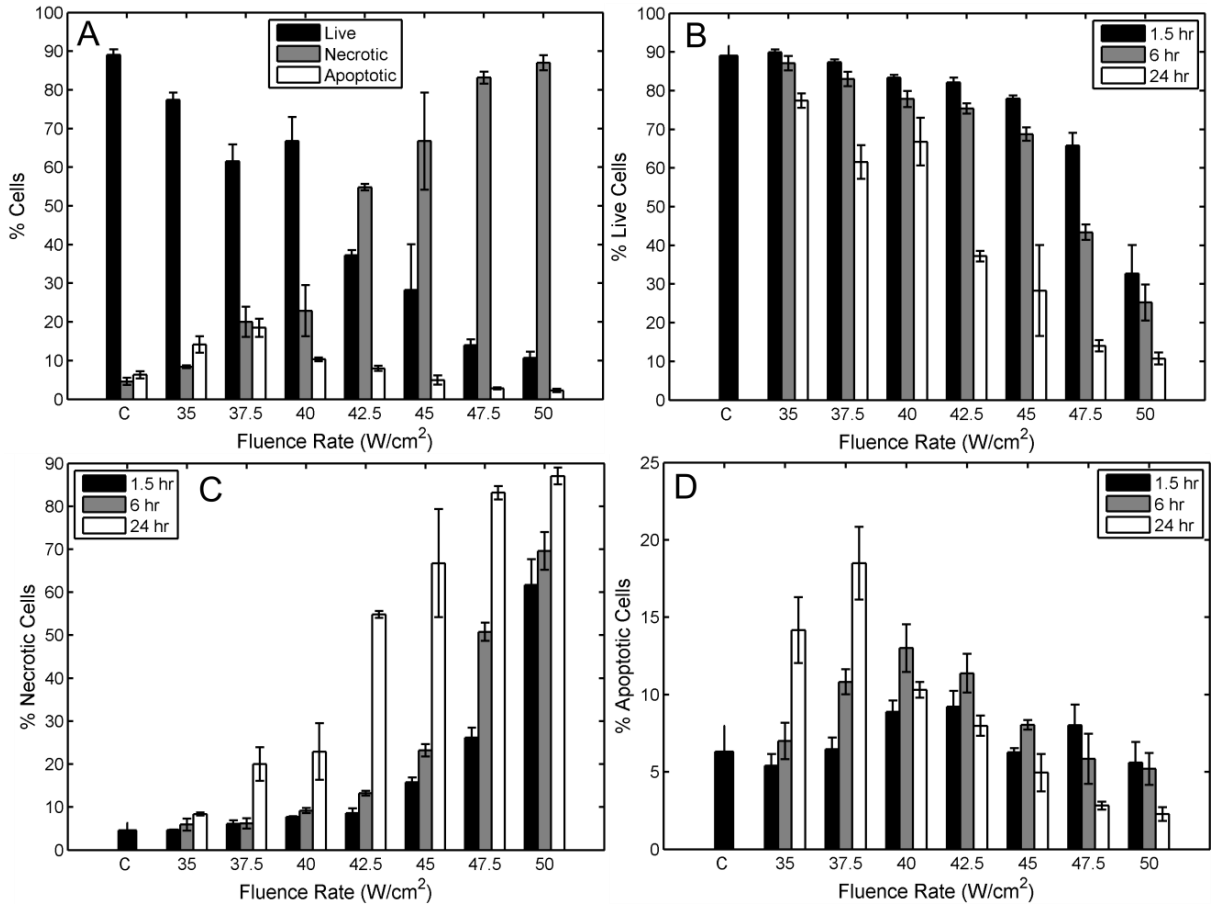

Figure 17: Quantitative Analysis of Cell Death Response to Photothermal Therapy. In (A) we see the 24 hour incubated GNRs live, necrotic and apoptotic percentages for several fluence rates and see the trends. In (B), (C), (D) we see the live, necrotic, and apoptotic cell percentages respectively with all three GNR incubation times compared together at several fluence rates.

3.5 DISCUSSION

3.5.1 Gold Nanorod Characterization

We successfully fabricated GNRs with CTAB on the surface and a size of 47 x 15 nm, measured by TEM image analysis. Thus, the peak SPR frequency was turned to 780 nm, which was sufficient for inducing photothermal damage and TPM imaging (Figure

12). All experiments utilized GNRs diluted to 0.5 OD at 808 nm for optimal absorption of the diode laser for photothermal therapy and comparison purposes.

3.5.2 Gold Nanorod Localization

Using two-photon imaging, we were able to determine the localization of the GNRs at several different time points. Our hypothesis that the GNRs would be found in different regions of the cell as the cellular internalization process progressed in time was shown to be correct. We believe this is due to CTAB on the surface, because it a cationic surfactant. Since the cells are negatively charged and the membrane is composed of lipids, the CTAB positive charge and lipophilic nature will be attracted to the cellular membrane, which is shown to start at the 1.5 hour time point and continue on at the 3 hour time point (Figure 13). The cell membrane allows the CTAB GNRs to transport through the membrane into the cell, possibly into lysosomes due to the positive charge, which starts in the 3 hour time point, but is more noticeable at the 6 hour time point (Figure 13). In fact, the GNRs at the 6 hour time point look to be aggregated and in small compartments, which seem to lysosomes. After the 6 hour time point we believe that the GNRs escape from the lysosome and the surface CTAB would attract the GNRs to organelles within the cell with lipid membranes, such as the nuclei and mitochondria (*72, 155*). The plasma membrane stain that we use is also lipophilic and when internalized will also localize to organelles within the cell with lipid membranes. In the 24 time points, the GNRs appear to be localized to the perinuclear region where the cell membrane stain is located within the cell, which we believe to be near mitochondria or nuclei (Figure 13).

3.5.3 Gold Nanorod Photothermal Threshold Determination

By visually inspecting the thresholds at which cell death was determined for different GNR incubation times (Figure 15) clearly indicates that photothermal therapy depends on incubation time, which is correlated with the localization. The fluence rate difference between the 1.5 hour and 24 hour GNR incubation is 10 W/cm^2, which is significant compared to the 2.5 W/cm^2 step size in determining the threshold over four replicates. As a result, we believe that inducing cell damage through GNR-mediated photothermal therapy is influenced by GNR localization. However, we believe that it is possible that this result could be skewed with the final GNR concentration varying between the different time-points. We believe this may occur because the longer GNR incubation times leads to a longer cellular exposure to the GNRs and consequently more GNRs could be taken up by the cells. Therefore, based on other studies and this work, we believe that the final GNR concentration in the cells could be an issue that has not been explored (*72, 73*). Subsequently, for the cell death pathway experiments we incubated the GNRs for only 1.5 hours (the smallest time point), then removed the media and allowed the cells to incubate in fresh media for the remainder of the time point. By following this procedure, we were assured that the concentration would be the same for all time points.

3.5.4 Quantitative Analysis of Cell Death Pathways

To illustrate a more accurate understanding of the cell death pathway response to photothermal therapy we obtained quantitative values of the number of apoptotic, necrotic and live cells (Figure 17). The live cell percentage decreases consistently, for all incubation times, as the fluence rate increases with cell death produced by different ratios of necrosis and apoptosis. Consequently, necrosis increases, for all incubation times, with fluence rate increases. After the necrotic threshold, defined as the fluence rate when the necrosis percentage is greater than 50%, necrosis is the dominant cell death pathway. As

shown in Figure 17, the 24 hour time point, internalized GNRs localized to organelles, has the lowest fluence rate at the necrotic threshold and the 1.5 hour time point, membrane-bound GNRs, has the highest fluence rate at the threshold.

This result is contrary to the study performed by Wei and coworkers; however, we believe that the differences in the experiment, that we use a CW laser and that we have a quantitative measurement of the amount of necrotic cell death, can explain these differences (*72*). The authors used a pulsed laser in CW mode, which involves a scan of laser pulses over a larger area with approximately 0.126 ms exposure for each nanorod. This is a quasi-CW mode, at the equivalent of millisecond pulses at each point, and could induce photodestructive effects instead of only thermal effects due to the extremely small GNP relaxation time (~0.6 ns) (*81*). Secondly, the authors assessed cell death subjectively using qualitative measures such as imaging the ethidium bromide stain and visually inspecting for membrane blebbing, which the authors state indicates necrosis but as discussed in Chapter 1, is actually representative of both necrosis and apoptosis. Qualitative measures for detecting cell death were also used by El-Sayed and coworkers when demonstrating that cytoplasmic gold nanoparticles required less energy to induce cell death than nuclear localized gold nanoparticles (*73*). We believe the heating profile of the internalized GNRs can induce cell death at lower fluence rates because the thermal energy is localized and spreads evenly throughout the cell to induce cell death through other mechanisms than just membrane lysis, such as the perturbation of the nuclei or mitochondria.

We found that for all time points there was a common trend for the apoptotic percentages. Essentially, the apoptotic percentage increased to a maximum value and decreased at or before reaching the fluence rate at the necrotic threshold. This indicates that there is an apoptotic threshold at which apoptosis and necrosis have approximately

equal contributions to cell death, which is consistently at a lower fluence rate than the necrotic threshold. When the necrotic threshold power is reached, necrosis becomes the dominant cell death pathway with a reduction in the number of apoptotic cells. We observed the maximum apoptotic percentage with the 24 hour incubated GNRs, around $3x$ the control, which we believe is because the GNRs were localized to the nuclei/mitochondria, due to their influence on the apoptotic pathway (*155*). The 1.5 hour time point had the lowest amount of apoptosis, which we believe is due to the membrane localization where the heating would elicit membrane damage and induce necrosis. Therefore, we also demonstrated that the initiation of apoptosis is affected by GNR localization during photothermal therapy.

3.5.5 Comparison to Relevant Work

In our study, we found the apoptotic percentage to be lower than the necrotic percentage, but it is significantly increased from the control, $1.5x$ for 1.5 hour, $2x$ for 6 hour, and $3x$ for 24 hour time points. In cancer, the apoptotic pathway is inhibited such that unregulated proliferation can occur, which may cause resistance to apoptosis in certain cancer types. Therefore, several previous studies have also explored the effectiveness of these anti-cancer therapeutics with different cancer types that may be resistant or augmented with processes that attempt to normalize the cell apoptotic pathway. However, studies have performed flow cytometry to measure apoptotic percentage with anti-cancer therapeutics, such as doxorubicin, tumor necrosis factor-related apoptosis inducing ligand (TRAIL), CD95, and non-steroidal anti-inflammatory drugs, These studies have observed induced apoptosis percentages for these anti-cancer drugs and therapeutics ranged from 10-40% depending on the effectiveness of the therapeutic to the specific cell type (*121-124*). Therefore in comparison to our study, we

see that the apoptosis 6 and 24 time points, ~13% and ~18.5% respectively with colon cancer cells, are in the range seen for anti-cancer therapeutics, which could even vary for different cell types. We believe that this indicates that for GNR-mediated photothermal therapy at those time-points and at fluence rates at the apoptotic maximum, we can achieve a similar anti-cancer therapeutic effect. If total cell death was the goal of a study, without specifically desiring apoptosis or necrosis, the optimal parameters for photothermal therapy would be the fluence rate with the highest cell death. However, our goal was to induce apoptosis as a significant portion of the cell death. Therefore, we can consider these points as the optimal parameters for GNR-mediated photothermal therapy for limiting the extracellular damage in terms of having maximum apoptosis with also causing significant cell death.

Chapter 4: Cell Death Pathways Initiated during Gold Nanorod-mediated Photothermal Therapy in 3D Multicellular Tumor Spheroids

4.1 INTRODUCTION

In continuing this extensive study, we quantitatively analyzed the cell death response to GNR-mediated photothermal therapy assessed in MTS as an *in vitro* tumor model with two different GNR delivery methods. Using the agarose-coated 96 well plate method, the colon cancer cells were forced to aggregate to each other and form MTS. GNRs were delivered to the MTS in two different ways: (1) co-incubated with the MTS at the time of inception, which we projected to form a uniform distribution, and (2) incubated for 24 hours for a distribution representative of *in vivo* photothermal studies, which we anticipated to only be localized in the MTS periphery. After PTT irradiation, we quantitatively analyzed MTS cell response for apoptosis and necrosis using flow cytometry. We expected that apoptosis and necrosis percentages will be higher for the uniform GNR distribution. However, due to the coupling and enhanced absorption effect of aggregated GNRs limited only to the periphery, we observed that the necrotic and apoptotic damage threshold was lower for the 24 hour incubated GNRs than the co-incubated GNRs. Furthermore, in comparison to 2D monolayer quantitative analysis studies of cell death response to photothermal therapy performed earlier, we found that there is overall less cell death, both apoptosis and necrosis, in MTS than the 2D monolayer due to increased cell-cell and cell-ECM interactions. This study aims to show that 3D cell culture, MTS, is an advantageous model for analytically understanding the cell death response to GNR-mediated photothermal therapy.

4.2 RELEVANT WORK

Several groups recently have investigated nanoparticle interactions with MTS, primarily studying the nanoparticle penetration with varied conditions. Similarly, few groups have modeled the nanoparticle diffusion and penetration in MTS (*137, 159*). One group explored the uptake enhancement of polystyrene nanoparticles in MTS conjugated with collegenase to degrade ECM proteins, which allowed to particles to travel further into the MTS rather than just the MTS margin with the unconjugated nanoparticles (*140*). Another study explored the dependence of size on ultrasmall gold nanoparticle (2-15 nm) penetration into MTS. The authors found that the smaller nanoparticles (2 nm) were more evenly distributed throughout the MTS and were internalized into the cells more than the larger nanoparticles, which were mostly located in the MTS edge (15 nm) (*160*). Several papers have also explored encapsulating drugs into synthetic micelles and finding that the therapeutic effect was limited by penetration ability of the drugs and micelles, similar to our study (*161, 162*).

The cell death pathway response to known toxic nanoparticles, (1) CdTe and (2) CTAB gold nanoparticles has been explored with 2D and 3D cell culture (*158*). The authors demonstrated that the nanoparticle toxicity to 3D cell culture was substantially less than with 2D monolayers for both necrosis and apoptosis, as was seen in our study, conceivably because of the limited penetration of the nanoparticles as well as the cell-cell and cell-ECM interactions increasing cell repair function. Furthermore, the authors observed that, after exposure to the nanoparticles, apoptosis and necrosis values changed dramatically with time as cells moved from apoptosis to secondary necrosis. As a result of this study, we have performed all quantitative experiments at 1 hour after laser exposure to match the observed peak of apoptosis detection in that experiment.

Two different groups have studied gold nanoshell-loaded tumor associated macrophage MTS penetration and photothermal therapy (*163, 164*). Using breast cancer MTS as a hypoxic tumor model, the authors showed that nanoshell-loaded macrophages penetrated into the MTS periphery and, after laser irradiation, imaged cell death only near the nanoshell-loaded macrophages localization in the MTS (*164*). The other group used nanoshell-loaded macrophages, due to their ability to pass through the blood-brain barrier, to treat a glioma MTS model. The authors created two glioma MTS models: similar to the first study, a normal (1) MTS containing glioma cells and the macrophages infiltrated into the periphery, and (2) hybrid, which mixed nanoshell-loaded macrophages within the MTS with the glioma cells to simulate a uniform distribution, similar to our co-incubated MTS model. Using a continuous wave laser at a single fluence rate, the authors found that for both the hybrid and infiltrated MTS, they could completely suppress growth and visualized significant cell death (*163*).

Another group examined the surface chemistry-dependent GNR penetration and photothermal therapy of MTS (*165*). The authors found that positively-charged GNRs accumulated more in the MTS, but the negatively-charged GNRs penetrated further into the MTS. In our study, we use positively-charged GNRs due to the residual CTAB on the GNR surface. After photothermal therapy, the authors measured the cell death, using acid phosphatase assay, and found that the negatively-charged GNRs had more cell death per particle than the positively-charged particles, most likely due to the deeper penetration.

4.3 MATERIALS AND METHODS:

4.3.1 Multicellular Tumor Spheroid Formation

Human colorectal tumor cells (HCT-116, ATCC, Manassas, VA) were seeded in T25 flasks with cell culture media composed of McCoy's Modified Medium (Corning

CellGro, Corning, NY) supplemented with 10% fetal bovine serum (FBS) and 1% penicillin-streptomycin-amphotericin B (Lonza, Basel, Switzerland) at 37°C with 5% CO_2. After the cells reached confluence, we detached the cells with 0.5% trypsin solution (Thermo Scientific HyClone, Waltham, MA) and centrifuged at 600 RPM for 5 minutes. For MTS formation, we seeded 1500 cells per well into agarose-coated 96-well plates as reported by Friedrich et al, replacing the cell culture media every 3-4 days (*130*). The 96-well plate is coated with 1.5% sterilized agarose type III (Sigma Aldrich, St. Louis, MO) to provide a non-adherent surface forcing the cells to aggregate into the center of each well, and was incubated in a humidified atmosphere with 5% CO_2 at 37°C after being sealed with plastic paraffin film (Parafilm, Bemis Flexible Packaging, Neenah, WI). To determine size and integrity, we visually inspected the MTS daily under a bright-field microscope and took images.

4.3.2 Gold Nanorod Synthesis

We followed the same gold nanorod synthesis as previously done by Nikoobakht et al and Jana et al in a Ag(I) –assisted growth method (*145, 157*). Briefly, we made an aqueous gold seed particle solution is prepared by adding 250 µL of 0.01 M $HAuCl_4$ (Sigma Aldrich, St. Louis, MO) to 9.75 mL of aqueous 0.1 M cetyl trimethylammonium bromide (CTAB, Sigma Aldrich, St. Louis, MO) solution in a vial, while stirring. Then we made a 0.01 M $NaBH_4$ (CTAB, Sigma Aldrich, St. Louis, MO) solution by placing DI water in a vial, equilibrating it in an ice bath, adding the $NaBH_4$, and mixing it rapidly. 600 µL of the aqueous 0.01 M $NaBH_4$ is added to the gold seed particle solution and stirred for 2 min. Next, an aqueous growth solution is prepared by combining 9.5 mL of 0.1 M CTAB, 75 µL of 0.01 M $AgNO_3$ (Sigma Aldrich, St. Louis, MO), 500 µL of 0.01 M $HAuCl_4$, and 55 µL of 0.1 M ascorbic acid (Sigma Aldrich, St. Louis, MO) in a 15 mL

centrifuge tube. Upon adding ascorbic acid, we inverted the tube two times to mix, and the solution became colorless due to partial reduction of the gold salts. 12 μL of the gold seed solution was then added to this growth solution followed by slowly inverting it two times to mix, and it was incubated at 27 °C overnight without stirring. The resulting GNR solution was centrifuged three times at 8000 RPM for 20 minutes to remove excess CTAB, which would cause cytotoxicity if left in solution, and concentrated the solution in 15 mL of DI H_2O. We measured the dimensions by averaging over 300 individual particles analyzed in ImageJ (NIH Bethesda, MD) using transmission electron microscopy (TEM, FEI Tecnai, Hillsboro, OR) images (inset of Figure 18), which were measured to be 47 x 15 nm. We measured the optical density (OD) or absorbance of the solution using a UV-Vis Spectrophotometer (Beckman Coulter DU720, Brea, CA) as shown in Figure 18.

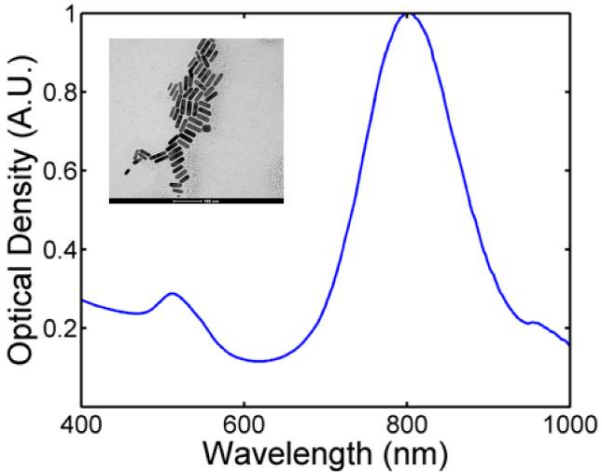

Figure 18: Absorption spectra for fabricated gold nanorods. Inset: TEM image of fabricated gold nanorods

4.3.3 GNR Delivery Techniques

We used two different delivery techniques: co-incubation and 24 hour incubation. During co-incubation, the GNRs are seeded simultaneously with the HCT-116 cells at the

beginning of MTS formation and allowed to incubate with the cells as the MTS grows. For 24 hour incubation, the GNRs were incubated for 24 hours with the spheroids on day 6 of growth, due to it best mimicking *in vivo* tumors at this time-point (as discussed in a later section). For both delivery techniques the GNRs are incubated with spheroids at 0.05 OD mixed with fresh cell culture medium, which was found to be a non-toxic concentration.

4.3.4 Two-Photon Imaging for GNR distribution

After incubating the GNRs with the MTS in two different techniques, we utilized TPM to determine the GNR distribution. To prepare for staining, we removed the GNR media from each well and washed with PBS (phosphate buffered saline) to ensure no residual GNR binding, and fixed the MTS in 4% paraformaldehyde (PFA, Sigma Aldrich, St. Louis, MO) for 10 minutes. Then we stained the MTS with the CellMask plasma membrane stain (Life Technologies, Carlsbad, CA) for one hour, to allow for MTS stain penetration for visualizing the MTS and understanding where the GNRs reside with respect to the cellular matrix. Then we mounted the MTS onto concave slides with Vectashield (Vector Laboratories, Burlingame, CA), which were sealed with nail polish.

Imaging was performed with TPM (Prairie Technologies, Middleton, WI) utilzing an ultrafast pulsed femtosecond tunable Ti:Sapphire laser (Spectra Physics Mai-Tai, Irvine, CA). The laser excitation was tuned to 750 nm, to detect the plasma membrane stain, and 800 nm, to detect the GNRs. For detecting the emitted light, photomultiplier tubes (PMTs) were used with a 660 nm +/- 20 nm bandpass emission filter for the gold nanorods (Channel 1) and 595 nm +/- 50 nm bandpass emission filter for the plasma membrane stain (Channel 2). The cells were imaged with a water-immersion 20x and 60x objectives (Olympus) with 1.0 NA allowing for a high resolution and high magnification.

We obtained single images and Z-stacks by imaging through the MTS in 10 μm increments, all of which were taken with the proprietary software (PrairieView) and analyzed using ImageJ (NIH, Bethesda, MD).

4.3.5 Photothermal Therapy

For the photothermal therapy experiments, the MTS were washed with PBS after removing the GNRs for each respective delivery technique. Then we irradiated the MTS with an 808 nm CW diode laser for 5 minute duration. The fiber-coupled laser was focused to a spot size of 1.6 mm diameter using a series of biconvex and aspherical lenses. The laser fluence rate ranged from 30-50 W/cm^2, increasing in increments of 5 W/cm^2, to quantitatively determine the threshold at which cell necrosis and apoptosis occurs. After photothermal therapy is done, the MTS are prepared for flow cytometry.

4.3.6 Flow Cytometry

To quantitatively analyze cell death pathway response to photothermal therapy we use flow cytometry one hour after laser irradiation, due to apoptosis being a time-dependent process and achieving its maximum at that time-point (*158*). We broke down the MTS ECM by adding 0.5% trypsin to the MTS for 15-20 minutes, and pelleted the MTS cells by centrifuging at 600 rpm for 5 minutes. Then we replaced the supernatant with the staining solution composed of YO-PRO-1 (YP, Life Technologies) and propidium iodide (PI) and incubated for 30 minutes on ice. YP is a carbocyanine nucleic acid stain that can permeate into apoptotic cells, while propidium iodide can permeate into any cell with membrane damage, namely necrotic cells. To quantitatively measure the YP and PI fluorescence we used a flow cytometer (BD Accuri C6, Franklin Lakes, NJ) with PMTs utilizing a bandpass emission filter at 530 nm +/- 15 nm (FL1) for YP and long-pass emission filter at 670 nm (FL3) for PI. The cells are sorted according to

their fluorescence profile. Cells that are alive have low amounts of YP or PI fluorescence. Apoptotic cells have only moderate YP fluorescence and necrotic cells have high YP and PI fluorescence. The disparity between necrotic and apoptotic cells is compared between co-incubated GNR MTS, 24 hour incubated MTS, positive and negative controls. As a control, we used stained cells with no external factors (negative control), cells exposed to 1 hour of UV radiation (apoptotic positive control) and cells exposed to 30 minutes of lysis buffer (Promega, Madison, WI).

4.4 RESULTS:

4.4.1 Multicellular Tumor Spheroid Growth Analysis

In this study, we successfully formed MTS using the agarose-coated 96 well plate method as described earlier. We analyzed the MTS by taking bright-field images and measured the diameter every 24 hours until the MTS growth stalled, which was around day 20 (Figure 19). The inset of Figure 19 shows the bright-field images over several days to show cell aggregation and MTS growth. MTS have different three different regions of growth: (1) exponential growth (day 3-5 after seeding), (2) linear growth (day 6-15), and (3) stalled growth (plateau region seen in days 16-21), which is seen in Figure 19 (*130*). Based on the MTS growth curve, we chose day 6 for experimentation because of its location in the linear region.

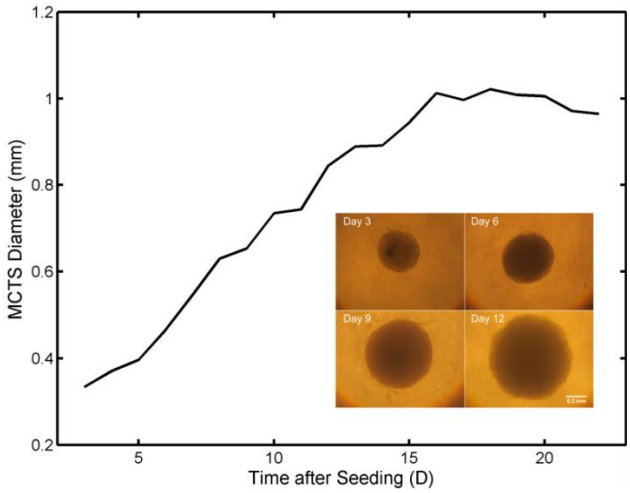

Figure 19: MTS growth curve. Measured MTS diameter increasing over time through three different regions: (1) from day 3-5 in the exponential region, (2) from day 6-15 in the linear region, and (3) from day 16-21in the plateau region. Inset shows MTS images from Day 3, Day 6, Day 9 and Day 12.

4.4.2 Gold Nanorod Penetration in Multicellular Tumor Spheroids

Subsequently, we incubated GNRs with the MTS using the two different delivery methods and performed TPM imaging to determine GNR penetration and uptake. Figure 20 is composed of TPM slices at the top ($Z = 0$), upper half, bottom half and bottom of the MTS to illustrate the GNR penetration (red) in the MTS, stained with a cell membrane stain (green), GNRs incubated for 24 hours (Figure 20A) are only found in the MTS periphery as expected. In the first slice (Figure 20A) the GNRs are spread out since the whole MTS top area is exposed to the GNRs in media; however, as we imaged into the MTS the GNRs appear to only be in the outer edges. Therefore, it is apparent that the GNRs do not penetrate deep into the MTS. In Figure 20B, we see a representative MTS with co-incubated GNRs. The GNRs appear to penetrate further into the MTS. In the 2nd and 3rd slices (Figure 20B), the co-incubated GNRs are unmistakably further than in the 24 hour incubated on both sides of the MTS.

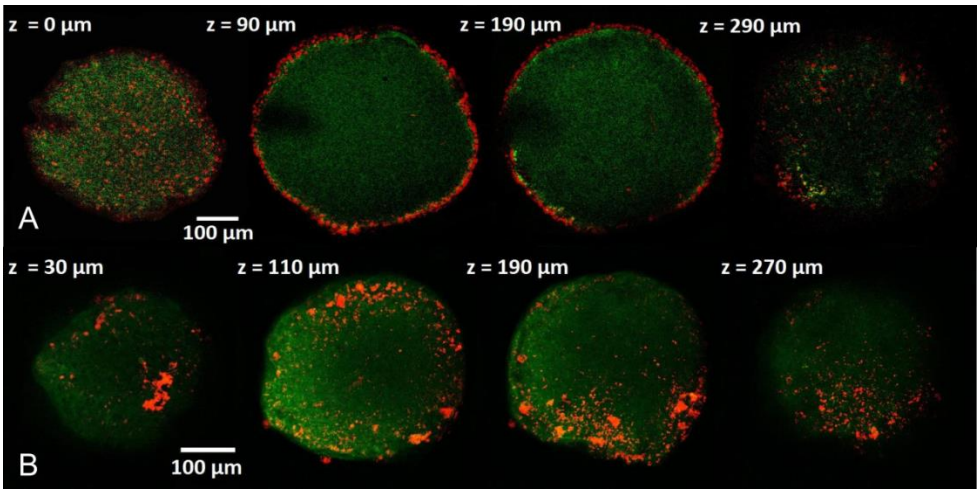

Figure 20: MTS Slices showing GNR Distribution. For both sets, we have 4 images going through the spheroid in the z-direction, showing the top, two images in the middle and bottom of the MTS. In (A), we see the 24 hour incubated 24 hours are localized to only the MTS periphery. In (B), the co-incubated are shown to be distributed somewhat uniformly through the MTS.

Next, we quantitatively analyzed the images to determine the respective penetrations for the two GNR delivery methods. Images taken with the TPM GNR channel were thresholded to allow only GNRs to be visible and analyzed (Figure 21). To analyze the penetration, we divided the MTS into 5 concentric rings separated using segments equivalent to 20% of the total radius and counted the accumulation in each region. GNRs incubated for 24 hours (Figure 21A) are distinctly found only in the outer ring, limited to the first 20% of the MTS radii. The co-incubated GNR distribution is much more complex due to the widespread GNR accumulation as seen in Figure 21B.

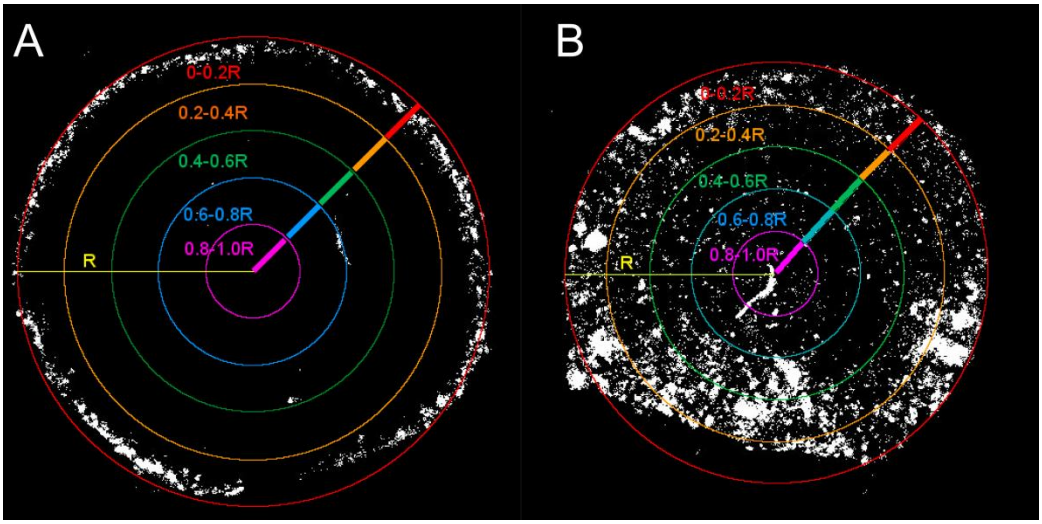

Figure 21: GNR Penetration in MTS. Thresholded images of GNR images showing the penetration into different MTS regions divided by 20% radii segments. For (A), we see that the 24 hour incubated GNRs are found primarily in the first 20% segment. For (B) the co-incubated GNRs are found distributed throughout the MTS.

Moreover, we plotted (Figure 22) the percentage of total GNRs in each ring normalized to their respective ring area due to outer rings being larger than the inner rings. In Figure 22, we see that the 24 hour incubated GNRs are only found in the first 20% of the MTS. Conversely, the co-incubated GNRs accumulated slightly higher in the first 20% of the MTS but are relatively evenly distributed within the ensuing four regions. Thus, this shows that the two GNR delivery techniques have statistical differences ($p < 0.01$) in MTS distribution, which are clearly seen in the quantitative analysis of the data.

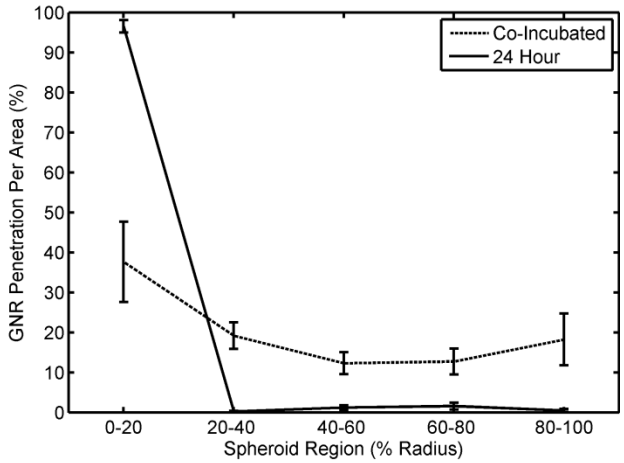

Figure 22: Quantification of GNR penetration per MTS Area Region. Using the thresholded image, we determine the GNR intensity values for each MTS region divided by the total GNR intensity values to obtain GNR penetration percentage normalized by the total MTS region area. We see the 24 hour incubated GNRs are only located in the first 20% of the MTS, whereas the co-incubated GNRs are found to be distributed throughout the MTS.

4.4.3 Gold Nanorod Localization in Multicellular Tumor Spheroids

Taking advantage of the high axial and lateral resolution of TPM, we desired to determine the locations of the GNRs on the cellular level. Figure 23A and B are high magnification images of the co-incubated GNRs (red) close to the center of the MTS. The GNRs are seen to be distributed throughout and highly aggregated but mostly found in the ECM between cells, however, in Figure 23B when we magnify even further GNRs are shown to be internalized in some cells. The 24 hour incubated GNRs (Figure 23C and D) show GNRs located near the MTS periphery. The GNRs seem to be less aggregated in clumps, probably due to the shorter incubation time. In addition, the GNRs appear to be both internalized and distributed in the ECM evenly, such that there is more internalization for the 24 hour incubated GNRs than the co-incubated GNRs.

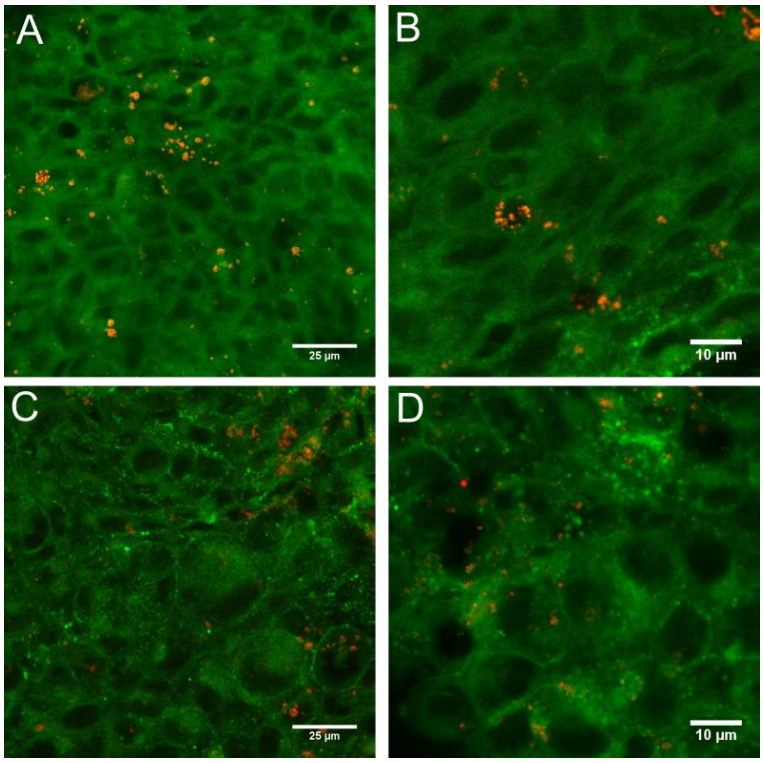

Figure 23: High Magnification images of GNR uptake in cells. We show co-incubated GNRs (A and B) and 24 hour incubated GNRs (C and D). Most co-incubated GNRs are found in the ECM and with the 24 hour incubated the GNRs appear to be evenly distributed between being found in the ECM and internalized in cells.

4.4.4 Gold Nanorod-Mediated Photothermal Therapy of Multicellular Tumor Spheroids

After observing the GNR locations of the two delivery techniques, we performed photothermal therapy on the GNR-incubated MTS. To visualize MTS damage during photothermal therapy we took bright-field images one day before and one day after laser irradiation (Figure 24). As compared to normal growth in Figure 19, the MTS was completely destroyed at 40 W/cm^2 for both GNR delivery methods, 24 hour incubated GNRs and the co-incubated GNRs. We observed that the MTS has become less dense, lost structural integrity and the cells seem to spread throughout the well. Since the cells

start spreading the MTS diameter cannot be measured effectively using the bright-field microscopy technique used in Figure 19, therefore, we employ a more quantitative assessment of cell death.

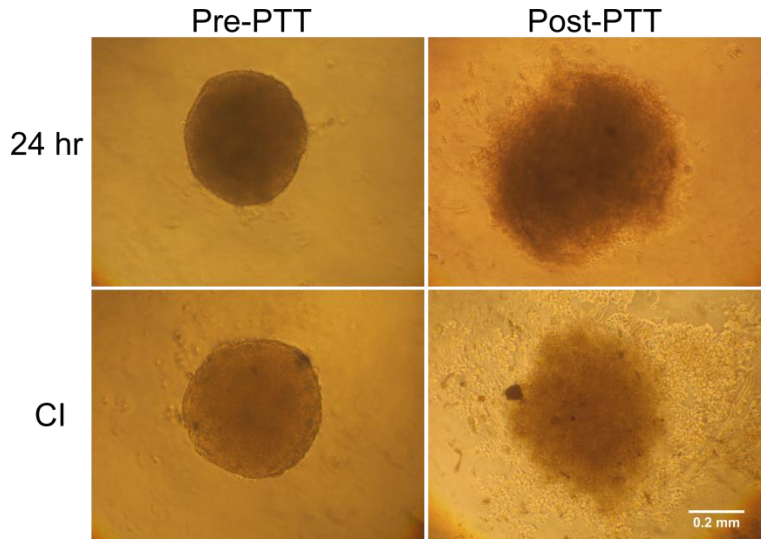

Figure 24: MTS structural integrity after photothermal therapy. After 40 W/cm^2 irradiation we see that the MTS are destroyed and lose structural integrity for both 24 hour and co-incubated GNRs.

4.4.5 Quantitative Analysis of Cell Death Pathways

After laser irradiation and cell death pathway staining, we performed quantitative analysis on the cells using flow cytometry. The device recorded the apoptotic (YP) and necrotic (PI) stain intensity for all cells and we plotted the intensities against each other with apoptosis on the x-axis and necrosis on the y-axis (Figure 25). Cells that are alive have low amounts of YP or PI fluorescence. Apoptotic cells have only moderate YP fluorescence and necrotic cells have high YP and PI fluorescence. To separate out the different regions of live, apoptotic and necrotic cells we performed control experiments. In Figure 25B, as a positive control we induced necrosis by using a cell lysis buffer to find the region of necrotic cell death, which indicates ~96% cell necrosis. As another

positive control (Figure 25C), we induced apoptotic cell death by exposing the MTS to ultraviolet light for one hour and let the MTS incubate for an hour before staining. In this control, the cells are evenly distributed between live, necrotic and apoptotic. Therefore, using this data we were able to define the appropriate regions for live, apoptotic and necrotic cells. In Figure 25A, we show the stained MTS negative control with no GNR or laser exposure, which has ~28% necrotic cell death, ~1.2% apoptotic cell death and primarily ~66% of the cells are live based on the determined regions. In Figure 25D, we show a representative sample of MTS with 24 hour incubated GNRs exposed to 40 W/cm^2 laser irradiation. In this case, the live cell percentage is 37.7% and the cell death was divided between 44.4% necrotic and 14.3% apoptotic cell death.

After determining the regions to divide live, necrotic, and apoptotic cells, we quantitatively analyzed the respective percentages (with standard error over four replicates for each sample) for a fluence rate range (30-50 W/cm^2) for both GNR delivery techniques (Figure 26). The 24 hour incubated GNR (Figure 26A) live cell percentage decreases with increasing fluence rate as expected. The necrotic cell percentage increases significantly between 30 and 35 W/cm^2 laser irradiation, which can be designated the necrotic threshold. From there the necrotic percentage continues increasing at increasing fluence rates, yet at a smaller slope. The apoptotic percentage increases to a maximum (~13%) at 35 W/cm^2 but decreases afterwards as necrosis becomes the dominant cell death pathway at higher fluence rates due to the larger temperature increases.

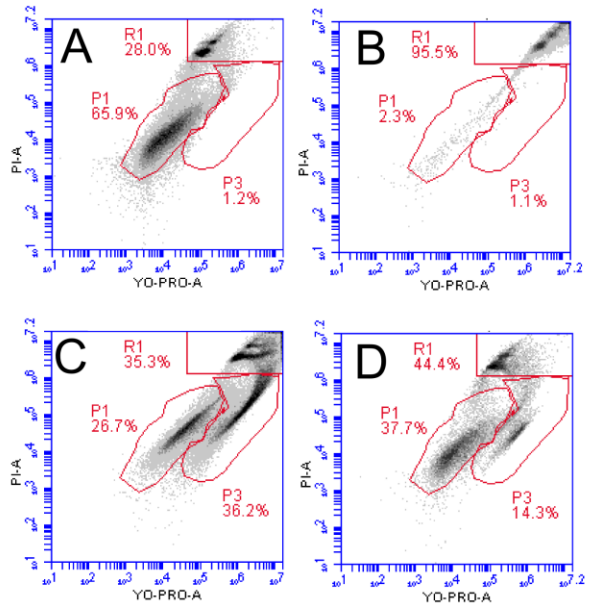

Figure 25: Flow Cytometry region determination. Log-log plot of fluorescence intensity, apoptosis stain (YP) on the x-axis and necrosis stain (PI) on the y-axis, (A) shows the negative control of only the MTS stained. (B) shows the necrotic positive control to determine the necrotic region. (C) shows the apoptotic positive control to determine the live, apoptotic and necrotic regions. (D) Representative sample of MTS incubated with GNRs for 24 hours and exposed to 40 W/cm^2 irradiation.

We observed similar trends with MTS contained co-incubated GNRs (Figure 26B). However, the necrotic cell death percentage increased significantly at a higher fluence rate, between 35 and 40 W/cm^2, than the MTS incubated with GNRs for 24 hours (Figure 26C). Although, from 40 to 50 W/cm^2 the necrotic cell death percentages increased at a steeper slope than the 24 hour GNR delivery method, most likely due to the differences in the distribution. The co-incubated GNR apoptotic percentages followed the same trend as the 24 hour incubated GNRs (Figure 26D), increasing till it reached a maximum (~16%) at 40 W/cm^2 and decreased afterwards. Additionally, the apoptotic percentage for co-incubated GNRs did not decrease as dramatically as the MTS with 24

hour incubated GNRs. Interestingly, both the maximum necrotic and apoptotic cell death percentages were higher for the MTS damaged by co-incubated GNRs than 24 hour incubated GNRs (Figure 26C and D), suggesting that the cell death pathway response is dependent on the GNR location in the MTS.

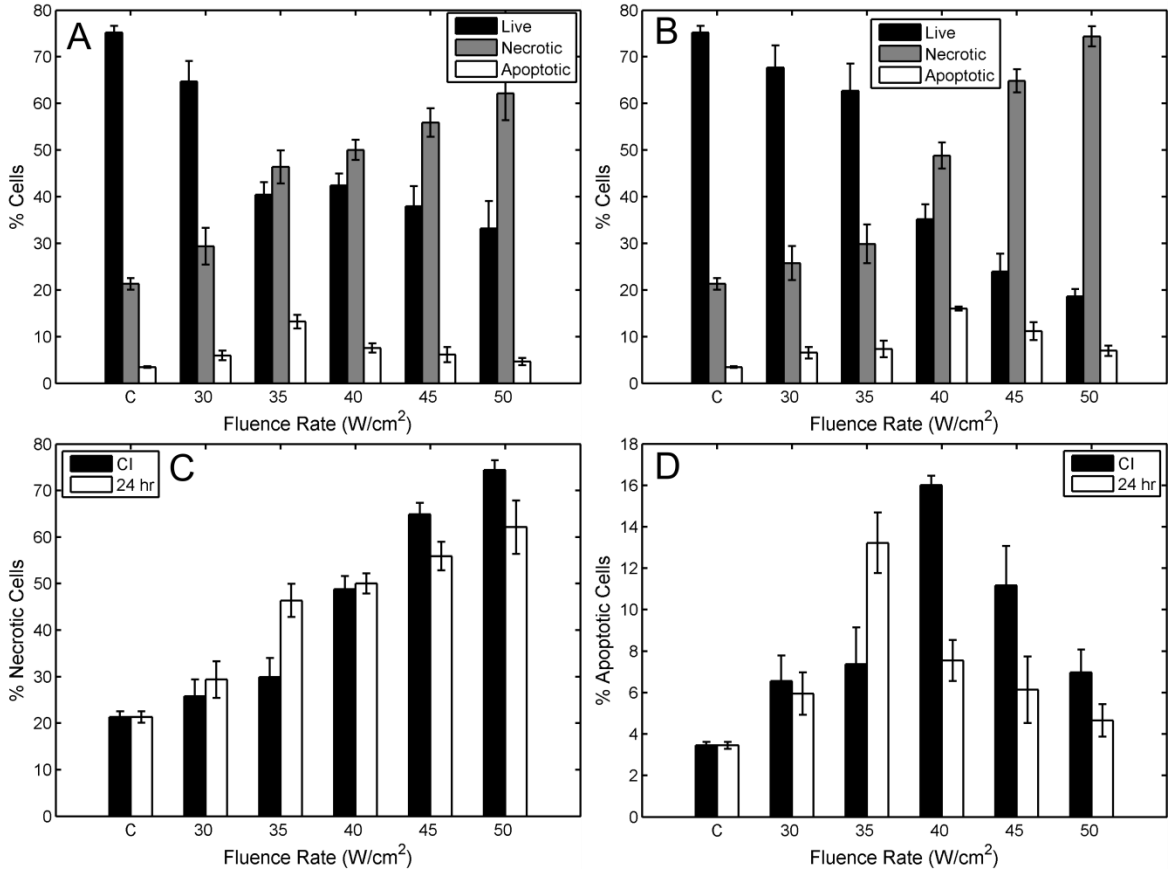

Figure 26: Quantitative Analysis of Cell Death Response to Photothermal Therapy. In (A) and (B) we see the 24 hour incubated and co-incubated GNRs, respectively, with the live, necrotic and apoptotic percentages for several fluence rates and see the trends. In (C) and (D) we see the necrotic and apoptotic cell percentages respectively with both GNR delivery techniques compared together at several fluence rates.

4.5 DISCUSSION

4.5.1 Multicellular Tumor Spheroid Growth Curve

Understanding the MTS growth curve allowed us to choose the optimal experimentation time. We found that the MTS grew in 96 well plates to similar sizes due to the initial cell concentration incubated and the same growth environment for repeatable experimentation. The first growth region is the exponential growth region, in which the MTS has not fully formed a dense structure, which it achieves around day 3 (Figure 19). Due to small size and ability of nutrients to reach all cells in the MTS the growth is exponential until approximately day 5. The linear region indicates that there is the beginning of necrotic core formation as the MTS gets larger and the nutrients from the FBS and media cannot penetrate deep into the MTS. We chose day 6 after incubation (Figure 19) due to it best mimicking *in vivo* tumors in the early linear growth region. At that size, the MTS is denser and starts forming a necrotic core, which is necessary to effectively model our assessments as GNR penetration and photothermal therapy in an *in vivo* colon cancer tumor (*130*). The plateau region has no net growth and, thus, is not a good representation of *in vivo* tumors.

4.5.2 Gold Nanorod Penetration in Multicellular Tumor Spheroids

After determining the optimal day for experimentation, we performed penetration experiments to understand the GNR uptake kinetics in 3D cell structures. As shown from Figure 18, GNRs were synthesized to be utilized for the imaging and photothermal therapy of MTS. The NIR SPR plasmon peak was exploited for luminescence imaging with TPM. We chose two methods for GNR delivery in the MTS to create different distributions for comparison purposes. The GNRs incubated for 24 hours mimicked the *in vivo* circumstances by allowing the GNRs to penetrate into the MTS from the outside.

This technique is similar to GNR intravenous injections because the GNRs would flow through the blood vessels and due to the EPR phenomenon would extravasate and penetrate into the tumor. *In vivo* studies have shown that gold nanoparticles, in the tumor, seem mostly be located around the blood vessels, not penetrating much further (*92, 93*). We found a similar limited penetration in the GNR distribution as shown in Figure 21 and Figure 22, with the GNRs only found in the outer ring, approximately ~20% of the radius into the MTS. As discussed previously, there are three growth regions within the MTS: (1) the outer proliferating area (~15% radially), (2) the middle quiescent area (~15-60% radially), and (3) the necrotic core (60-100% radially) (*159*). Thus, the 24 hour incubated GNRs are only found in the outer proliferating region. This indicates that since it is less dense and continuously growing, GNRs can transport through that region, however, the GNRs seem to be unable to penetrate through to the higher density quiescent region.

The other GNR delivery technique involved co-incubating the MTS with the GNRs. The GNRs were incubated simultaneously with the cells into the well at the same initial concentration as the 24 hour incubated GNRs. On the 6^{th} day of growth, with TPM, we found that the GNR distribution was significantly different than the 24 hour incubated GNRs (Figure 21 and Figure 22). The GNRs were distributed almost uniformly throughout the MTS with a slightly larger density in the outer ring. The GNRs are distributed throughout because the MTS appears to have grown around the GNRs and as the MTS grew larger the GNRs moved further outwards as well to the less dense MTS areas with some caught in the ECM. This ideal distribution is the current goal of all drug delivery studies but has not been able to be achieved in practice using oral or intravenous delivery. Even though this distribution is not relevant for comparing to *in vivo* results, we

believe it is important to study to show the photothermal therapeutic effects with the ideal situation of GNRs being distributed throughout the MTS.

4.5.3 Gold Nanorod Localization in Multicellular Tumor Spheroids

Using a higher magnification objective, we probed the GNR localization on the cellular level. As discussed in the GNR synthesis section, CTAB is present on the GNR surface. CTAB is a cationic surfactant, which allows for strong attraction to negatively-charged cells as well as internalization due to the lipophilic cell membrane. As discussed in the earlier *in vitro* 2D monolayer experiments, the CTAB encourages cell internalization and possibly organelle localization within the cell. In 3D cell structures the positive GNR surface charge does not allow for deep MTS penetration due to the cell and ECM negative charge (*165*). However, due to the stacked and dense cell structure in the MTS, the cellular GNR localization is not a trivial process. Figure 23 shows the co-incubated and 24 hour incubated GNRs within the center and periphery of the MTS, respectively. The co-incubated GNRs appear to be more aggregated but spread out through the MTS. However, possibly due to this aggregation and resulting size increase as well as the ECM negative charge, the GNRs were primarily shown to be in the ECM between the cells. Yet, some GNRs succeeded in cellular internalization as shown in Figure 23B. For the 24 hour incubated GNRs, the distribution between extracellularly and intracellularly located GNRs seems closer to even. Possibly due to the incubation time and limited GNR aggregation, we demonstrate the 24 hour incubated GNRs were able to internalize at a higher rate in the cells than the co-incubated GNRs.

4.5.4 Gold Nanorod-Mediated Photothermal Therapy of Multicellular Tumor Spheroids

After determining the GNR penetration and uptake in the MTS, we performed photothermal therapy to destroy the MTS by inducing cell death. In our first experiments, we visually inspected the MTS structural integrity to determine whether cell death occurred (Figure 24). It is clearly seen that the MTS at 40 W/cm^2 laser fluence rate lost all integrity and the cells were dislodged from the MTS and likely dead. However, such a qualitative method of utilizing bright-field imaging to examine structural integrity did not show any differences between the two GNR delivery methods.

4.5.5 Quantitative Analysis of Cell Death Pathways

To better understand the differences and the cell death pathway response to GNR-mediated photothermal therapy we performed a quantitative assessment using a cell death pathway stain and flow cytometry. After determining the effective regions of live, necrotic and apoptotic cells by utilizing the relative stain intensity amounts detected (Figure 25), we analyzed 4 replicates of each MTS sample with the two GNR delivery methods and a range of fluence rates. In Figure 26, we observe that the 24 hour incubated GNRs have a large increase in necrotic cell death, from ~29% to 46%, at a lower fluence rate (35 W/cm^2) than co-incubated GNRs (40 W/cm^2) has the first large increase in necrotic cell death, from ~29% to ~49% (Figure 26). This increase in necrotic cell death indicates the induction of significant cell death by photothermal therapy; as a result, we refer to this fluence rate as the necrotic threshold. We believe this threshold value is lower for the 24 hour incubated GNRs due to the limited GNR distribution. Since the GNRs are all within the outer region there could be a significant coupling effect increasing the GNR absorption efficiency, thus, increasing the amount of thermal energy delivered to the surroundings. Due to this increase in heat more cells were killed for the

24 hour incubated GNRs than the co-incubated GNRs at the same fluence rate (35 W/cm^2). However, as the fluence rates increased, the necrotic cell percentages were similar at 40 W/cm^2 for both delivery methods and actually higher for the co-incubated GNRs at 45 and 50 W/cm^2 (Figure 26C). We believe that the co-incubated GNRs induce more cell death after the respective necrotic threshold because of the more uniform distribution. Due to the GNRs being spread throughout the MTS, the localized thermal energy released from the GNRs can affect a greater number of cells.

Apoptotic cell death followed a different trend (Figure 26D). The apoptotic cell death percentages increased to a maximum at a certain fluence rate, which was observed to be same as the necrotic threshold, and decreased after that fluence rate. We believe that apoptosis follows this trend because it can be commenced at lower temperatures than necrosis due to the initiation process and intracellular signaling that occurs during apoptosis. In necrosis, the primary method of inducing cell death is through heating to cause sufficient membrane lysis; however, with apoptosis the lower heating could still induce protein denaturation and mitochondrial or nuclear disruption, thus initiating the apoptotic pathway. Thus, as the fluence rate is increased and the thermal energy being delivered increases, necrosis appears to become the dominant cell death pathway since almost all cells are dying through membrane lysis. For the 24 hour incubated GNRs, the fluence rate at which we see the maximum apoptosis (~13% at 35 W/cm^2) is lower than for the co-incubated GNRs (16% at 40 W/cm^2). The reasoning behind this, we believe, is similar to the necrotic threshold difference, which is the tightly localized area of the 24 hour incubated GNRs induces slightly higher heating due to a possible coupling effect reaching the temperature needed to induce apoptosis at a lower fluence rate than co-incubated GNRs. Conversely, the maximum apoptosis percentages for the co-incubated GNRs was detected to be higher than the 24 hour incubated GNRs, which we again

believe is because of the more uniform GNR distribution with the co-incubated GNRs delivering thermal energy to more cells. As the fluence rate increased the maximum necrotic percentages reached values of ~62% and ~75% for 24 hour incubation and co-incubated respectively, which were ~2.9 and ~3.5 times the control necrosis values. The absolute maximum apoptosis percentages, on the other hand, were much smaller in comparison to the absolute maximum necrotic percentages. However, the percentages were determined to be ~3.8 and ~4.6, respectively, times the control apoptosis percentages. Therefore, with respect to the control, apoptosis is determined to be increased at a higher rate than necrosis in MTS exposed to photothermal therapy utilizing both GNR delivery techniques.

Chapter 5: Conclusions

5.1 2D Monolayer Photothermal Therapy

In this study, we successfully targeted GNRs to different cell regions based on incubation time due to the time-dependent internalization process. Using TPM, we observed that GNRs were membrane-bound at 1.5 hours incubation time, starting to be internalized in lysosomal compartments at the 6 hour time point, and localized to organelles, hypothesized to be in the perinuclear space, at the 24 hour time point. At each time point, we performed photothermal therapy on colon cancer cells incubated with GNRs to quantitatively determine the cell death response to highly localized GNR heating using flow cytometry. We found that the 1.5 hour time point required the highest fluence rate to induce necrosis and apoptosis while the 24 hour time point needed the lowest fluence rate for both. In addition, photothermal therapy at the 24 time point, comprised of internalized GNRs localized to organelles in the perinuclear space, resulted in the highest apoptotic percentage (~18.5%) while the 6 hour time point (~13%) and 1.5 hour time points (9.2%) were less. Furthermore, the 24 hour and 6 hour time points had similar apoptosis values as other anti-cancer therapeutics. In conclusion, we believe this data indicates that the cell death pathway response to photothermal therapy is influenced by GNR localization, which we can utilize to optimize the process of photothermal therapy.

5.2 3D Multicellular Tumor Spheroid Photothermal Therapy

In this portion of the study, we quantitatively analyzed the cell death pathway response to the GNR-mediated photothermal therapy in 3D cell cultures. The MCTS was shown to be an effective *in vitro* tumor model to understand how photothermal therapy affects the cell death pathways *in vivo*. Using two GNR delivery methods, we were able

to confirm two different distributions with TPM: (1) 24 hour incubated GNRs localized around the MTS periphery similar to *in vivo* studies and (2) co-incubated GNRs found spread almost uniformly throughout the MTS. With these two distributions, we explored the cellular response to photothermal therapy by measuring the apoptosis and necrosis values quantitatively with flow cytometry. We found that the using photothermal therapy we were able to induce necrosis and apoptosis at different fluence rates. As demonstrated there was a lower threshold for cell death, both apoptosis and necrosis, for the 24 hour incubated GNRs due to the tighter GNR distribution within the outer MTS ring leading to a possible coupling effect, enhancing GNR absorption. Conversely, the co-incubated GNRs had a higher maximum apoptotic and necrotic percentage values than the 24 hour incubated GNRs due to the uniform distribution allowing for more cells to be exposed to the thermal energy delivered from the GNRs. Through a quantitative assessment of the cell death response to photothermal therapy we gain a better understanding of the affect localized heating has on tumors. In conclusion, the fluence rates, 35 and 40 W/cm^2 for 24 hour incubated and co-incubated GNRs, respectively, at which apoptosis is at a maximum is preferable for the optimization of GNR-mediated photothermal therapy.

5.3 Comparison of Cell Death Response in 2D and 3D to Relevant Work

Several studies have examined the effect of thermal therapy on cell death, specifically comparing the cell death pathway response to temperature. Thermal therapy, essentially, involves the bulk heating of tumor tissue using radio frequency or microwave radiation (*166*). As discussed in Chapter 1, the heating is not localized solely to the tumor and the temperature will be elevated in surrounding tissues as well leading to collateral damage. With thermal therapy, the temperature is elevated slightly above physiological levels, 43-50°C, for long time durations, 0.5-8 hours, to induce the cytotoxic response

(*167*). The temperature needs to be in that range due to the lack of localization and possible collateral damage, which is the reasoning for using GNR-mediated photothermal therapy with more selective heating. To measure temperature in our earlier studies, an IR camera was used. However, IR measurements only allow us to probe surface (~100 μm) averaged heating due to the lateral resolution and interference due to strong infrared absorption by water. In our later studies, we did not measure temperature during heating due to the difficulty of determining the temperature on the nanoscale and getting an accurate measurement of the MTS in depth. Therefore, a comparison with relevant previous results in thermal therapy using bulk heating may allow for some speculation on elevated temperatures achieved during GNR-mediated photothermal therapy.

One study performed whole body hyperthermia, 41.5°C for 2 hours, on mice with colon cancer and fibrosarcoma tumors (*168*). Cell death quantification was performed by histopathology on the tumor samples and grading apoptosis as 'none', 'modest', 'mild', 'moderate' and 'severe' using cell morphology. The authors found that apoptosis increased and reached a maxima of ~43% apoptotic cell death 8 hours after hyperthermic treatment and the fibrosarcoma reached ~19% apoptotic cell death 4 hours after hyperthermia.

Another study performed thermal therapy on *ex vivo* tumor slices (AT-1 Dunning prostate tumors) at several different temperatures and times (*169*). The authors also quantified apoptosis as 'none', 'mild', 'moderate' and 'marked' using histopathology visually inspecting the cell morphology, and karyorrhexic nuclear debris. The number of tissues that exhibited 'moderate' and 'marked' apoptosis was reported as a percentage of total tissues graded at 3, 24 and 72 hours after treatment. The treatments varied from 40°C for 15 minutes to 70°C for 1 minute. The authors found that only at 40°C for 15 minutes was there any significant degree of apoptosis characterized as 'moderate' or

‘marked’, however, it was not significant from the control. Furthermore, the authors established that apoptosis measurements were time-dependent and that at 24 and 72 hours after treatment apoptosis values were significantly higher than at the 3 hour time point.

At higher temperatures (and shorter time durations), the authors observed no significant apoptosis, but still saw significant cell death, suggesting that it reached a threshold at which necrosis was the dominant cell death pathway. This finding is similar to our result that there is a threshold, either temperature or laser fluence rate (which are related), at which apoptosis decreases and necrosis becomes the primary method of cell death. Another study confirmed this same result finding moderate apoptotic values with treatment ranging from 42-45°C for 30 minutes, but above 45°C all cell death was through necrosis (*170*). In fact, this study showed that the apoptotic cell death percentages increased with as the temperature increased from 42 to 44°C (at which we see a maxima of ~55% apoptosis) and decreases as necrosis becomes the dominant cell death pathway, very similar to our findings.

From the same group as the previous study, the authors performed thermal therapy at 43°C and 45°C for 30 minutes heating duration (*171*). Then they quantified apoptosis by histopathology similar as the other studies using morphology at 4, 6 and 8 hours after treatment. In murine cancer cells, the authors measured from 1-20% apoptosis 4 hours after 43°C treatment and 10-25% apoptosis (and one at 53%) after 45°C treatment. With most human cancer cells (carcinoma and melanoma), which is more relevant for our work, the authors observed ~ 20% apoptosis 6-8 hours after 43°C treatment. However, two types of Burkitt’s lymphoma (BM 13674 and WW2) had 95% and 97% apoptosis 8 and 6 hours, respectively, after 43°C treatment.

Based on these results, we notice that the induction of cell death pathways directly depends on the cancer cell type, thus, making comparisons between different cell types is

difficult. In addition, all of these studies utilized bulk heating over long time durations at low temperatures, due to the non-specificity, which increases the difficulty in comparison. Furthermore, the quantitative measurements to determine apoptosis are dramatically different from our study and these older studies. In their study, the quantification was performed through histopathology, which is the gold standard, but is still subjective and only can look at a smaller sample size. Whereas, in our study, we performed flow cytometry, which still has some subjectivity in terms of determining the apoptotic region, but incorporates the whole sample. However, we can infer that our results with ~18% maximum apoptosis in monolayers and 16% maximum apoptosis in MTS are similar to some of the percentages seen in thermal therapy studies. For the first study explored, the authors inspected ~19% apoptosis in fibrosarcoma after 41.5°C for 2 hours with whole body hyperthermia. In the other studies, the authors observed ~20% apoptosis after 43°C for 30 minutes in tissue slices and *in vitro* with their cancer cell types. As a result, we can speculate that in our studies when we achieved ~16-18% apoptosis, the temperatures inside the cells and MTS, respectively, were equivalent to 43°C bulk heating for 30 minutes. However, to better understand the relationship between cell death pathways and heating during GNR-mediated photothermal therapy, future studies need to be performed in which temperature is accurately measured, possibly using magnetic resonance thermography, or GNR heating modeled, which has not been performed effectively yet.

5.4 Comparison between Cell Death Response for 2D and 3D Cell Culture

With quantitative results for cell death pathway response to 2D monolayer and 3D MCTS to GNR-mediated photothermal therapy, we can compare the trends. Figure 27 shows the % necrotic or apoptotic cell death normalized by their respective negative

control, % necrotic or apoptotic cell death. The overall trends are the same for both 2D and 3D cell culture. The necrotic cell death percentage increases with increasing fluence rate for both the monolayer and MTS. In addition for both cell culture types, the apoptotic cell death percentage increased to a maximum and then decreased back down as the fluence rate increased.

If we compare the necrotic percentages normalized with their respective controls between the two cell culture types, it is clear that there is a significantly higher amount of necrosis in 2D cell culture (up to $18x$ for 24 hour GNR incubation) than MTS (up to $3.5x$ for co-incubated GNRs and 24 hour GNR incubation). Although, the initial necrotic cell death percentages for the control are very different between the 2D (~4.6%) and the 3D (~21.3%) due to the necrotic core in the MTS, which creates difficultly in comparing the response to the two different cell culture types. Yet in this case, there is significantly more absolute necrotic cell death in the 2D cell culture (~87%) for the 24 hour incubated GNRs than the MTS with either the co-incubated (~74%) or 24 hour incubated GNRs (62%) ($p < 0.01$).

The absolute apoptotic cell death percentages follow a similar trend. The MTS cell culture had a significantly lower absolute apoptotic percentage (maximum of ~16% for co-incubated GNRs) than the 2D monolayer (maximum of ~18% for 24 hour incubated GNRs) ($p < 0.05$). However, the percentages normalized to the control illustrate an opposite result. In Figure 27, we observe that the monolayer 24 hour incubated GNRs ($2.9x$) has a lower normalized value than either the 3D MTS co-incubated ($4.6x$) and 24 hour incubated GNRs ($3.8x$). Similar to the normalized necrotic cell death difference, this disparity is due primarily to the apoptotic control percentages for 2D monolayer (~6.3%) and 3D MTS (3.5%).

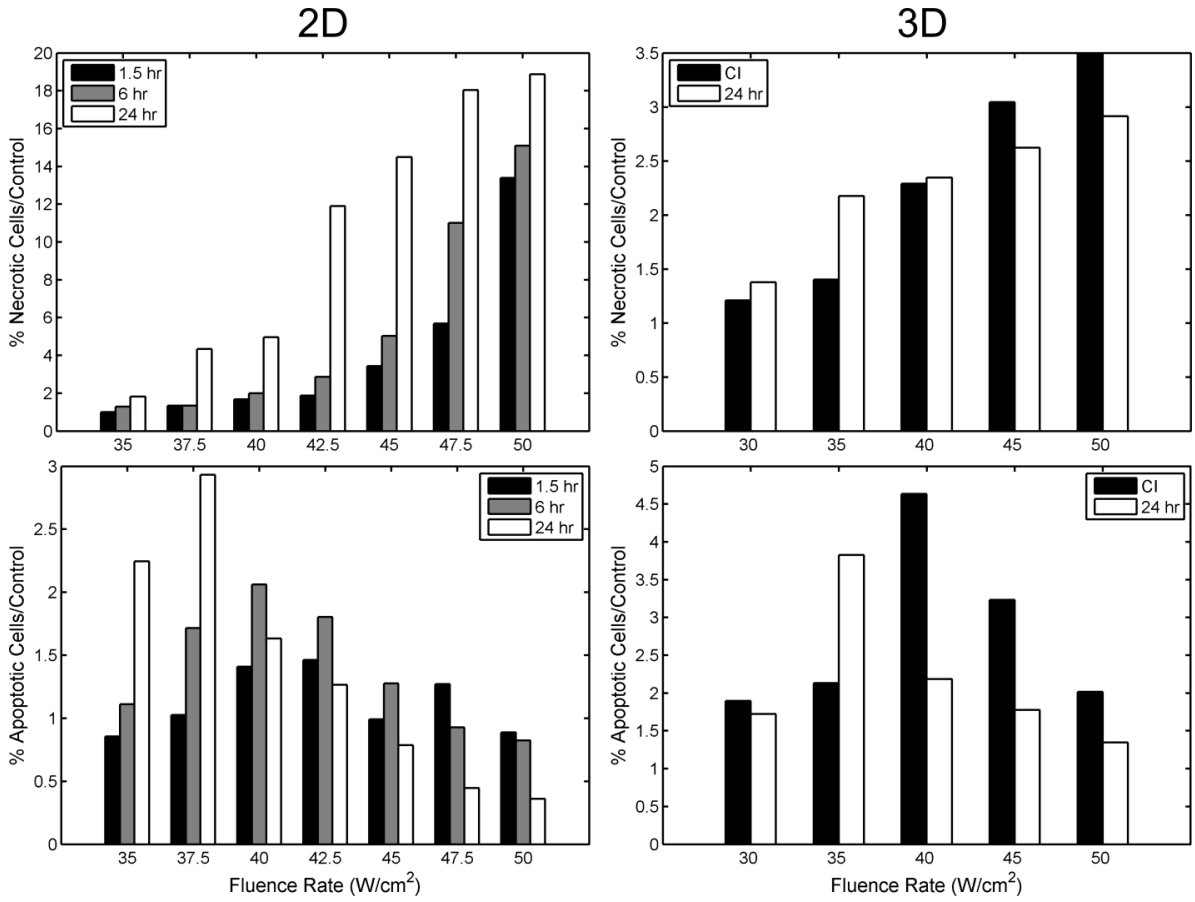

Figure 27: Comparison between apoptotic and necrotic cell percentages for 2D and 3D cell cultures. In this figure, all of the values in the plots are normalized by their respective controls to better allow comparisons between the 2D and 3D necrotic and apoptotic values. 2D has a larger normalized necrotic value than 3D but a lower normalized apoptotic value than 2D.

Therefore, we notice that overall 3D cell culture has significantly less cell death, both apoptotic and necrotic, than the 2D monolayer for similar fluence rates and GNR incubation times, which is similar to what other studies have observed (*158, 172*). We believe this can primarily be attributed to GNR distribution and localization. For the 2D monolayer study, the GNRs are distributed throughout the monolayer and are most likely internalized in the perinuclear region of every cell for the 24 hour incubated GNRs. Whereas, in the 3D MTS, with the 24 hour incubated GNRs we determined that the

GNRs were only located in the outer ring (~20% of the radius) and with the co-incubated GNRs, even though the GNRs are distributed more evenly than the 24 hour incubated GNRs, it is still not feasible for GNRs to be beside or within every cell in the MTS. Furthermore, the tumor mimicking morphology, including the cell-cell and cell-ECM interactions found in the 3D MTS cell culture could prevent apoptotic and necrotic cell death from occurring. We believe that these interactions reduce toxicity in MTS not only because of the ECM formation mechanically resisting GNR penetration, but also possibly due to the inherent enhanced cellular function and repair ability in 3D cell structures allowing the cells to have a higher threshold for injury.

5.5 FUTURE WORK

All of this work completed in this dissertation was on the cellular level, understanding the mechanisms of cell death response to photothermal therapy based on the pathways involved, necrosis or apoptosis. Yet, as discussed in Chapter 1, there are other possible programmed cell death pathways that could be involved, such as pyroptosis and necroptosis. Therefore, in continuing studies, it would be of great importance to further differentiate the quantification of cell death pathways into all the possibilities. With the current fluorescent stains used in this study, we would be unable to differentiate between necrosis, pyroptosis and necroptosis because all involve cell lysis, which is how the PI stain internalizes into the cell. To understand the process, we could perform a time-dependent study to inspect when PI enters the cell since necrosis should be instantaneous during cell injury, pyroptosis is known to be rapid, and necroptosis should be on the same time scales as apoptosis. A better differentiation would involve utilizing potential biomarkers, such as necrostatins for necroptosis, for each cell death type, which would need to be explored more extensively (*111*).

Furthermore, in future work, it would be extremely valuable to understand the processes, now that we confirmed differences based on GNR localization, on the molecular level. This includes gaining a better understanding of the effect of heating on the protein structures and probing macromolecular transitions and caspase activation with regards to apoptotic cell death. As discussed in the introduction, both initiator and executioner caspases are vital in the initiation and continuation of the apoptotic pathway. Therefore, probing the caspase activity will provide a better indication of the apoptotic processes occurring, especially if, as is usually the case with cancer, the apoptotic pathway is suppressed either upstream or downstream of the caspase activation. Therefore, to get an accurate understanding of the processes occurring on the molecular level, we would need to probe the apoptotic pathway at several different levels to determine where the suppression was located.

If any three of the primary macromolecules (nucleic acid inactivation, protein denaturation, and lipid transitions) undergo significant transitions, cell death can be initiated in the form of apoptosis or necrosis. Nucleic acids (DNA/RNA) encode, transmit and express all cellular genetic material and protein synthesis. The inactivation transition of nucleic acids through heat is known to occur at ~85-90°C, which is significantly higher than the hyperthermic regime. Studies have shown that it is not possible to affect DNA/RNA directly using solely hyperthermic heat shock (*173*). The boundary membranes for all significant intracellular organelles as well as the outer membrane of the cell are composed of lipids, mediating intracellular homeostasis by trafficking membrane transport. Lipids have not been shown to melt, transitioning from a solid to a liquid, at temperatures greater than 37°C (during heat shock), which would remove the barrier to intracellular transport (*174, 175*). Studies have shown that hyperthermic heat shock affects the lipid membranes slightly, resulting in changes in the

intracellular concentrations of certain ions (Ca^{2+} for example); however, it has been shown that this does not adversely affect cell survival (*176-178*). Proteins perform all basic functions in the cell, strongly utilized in the signal transduction and cell death pathways. The denaturation transition of proteins has similar activation energies to cell death caused by thermal therapy (*6, 179*). Differential scanning calorimetry (DSC) studies performed on cells show that significant transitions occur in the hyperthermic regime (>43°C), which were shown to be intracellular protein denaturation (*180*). Utilizing ethanol, which sensitizes proteins to denaturation, and glycerol, which protects proteins from denaturation, elicited expected results for those transitions, further suggesting that the transition is protein denaturation.

Furthermore, we could also look at the response to photothermal therapy in terms of heat shock and cellular resilience and repair function. Inactivation is not the only result of thermal therapy, some protein pathways are activated due to heat shock. Cells can develop thermotolerance through the activation of the heat shock proteins (HSP). When cells are exposed to high temperatures for short time periods or lower temperatures for long durations, HSP synthesis is instigated. There are many different forms of HSPs based on their size (kDa), from small (<40 kDa), to HSP60, HSP70, HSP90 and HSP100 families. Many of these HSPs function as protein chaperones and prevent apoptosis due to any forms of stress, including heat (*181, 182*).

HSPs protect newly formed proteins and older, denatured proteins by preventing aggregation that would result in loss of function, allowing enough time for the protein to refold properly (*183*). Furthermore, many HSPs inhibit molecules that that are integral to the apoptotic pathway. For example, HSP27 inhibits cytochrome C, whereas HSP70 and HSP90 inhibit the formation of the apoptosome and intervene in the caspase pathway. Nevertheless, when cells are exposed to higher temperatures at sufficient durations HSPs

cannot be synthesized to prevent apoptosis. Relevant to this study, HSP formation can be used as an indicator of protein denaturation as well as the initiation of the apoptotic cascade. Studies have analyzed HSP activation as a method to evaluate the cell reaction to thermal therapy (*184*).

In addition, we can explore other parameters to gain a better understanding, such as the length of laser irradiation time. Essentially, we would try to determine if we reduce the fluence rate and increased the exposure time, would the apoptotic pathway (or specific macromolecular transitions) be initiated more significantly. Ideally, these modifications could be tested with a finite element model based on the heat equation and a system of state equations describing the different possible cellular responses (*185*).

5.6 Final Conclusions

Overall in this study we observed and quantified the cell death pathway response to GNR-mediated photothermal therapy in 2D and 3D cell structures. Therefore, we have indicated that threshold for cell death and, more specifically, the cell death pathways initiated are affected by GNR localization on the cellular level in 2D. Furthermore, with the 3D cell structure we found that GNR distribution made a significant difference in cell death pathway response. We also determined that there is less overall cell death, both apoptotic and necrotic, due to photothermal therapy in the 3D MTS than in the 2D monolayer study. Consequently, we believe these differences between cell death pathway response to GNR-mediated photothermal therapy in 2D and 3D cell culture lends credence to the belief that a 3D in vitro tumor structure, like MTS, are necessary to accurately model the findings that would be seen in an in vivo tumor. We believe using 3D MTS provides significant benefits over 2D monolayer studies for toxicity calculations, such as GNR-mediated photothermal therapy. In conclusion, we believe that

these MTS allow for accurate assessments of the GNR penetration and distribution through an ECM and densely packed cell structure as well as providing a better evaluation of the cell death pathway response to cancer therapeutics, such as photothermal therapy, due to cell-cell and cell-ECM interactions augmenting the cellular resilience through increased cell repair function. Through the cell death pathway response quantification for gold nanoparticle-mediated photothermal therapy we gain a better understanding to optimize and improve cancer therapy.

References

1. R. Siegel, D. Naishadham, A. Jemal, Cancer statistics, 2013. *CA: a cancer journal for clinicians* **63**, 11-30 (2013).
2. N. Howlader, A. Noone, M. Krapcho, N. Neyman, R. Aminou, S. Altekruse, C. Kosary, J. Ruhl, Z. Tatalovich, H. Cho, SEER cancer statistics review, 1975–2009 (vintage 2009 populations). *Bethesda, MD: National Cancer Institute*, (2012).
3. A. K. Frei III E, in *Cancer Medicine,* B. e. al, Ed. (BCDecker, Hamilton, Ontario, 2000), chap. 40.
4. R. J. Mundt A, Weichselbaum R, in *Cancer Medicine,* B. e. al, Ed. (BCDecker, Hamilton, Ontario, 2000), chap. 34.
5. M. D. Pollock R, in *Cancer Medicine,* B. e. al, Ed. (BCDecker, Hamilton, Ontario, 2000), chap. 32.
6. J. R. Lepock, Cellular effects of hyperthermia: relevance to the minimum dose for thermal damage. *Int. J. Hyperthermia* **19**, 252-266 (2003); published online EpubMay-June 2003 (
7. A. Laszlo, The effects of hyperthermia on mammalian cell structure and function. *Cell Prolif.* **25**, 59-87 (1992).
8. B. B. V, Thermal potentiation of mammalian cell killing: Clues for understanding and potential for tumor therapy. *Adv. Radiat. Biol.* **6**, 267-324 (1976).
9. K. J. Henle, L. A. Dethlefsen, HEAT FRACTIONATION AND THERMOTOLERANCE - REVIEW. *Cancer Research* **38**, 1843-1851 (1978).
10. J. R. Cole, N. A. Mirin, M. W. Knight, G. P. Goodrich, N. J. Halas, Photothermal efficiencies of nanoshells and nanorods for clinical therapeutic applications. *The Journal of Physical Chemistry C* **113**, 12090-12094 (2009).
11. H. Chen, L. Shao, T. Ming, Z. Sun, C. Zhao, B. Yang, J. Wang, Understanding the photothermal conversion efficiency of gold nanocrystals. *Small* **6**, 2272-2280 (2010); published online EpubOct 18 (10.1002/smll.201001109).
12. D. K. Roper, W. Ahn, M. Hoepfner, Microscale heat transfer transduced by surface plasmon resonant gold nanoparticles. *Journal of Physical Chemistry C* **111**, 3636-3641 (2007)10.1021/jp064341w).
13. L. R. Hirsch, R. J. Stafford, J. A. Bankson, S. R. Sershen, B. Rivera, R. E. Price, J. D. Hazle, N. J. Halas, J. L. West, Nanoshell-mediated near-infrared thermal therapy of tumors under magnetic resonance guidance. *Proc Natl Acad Sci U S A* **100**, 13549-13554 (2003); published online EpubNov 11 (10.1073/pnas.2232479100).

14. X. H. Huang, I. H. El-Sayed, W. Qian, M. A. El-Sayed, Cancer cell imaging and photothermal therapy in the near-infrared region by using gold nanorods. *Journal of the American Chemical Society* **128**, 2115-2120 (2006)10.1021/ja057254a).

15. C. M. Pitsillides, E. K. Joe, X. B. Wei, R. R. Anderson, C. P. Lin, Selective cell targeting with light-absorbing microparticles and nanoparticles. *Biophysical Journal* **84**, 4023-4032 (2003).

16. V. P. Zharov, E. Galitovskaya, M. Viegas, Photothermal guidance for selective photothermolysis with nanoparticles. *Laser Interaction with Tissue and Cells Xv* **5319**, 291-300 (2004)10.1117/12.532011).

17. G. Mie, Considerations on the optics of turbid media, especially colloidal metal sols. *Ann. d. Physik* **25**, 377-442 (1908).

18. C. F. Bohren, D. R. Huffman, Absorption and scattering of light by small particles. *Research supported by the University of Arizona and Institute of Occupational and Environmental Health. New York, Wiley-Interscience, 1983, 541 p.* **1**, (1983).

19. U. Kreibig, M. Vollmer, Optical properties of metal clusters. (1995).

20. M. A. El-Sayed, Some interesting properties of metals confined in time and nanometer space of different shapes. *Accounts of Chemical Research* **34**, 257-264 (2001).

21. S. Link, M. A. El-Sayed, Shape and size dependence of radiative, non-radiative and photothermal properties of gold nanocrystals. *International Reviews in Physical Chemistry* **19**, 409-454 (2000).

22. P. K. Jain, K. S. Lee, I. H. El-Sayed, M. A. El-Sayed, Calculated absorption and scattering properties of gold nanoparticles of different size, shape, and composition: Applications in biological imaging and biomedicine. *Journal of Physical Chemistry B* **110**, 7238-7248 (2006)10.1021/jp057170o).

23. K. L. Kelly, E. Coronado, L. L. Zhao, G. C. Schatz, The optical properties of metal nanoparticles: the influence of size, shape, and dielectric environment. *The Journal of Physical Chemistry B* **107**, 668-677 (2003).

24. W. Rechberger, A. Hohenau, A. Leitner, J. Krenn, B. Lamprecht, F. Aussenegg, Optical properties of two interacting gold nanoparticles. *Optics Communications* **220**, 137-141 (2003).

25. K. H. Su, Q. H. Wei, X. Zhang, J. Mock, D. Smith, S. Schultz, Interparticle coupling effects on plasmon resonances of nanogold particles. *Nano Letters* **3**, 1087-1090 (2003).

26. P. K. Jain, S. Eustis, M. A. El-Sayed, Plasmon coupling in nanorod assemblies: optical absorption, discrete dipole approximation simulation, and exciton-coupling model. *The Journal of Physical Chemistry B* **110**, 18243-18253 (2006).

27. S. Underwood, P. Mulvaney, Effect of the solution refractive index on the color of gold colloids. *Langmuir* **10**, 3427-3430 (1994).

28. S. K. Ghosh, S. Nath, S. Kundu, K. Esumi, T. Pal, Solvent and ligand effects on the localized surface plasmon resonance (LSPR) of gold colloids. *The Journal of Physical Chemistry B* **108**, 13963-13971 (2004).

29. M. S. Patterson, B. Chance, B. C. Wilson, Time resolved reflectance and transmittance for the non-invasive measurement of tissue optical properties. *Applied Optics* **28**, 2331-2336 (1989).

30. E. M. Purcell, C. R. Pennypacker, Scattering and absorption of light by nonspherical dielectric grains. *The Astrophysical Journal* **186**, 705-714 (1973).

31. B. T. Draine, P. J. Flatau, DISCRETE-DIPOLE APPROXIMATION FOR SCATTERING CALCULATIONS. *Journal of the Optical Society of America a-Optics Image Science and Vision* **11**, 1491-1499 (1994).

32. B. T. Draine, P. J. Flatau, User Guide for the Discrete Dipole Approximation Code DDSCAT 7.1. *arXiv:1002.1505*, (2010).

33. N. Felidj, J. Aubard, G. Levi, Discrete dipole approximation for ultraviolet-visible extinction spectra simulation of silver and gold colloids. *Journal of Chemical Physics* **111**, 1195-1208 (1999).

34. K. S. Lee, M. A. El-Sayed, Dependence of the enhanced optical scattering efficiency relative to that of absorption for gold metal nanorods on aspect ratio, size, end-cap shape, and medium refractive index. *Journal of Physical Chemistry B* **109**, 20331-20338 (2005)10.1021/jp054385p).

35. A. Brioude, X. Jiang, M. Pileni, Optical properties of gold nanorods: DDA simulations supported by experiments. *The Journal of Physical Chemistry B* **109**, 13138-13142 (2005).

36. S. W. Prescott, P. Mulvaney, Gold nanorod extinction spectra. *Journal of Applied Physics* **99**, 123504-123504-123507 (2006).

37. C. Ungureanu, R. G. Rayavarapu, S. Manohar, T. G. van Leeuwen, Discrete dipole approximation simulations of gold nanorod optical properties: Choice of input parameters and comparison with experiment. *Journal of Applied Physics* **105**, (2009)10.1063/1.3116139).

38. N. Khlebtsov, L. Trachuk, A. Mel'nikov, The effect of the size, shape, and structure of metal nanoparticles on the dependence of their optical properties on the refractive index of a disperse medium. *Optics and spectroscopy* **98**, 77-83 (2005).

39. L. V. Wang, H. Wu, *Biomedical optics: principles and imaging*. (Wiley-Blackwell, 2007).

40. R. D. Averitt, S. L. Westcott, N. J. Halas, Linear optical properties of gold nanoshells. *JOSA B* **16**, 1824-1832 (1999).

41. S. Oldenburg, R. Averitt, S. Westcott, N. Halas, Nanoengineering of optical resonances. *Chemical Physics Letters* **288**, 243-247 (1998).

42. S. J. Oldenburg, J. B. Jackson, S. L. Westcott, N. Halas, Infrared extinction properties of gold nanoshells. *Applied Physics Letters* **75**, 2897 (1999).

43. W. Lu, C. Y. Xiong, G. D. Zhang, Q. Huang, R. Zhang, J. Z. Zhang, C. Li, Targeted Photothermal Ablation of Murine Melanomas with Melanocyte-Stimulating Hormone Analog-Conjugated Hollow Gold Nanospheres. *Clinical Cancer Research* **15**, 876-886 (2009)10.1158/1078-0432.ccr-08-1480).

44. M. P. Melancon, W. Lu, Z. Yang, R. Zhang, Z. Cheng, A. M. Elliot, J. Stafford, T. Olson, J. Z. Zhang, C. Li, In vitro and in vivo targeting of hollow gold nanoshells directed at epidermal growth factor receptor for photothermal ablation therapy. *Molecular Cancer Therapeutics* **7**, 1730-1739 (2008); published online EpubJun (10.1158/1535-7163.mct-08-0016).

45. Y. Y. Yu, S. S. Chang, C. L. Lee, C. R. C. Wang, Gold nanorods: electrochemical synthesis and optical properties. *The Journal of Physical Chemistry B* **101**, 6661-6664 (1997).

46. E. S. Kooij, B. Poelsema, Shape and size effects in the optical properties of metallic nanorods. *Phys. Chem. Chem. Phys.* **8**, 3349-3357 (2006).

47. A. Brioude, X. C. Jiang, M. P. Pileni, Optical properties of gold nanorods: DDA simulations supported by experiments. *Journal of Physical Chemistry B* **109**, 13138-13142 (2005).

48. S. Link, M. Mohamed, M. El-Sayed, Simulation of the optical absorption spectra of gold nanorods as a function of their aspect ratio and the effect of the medium dielectric constant. *The Journal of Physical Chemistry B* **103**, 3073-3077 (1999).

49. V. P. Pattani, J. W. Tunnell, Nanoparticle-mediated photothermal therapy: A comparative study of heating for different particle types. *Lasers in Surgery and Medicine* **44**, 675-684 (2012).

50. L. Messori, G. Marcon, in *Metal ions and their complexes in medication*. (Marcel Dekker Inc, 2004), vol. 41, pp. 279.

51. A. K. Iyer, G. Khaled, J. Fang, H. Maeda, Exploiting the enhanced permeability and retention effect for tumor targeting. *Drug Discovery Today* **11**, 812-818 (2006)10.1016/j.drudis.2006.07.005).

52. H. Maeda, The enhanced permeability and retention (EPR) effect in tumor vasculature: The key role of tumor-selective macromolecular drug targeting. *Advances in Enzyme Regulation, Vol 41* **41**, 189-207 (2001).

53. H. Maeda, J. Wu, T. Sawa, Y. Matsumura, K. Hori, Tumor vascular permeability and the EPR effect in macromolecular therapeutics: a review. *Journal of Controlled Release* **65**, 271-284 (2000).

54. H. Maeda, J. Fang, T. Inutsuka, Y. Kitamoto, Vascular permeability enhancement in solid tumor: various factors, mechanisms involved and its implications. *International Immunopharmacology* **3**, 319-328 (2003)10.1016/s1567-5769(02)00271-0).

55. L. Brannon-Peppas, J. O. Blanchette, Nanoparticle and targeted systems for cancer therapy. *Adv. Drug Deliv. Rev.* **56**, 1649-1659 (2004); published online EpubSep (10.1016/j.addr.2004.02.014).

56. S. Kumar, J. Aaron, K. Sokolov, Directional conjugation of antibodies to nanoparticles for synthesis of multiplexed optical contrast agents with both delivery and targeting moieties. *Nature Protocols* **3**, 314-320 (2008)10.1038/nprot.2008.1).

57. H. W. Liao, J. H. Hafner, Gold nanorod bioconjugates. *Chemistry of Materials* **17**, 4636-4641 (2005)10.1021/cm050935k).

58. A. Liopo, A. Conjusteau, D. Tsyboulski, B. Ermolinsky, A. Kazansky, A. Oraevsky, Biocompatible Gold Nanorod Conjugates for Preclinical Biomedical Research. *Journal of nanomedicine & nanotechnology* **S2**, (2012); published online EpubAug 3 (10.4172/2157-7439.S2-001).

59. Y. Akiyama, T. Mori, Y. Katayama, T. Niidome, The effects of PEG grafting level and injection dose on gold nanorod biodistribution in the tumor-bearing mice. *Journal of controlled release : official journal of the Controlled Release Society* **139**, 81-84 (2009); published online EpubOct 1 (10.1016/j.jconrel.2009.06.006).

60. Arnida, A. Malugin, H. Ghandehari, Cellular uptake and toxicity of gold nanoparticles in prostate cancer cells: a comparative study of rods and spheres. *Journal of applied toxicology : JAT* **30**, 212-217 (2010); published online EpubApr (10.1002/jat.1486).

61. T. Niidome, M. Yamagata, Y. Okamoto, Y. Akiyama, H. Takahashi, T. Kawano, Y. Katayama, Y. Niidome, PEG-modified gold nanorods with a stealth character for in vivo applications. *Journal of controlled release : official journal of the Controlled Release Society* **114**, 343-347 (2006); published online EpubSep 12 (10.1016/j.jconrel.2006.06.017).

62. A. M. Alkilany, C. J. Murphy, Toxicity and cellular uptake of gold nanoparticles: what we have learned so far? *Journal of nanoparticle research : an interdisciplinary forum for nanoscale science and technology* **12**, 2313-2333 (2010); published online EpubSep (10.1007/s11051-010-9911-8).

63. A. M. Alkilany, P. K. Nagaria, C. R. Hexel, T. J. Shaw, C. J. Murphy, M. D. Wyatt, Cellular uptake and cytotoxicity of gold nanorods: molecular origin of cytotoxicity and surface effects. *Small* **5**, 701-708 (2009); published online EpubMar (10.1002/smll.200801546).

64. E. E. Connor, J. Mwamuka, A. Gole, C. J. Murphy, M. D. Wyatt, Gold nanoparticles are taken up by human cells but do not cause acute cytotoxicity. *Small* **1**, 325-327 (2005); published online EpubMar (10.1002/smll.200400093).

65. N. Khlebtsov, L. Dykman, Biodistribution and toxicity of engineered gold nanoparticles: a review of in vitro and in vivo studies. *Chemical Society reviews* **40**, 1647-1671 (2011); published online EpubMar (10.1039/c0cs00018c).

66. R. G. Rayavarapu, W. Petersen, L. Hartsuiker, P. Chin, H. Janssen, F. W. van Leeuwen, C. Otto, S. Manohar, T. G. van Leeuwen, In vitro toxicity studies of polymer-coated gold nanorods. *Nanotechnology* **21**, 145101 (2010); published online EpubApr 9 (10.1088/0957-4484/21/14/145101).

67. S. C. Gad, K. L. Sharp, C. Montgomery, J. D. Payne, G. P. Goodrich, Evaluation of the toxicity of intravenous delivery of auroshell particles (gold-silica nanoshells). *International journal of toxicology* **31**, 584-594 (2012); published online EpubNov-Dec (10.1177/1091581812465969).

68. J. Y. Chen, D. L. Wang, J. F. Xi, L. Au, A. Siekkinen, A. Warsen, Z. Y. Li, H. Zhang, Y. N. Xia, X. D. Li, Immuno gold nanocages with tailored optical properties for targeted photothermal destruction of cancer cells. *Nano Letters* **7**, 1318-1322 (2007)10.1021/nl070345g).

69. I. H. El-Sayed, X. H. Huang, M. A. El-Sayed, Selective laser photo-thermal therapy of epithelial carcinoma using anti-EGFR antibody conjugated gold nanoparticles. *Cancer Letters* **239**, 129-135 (2006)10.1016/j.canlet.2005.07.035).

70. C. Loo, A. Lowery, N. Halas, J. West, R. Drezek, Immunotargeted nanoshells for integrated cancer imaging and therapy. *Nano Letters* **5**, 709-711 (2005)10.1021/nl050127s).

71. P. Puvanakrishnan, P. Diagaradjane, S. M. Kazmi, A. K. Dunn, S. Krishnan, J. W. Tunnell, Narrow band imaging of squamous cell carcinoma tumors using topically delivered anti-EGFR antibody conjugated gold nanorods. *Lasers Surg Med* **44**, 310-317 (2012); published online EpubApr (10.1002/lsm.22019).

72. L. Tong, Y. Zhao, T. B. Huff, M. N. Hansen, A. Wei, J. X. Cheng, Gold nanorods mediate tumor cell death by compromising membrane integrity. *Advanced Materials* **19**, 3136-+ (2007)10.1002/adma.200701974).

73. X. Huang, B. Kang, W. Qian, M. A. Mackey, P. C. Chen, A. K. Oyelere, I. H. El-Sayed, M. A. El-Sayed, Comparative study of photothermolysis of cancer cells with nuclear-targeted or cytoplasm-targeted gold nanospheres: continuous wave

or pulsed lasers. *Journal of biomedical optics* **15**, 058002 (2010); published online Epub2010 (10.1117/1.3486538).

74. A. K. Oyelere, P. C. Chen, X. Huang, I. H. El-Sayed, M. A. El-Sayed, Peptide-conjugated gold nanorods for nuclear targeting. *Bioconjugate Chem.* **18**, 1490-1497 (2007); published online EpubSep-Oct (10.1021/bc070132i).

75. N. J. Durr, T. Larson, D. K. Smith, B. A. Korgel, K. Sokolov, A. Ben-Yakar, Two-photon luminescence imaging of cancer cells using molecularly targeted gold nanorods. *Nano Letters* **7**, 941-945 (2007)10.1021/nl062962v).

76. X. H. Huang, P. K. Jain, I. H. El-Sayed, M. A. El-Sayed, Plasmonic photothermal therapy (PPTT) using gold nanoparticles. *Lasers in Medical Science* **23**, 217-228 (2008)10.1007/s10103-007-0470-x).

77. D. Peer, J. M. Karp, S. Hong, O. C. FaroKhzad, R. Margalit, R. Langer, Nanocarriers as an emerging platform for cancer therapy. *Nature Nanotechnology* **2**, 751-760 (2007)10.1038/nnano.2007.387).

78. B. Khlebtsov, V. Zharov, A. Melnikov, V. Tuchin, N. Khlebtsov, Optical amplification of photothermal therapy with gold nanoparticles and nanoclusters. *Nanotechnology* **17**, 5167 (2006).

79. N. Khlebtsov, L. Dykman, Biodistribution and toxicity of engineered gold nanoparticles: a review of in vitro and in vivo studies. *Chemical Society reviews* **40**, 1647-1671 (2011).

80. S. R. J. Hirsch L R, Bankson J A, Sershen S R, Rivera B, Price R E, Hazle J D, Halas N J, West J L, Nanoshell-mediated near-infrared thermal therapy of tumors under magnetic resonance guidance. *PNAS* **100**, 13549-13554 (2003); published online EpubNovember 11, 2003 (

81. V. P. Zharov, E. N. Galitovskaya, C. Johnson, T. Kelly, Synergistic enhancement of selective nanophotothermolysis with gold nanoclusters: Potential for cancer therapy. *Lasers in Surgery and Medicine* **37**, 219-226 (2005)10.1002/lsm.20223).

82. H. X. El-Sayed I H, El-Sayed M A, Selective laser photo-thermal therapy of epithelial carcinoma using anti-EGFR antibody conjugated gold nanoparticles. *Cancer Letters* **239**, 129-135 (2005).

83. W. W. F. He X, Crowe J H, Swanlund D J, Bischof J C, In Situ Thermal Denaturation of Proteins in Dunning AT-1 Prostate Cancer Cells: Implication for Hyperthermic Cell Injury. *Annals of Biomedical Engineering* **32**, 1384-1398 (2004); published online EpubOctober 2004 (

84. G. Huttmann, R. Birngruber, On the possibility of high-precision photothermal microeffects and the measurement of fast thermal denaturation of proteins. *Ieee Journal of Selected Topics in Quantum Electronics* **5**, 954-962 (1999).

85. W. Denk, J. H. Strickler, W. W. Webb, Two-photon laser scanning fluorescence microscopy. *Science* **248**, 73 (1990).

86. F. Helmchen, W. Denk, Deep tissue two-photon microscopy. *Nature* **200**, (2002).

87. R. A. Farrer, F. L. Butterfield, V. W. Chen, J. T. Fourkas, Highly efficient multiphoton-absorption-induced luminescence from gold nanoparticles. *Nano Letters* **5**, 1139-1142 (2005).

88. H. Wang, T. B. Huff, D. A. Zweifel, W. He, P. S. Low, A. Wei, J. X. Cheng, In vitro and in vivo two-photon luminescence imaging of single gold nanorods. *Proceedings of the National Academy of Sciences of the United States of America* **102**, 15752 (2005).

89. T. B. Huff, M. N. Hansen, Y. Zhao, J. X. Cheng, A. Wei, Controlling the cellular uptake of gold nanorods. *Langmuir* **23**, 1596-1599 (2007).

90. L. Tong, W. He, Y. Zhang, W. Zheng, J. X. Cheng, Visualizing systemic clearance and cellular level biodistribution of gold nanorods by intrinsic two-photon luminescence. *Langmuir* **25**, 12454-12459 (2009).

91. D. Yelin, D. Oron, S. Thiberge, E. Moses, Y. Silberberg, Multiphoton plasmon-resonance microscopy. *Opt. Express* **11**, 1385–1391 (2003).

92. J. Park, A. Estrada, K. Sharp, K. Sang, J. A. Schwartz, D. K. Smith, C. Coleman, J. D. Payne, B. A. Korgel, A. K. Dunn, J. W. Tunnell, Two-photon-induced photoluminescence imaging of tumors using near-infrared excited gold nanoshells. *Optics Express* **16**, 1590-1599 (2008).

93. J. Park, A. Estrada, J. A. Schwartz, P. Diagaradjane, S. Krishnan, A. K. Dunn, J. W. Tunnell, Intra-Organ Biodistribution of Gold Nanoparticles Using Intrinsic Two-Photon-Induced Photoluminescence. *Lasers in Surgery and Medicine* **42**, 630-639 (2010); published online EpubSep (10.1002/lsm.20935).

94. G. Majno, I. Joris, Apoptosis, oncosis, and necrosis. An overview of cell death. *The American journal of pathology* **146**, 3 (1995).

95. B. E. Trump, I. K. Berezesky, S. H. Chang, P. C. Phelps, The pathways of cell death: oncosis, apoptosis, and necrosis. *Toxicologic pathology* **25**, 82 (1997).

96. C. Szabó, Mechanisms of cell necrosis. *Critical care medicine* **33**, S530-S534 (2005).

97. B. E. Trump, I. K. Berezesky, S. H. Chang, P. C. Phelps, The Pathways of Cell Death: Oncosis, Apoptosis, and Necrosis. *Toxicologic Pathology* **25**, 82-88 (1997)10.1177/019262339702500116).

98. D. R. Green, J. C. Reed, Mitochondria and apoptosis. *Science* **281**, 1309-1312 (1998).

99. J. S. Armstrong, Mitochondria: a target for cancer therapy. *British journal of pharmacology* **147**, 239-248 (2006); published online EpubFeb (10.1038/sj.bjp.0706556).

100. Green, C. John, nbsp, D. R. Reed, Mitochondria and Apoptosis. *Science* **281**, 1309-1312 (1998)10.1126/science.281.5381.1309).

101. I. Budihardjo, H. Oliver, M. Lutter, X. Luo, X. Wang, Biochemical pathways of caspase activation during apoptosis. *Annual review of cell and developmental biology* **15**, 269-290 (1999).

102. A. Degterev, M. Boyce, J. Yuan, A decade of caspases. *Oncogene* **22**, 8543-8567 (2003); published online EpubNov 24 (10.1038/sj.onc.1207107).

103. T. J. Fan, L. H. Han, R. S. Cong, J. Liang, Caspase family proteases and apoptosis. *Acta biochimica et biophysica Sinica* **37**, 719-727 (2005).

104. H. Li, H. Zhu, C. Xu, J. Yuan, Cleavage of BID by caspase 8 mediates the mitochondrial damage in the Fas pathway of apoptosis. *Cell* **94**, 491-501 (1998).

105. A. G. Porter, R. U. Jänicke, Emerging roles of caspase-3 in apoptosis. *Cell death and differentiation* **6**, 99 (1999).

106. M. L. Coleman, E. A. Sahai, M. Yeo, M. Bosch, A. Dewar, M. F. Olson, Membrane blebbing during apoptosis results from caspase-mediated activation of ROCK I. *Nature cell biology* **3**, 339-345 (2001).

107. P. Vandenabeele, L. Galluzzi, T. V. Berghe, G. Kroemer, Molecular mechanisms of necroptosis: an ordered cellular explosion. *Nature Reviews Molecular Cell Biology* **11**, 700-714 (2010).

108. Q. Zhou, J. Zhao, J. G. Stout, R. A. Luhm, T. Wiedmer, P. J. Sims, Molecular cloning of human plasma membrane phospholipid scramblase a protein mediating transbilayer movement of plasma membrane phospholipids. *Journal of Biological Chemistry* **272**, 18240-18244 (1997).

109. S. L. Fink, B. T. Cookson, Apoptosis, pyroptosis, and necrosis: mechanistic description of dead and dying eukaryotic cells. *Infection and immunity* **73**, 1907-1916 (2005).

110. T. Bergsbaken, S. L. Fink, B. T. Cookson, Pyroptosis: host cell death and inflammation. *Nature Reviews Microbiology* **7**, 99-109 (2009).

111. T. V. Berghe, N. Vanlangenakker, E. Parthoens, W. Deckers, M. Devos, N. Festjens, C. Guerin, U. Brunk, W. Declercq, P. Vandenabeele, Necroptosis, necrosis and secondary necrosis converge on similar cellular disintegration features. *Cell Death & Differentiation* **17**, 922-930 (2009).

112. D. E. Christofferson, J. Yuan, Necroptosis as an alternative form of programmed cell death. *Current opinion in cell biology* **22**, 263-268 (2010).

113. L. Galluzzi, G. Kroemer, Necroptosis: a specialized pathway of programmed necrosis. *Cell* **135**, 1161-1163 (2008).

114. T. Idziorek, J. Estaquier, F. De Bels, J.-C. Ameisen, YOPRO-1 permits cytofluorometric analysis of programmed cell death (apoptosis) without interfering with cell viability. *Journal of immunological methods* **185**, 249-258 (1995).

115. H. M. Shapiro, *Practical flow cytometry*. (Wiley. com, 2005).

116. Z. Darzynkiewicz, S. Bruno, G. Del Bino, W. Gorczyca, M. Hotz, P. Lassota, F. Traganos, Features of apoptotic cells measured by flow cytometry. *Cytometry* **13**, 795-808 (1992).

117. C. Dive, C. D. Gregory, D. J. Phipps, D. L. Evans, A. E. Milner, A. H. Wyllie, Analysis and discrimination of necrosis and apoptosis (programmed cell death) by multiparameter flow cytometry. *Biochimica et Biophysica Acta (BBA)-Molecular Cell Research* **1133**, 275-285 (1992).

118. M. A. King, Detection of dead cells and measurement of cell killing by flow cytometry. *Journal of immunological methods* **243**, 155-166 (2000).

119. I. Vermes, C. Haanen, C. Reutelingsperger, Flow cytometry of apoptotic cell death. *Journal of immunological methods* **243**, 167-190 (2000).

120. G. Koopman, C. Reutelingsperger, G. Kuijten, R. Keehnen, S. Pals, M. Van Oers, Annexin V for flow cytometric detection of phosphatidylserine expression on B cells undergoing apoptosis. *Blood* **84**, 1415-1420 (1994).

121. S. Fulda, H. Sieverts, C. Friesen, I. Herr, K.-M. Debatin, The CD95 (APO-1/Fas) system mediates drug-induced apoptosis in neuroblastoma cells. *Cancer research* **57**, 3823-3829 (1997).

122. S. Fulda, W. Wick, M. Weller, K.-M. Debatin, Smac agonists sensitize for Apo2L/TRAIL-or anticancer drug-induced apoptosis and induce regression of malignant glioma in vivo. *Nature medicine* **8**, 808-815 (2002).

123. C. Friesen, I. Herr, P. H. Krammer, K.-M. Debatin, Involvement of the CD95 (APO–1/Fas) receptor/ligand system in drug–induced apoptosis in leukemia cells. *Nature medicine* **2**, 574-577 (1996).

124. R. Hanif, A. Pittas, Y. Feng, M. I. Koutsos, L. Qiao, L. Staiano-Coico, S. I. Shiff, B. Rigas, Effects of nonsteroidal anti-inflammatory drugs on proliferation and on induction of apoptosis in colon cancer cells by a prostaglandin-independent pathway. *Biochemical pharmacology* **52**, 237-245 (1996).

125. R. M. Sutherland, Cell and environment interactions in tumor microregions: the multicell spheroid model. *Science* **240**, 177-184 (1988).

126. J. P. Freyer, R. M. Sutherland, Selective dissociation and characterization of cells from different regions of multicell tumor spheroids. *Cancer research* **40**, 3956-3965 (1980).

127. F. Hirschhaeuser, H. Menne, C. Dittfeld, J. West, W. Mueller-Klieser, L. A. Kunz-Schughart, Multicellular tumor spheroids: an underestimated tool is catching up again. *Journal of biotechnology* **148**, 3-15 (2010); published online EpubJul 1 (10.1016/j.jbiotec.2010.01.012).

128. L. A. Kunz-Schughart, J. P. Freyer, F. Hofstaedter, R. Ebner, The use of 3-D cultures for high-throughput screening: the multicellular spheroid model. *Journal of biomolecular screening* **9**, 273-285 (2004).

129. A. I. Minchinton, I. F. Tannock, Drug penetration in solid tumours. *Nature reviews. Cancer* **6**, 583-592 (2006); published online EpubAug (10.1038/nrc1893).

130. J. Friedrich, C. Seidel, R. Ebner, L. A. Kunz-Schughart, Spheroid-based drug screen: considerations and practical approach. *Nat Protoc* **4**, 309-324 (2009)10.1038/nprot.2008.226).

131. F. Hirschhaeuser, H. Menne, C. Dittfeld, J. West, W. Mueller-Klieser, L. A. Kunz-Schughart, Multicellular tumor spheroids: an underestimated tool is catching up again. *Journal of biotechnology* **148**, 3-15 (2010).

132. A. Ivascu, M. Kubbies, Rapid generation of single-tumor spheroids for high-throughput cell function and toxicity analysis. *Journal of biomolecular screening* **11**, 922-932 (2006); published online EpubDec (10.1177/1087057106292763).

133. A. Ivascu, M. Kubbies, Diversity of cell-mediated adhesions in breast cancer spheroids. *International journal of oncology* **31**, 1403-1413 (2007).

134. J. Friedrich, R. Ebner, L. A. Kunz-Schughart, Experimental anti-tumor therapy in 3-D: spheroids-old hat or new challenge? *Int. J. Radiat. Biol.* **83**, 849-871 (2007).

135. R. Z. Lin, H. Y. Chang, Recent advances in three-dimensional multicellular spheroid culture for biomedical research. *Biotechnology Journal* **3**, 1172-1184 (2008).

136. G. Mehta, A. Y. Hsiao, M. Ingram, G. D. Luker, S. Takayama, Opportunities and challenges for use of tumor spheroids as models to test drug delivery and efficacy. *Journal of controlled release : official journal of the Controlled Release Society* **164**, 192-204 (2012); published online EpubDec 10 (10.1016/j.jconrel.2012.04.045).

137. C. L. Waite, C. M. Roth, Binding and transport of PAMAM-RGD in a tumor spheroid model: the effect of RGD targeting ligand density. *Biotechnology and bioengineering* **108**, 2999-3008 (2011); published online EpubDec (10.1002/bit.23255).

138. C. L. Waite, C. M. Roth, PAMAM-RGD conjugates enhance siRNA delivery through a multicellular spheroid model of malignant glioma. *Bioconjugate Chem.* **20**, 1908-1916 (2009).

139. N. Kohno, T. Ohnuma, P. Truog, Effects of hyaluronidase on doxorubicin penetration into squamous carcinoma multicellular tumor spheroids and its cell lethality. *Journal of cancer research and clinical oncology* **120**, 293-297 (1994).

140. T. T. Goodman, P. L. Olive, S. H. Pun, Increased nanoparticle penetration in collagenase-treated multicellular spheroids. *International journal of nanomedicine* **2**, 265 (2007).

141. G. von Maltzahn, J. H. Park, A. Agrawal, N. K. Bandaru, S. K. Das, M. J. Sailor, S. N. Bhatia, Computationally guided photothermal tumor therapy using long-circulating gold nanorod antennas. *Cancer Research* **69**, 3892 (2009).

142. M. Hu, J. Chen, Z. Y. Li, L. Au, G. V. Hartland, X. Li, M. Marquez, Y. Xia, Gold nanostructures: engineering their plasmonic properties for biomedical applications. *Chemical Society Reviews* **35**, 1084-1094 (2006).

143. F. Y. Cheng, C. T. Chen, C. S. Yeh, Comparative efficiencies of photothermal destruction of malignant cells using antibody-coated silica@ Au nanoshells, hollow Au/Ag nanospheres and Au nanorods. *Nanotechnology* **20**, 425104 (2009).

144. H. H. Richardson, M. T. Carlson, P. J. Tandler, P. Hernandez, A. O. Govorov, Experimental and theoretical studies of light-to-heat conversion and collective heating effects in metal nanoparticle solutions. *Nano Letters* **9**, 1139-1146 (2009).

145. N. R. Jana, L. Gearheart, C. J. Murphy, Wet chemical synthesis of high aspect ratio cylindrical gold nanorods. *Journal of Physical Chemistry B* **105**, 4065-4067 (2001).

146. S. J. Oldenburg, R. D. Averitt, S. L. Westcott, N. J. Halas, Nanoengineering of optical resonances. *Chemical Physics Letters* **288**, 243-247 (1998).

147. P. B. Johnson, R. W. Christy, OPTICAL-CONSTANTS OF NOBLE-METALS. *Physical Review B* **6**, 4370-4379 (1972).

148. C. Maetzler, "MATLAB Functions for Mie Scattering and Absorption," (Institute of Applied Physics, University of Bern, Germany 2002).

149. I. H. Malitson, INTERSPECIMEN COMPARISON OF REFRACTIVE INDEX OF FUSED SILICA. *Journal of the Optical Society of America* **55**, 1205-& (1965).

150. H. J. Vanstaveren, C. J. M. Moes, J. Vanmarle, S. A. Prahl, M. J. C. Vangemert, LIGHT-SCATTERING IN INTRALIPID-10-PERCENT IN THE WAVELENGTH RANGE OF 400-1100 NM. *Applied Optics* **30**, 4507-4514 (1991).

151. W. D. James, L. R. Hirsch, J. L. West, P. D. O'Neal, J. D. Payne, Application of INAA to the build-up and clearance of gold nanoshells in clinical studies in mice. *Journal of Radioanalytical and Nuclear Chemistry* **271**, 455-459 (2007)10.1007/s10967-007-0230-1).

152. R. T. Zaman, P. Diagaradjane, J. C. Wang, J. Schwartz, N. Rajaram, K. L. Gill-Sharp, S. H. Cho, H. G. Rylander, J. D. Payne, S. Krishnan, J. W. Tunnell, In vivo detection of gold nanoshells in tumors using diffuse optical spectroscopy. *Ieee Journal of Selected Topics in Quantum Electronics* **13**, 1715-1720 (2007)10.1109/jstqe.2007.910804).

153. E. D. Palik, HANDBOOK OF OPTICAL-CONSTANTS. *Journal of the Optical Society of America a-Optics Image Science and Vision* **1**, 1297-1297 (1984).

154. J. H. Weaver, C. Krafka, D. W. Lynch, E. E. Koch, Optical properties of metals. *Appl Opt* **20**, (1981); published online Epub1981 Apr (

155. L. Wang, Y. Liu, W. Li, X. Jiang, Y. Ji, X. Wu, L. Xu, Y. Qiu, K. Zhao, T. Wei, Y. Li, Y. Zhao, C. Chen, Selective targeting of gold nanorods at the mitochondria of cancer cells: implications for cancer therapy. *Nano Lett* **11**, 772-780 (2011); published online EpubFeb 9 (10.1021/nl103992v).

156. J. L. Li, M. Gu, Surface plasmonic gold nanorods for enhanced two-photon microscopic imaging and apoptosis induction of cancer cells. *Biomaterials* **31**, 9492-9498 (2010); published online EpubDec (10.1016/j.biomaterials.2010.08.068).

157. B. a. E.-S. Nikoobakht, MA, Preparation and Growth Mechanism of Gold Nanorods (NRs) using Seed-Mediated Growth Method. *Chemistry of Materials* **15**, 1957-1962 (2003).

158. J. Lee, G. D. Lilly, R. C. Doty, P. Podsiadlo, N. A. Kotov, In vitro toxicity testing of nanoparticles in 3D cell culture. *Small* **5**, 1213-1221 (2009); published online EpubMay (10.1002/smll.200801788).

159. T. T. Goodman, J. Chen, K. Matveev, S. H. Pun, Spatio-temporal modeling of nanoparticle delivery to multicellular tumor spheroids. *Biotechnology and bioengineering* **101**, 388-399 (2008); published online EpubOct 1 (10.1002/bit.21910).

160. K. Huang, H. Ma, J. Liu, S. Huo, A. Kumar, T. Wei, X. Zhang, S. Jin, Y. Gan, P. C. Wang, Size-dependent localization and penetration of ultrasmall gold nanoparticles in cancer cells, multicellular spheroids, and tumors in vivo. *ACS nano* **6**, 4483-4493 (2012).

161. H.-l. Ma, Q. Jiang, S. Han, Y. Wu, J. Cui Tomshine, D. Wang, Y. Gan, G. Zou, X.-J. Liang, Multicellular tumor spheroids as an in vivo-like tumor model for three-dimensional imaging of chemotherapeutic and nano material cellular penetration. *Molecular imaging* **11**, 487 (2012).

162. T.-H. Kim, C. W. Mount, W. R. Gombotz, S. H. Pun, The delivery of doxorubicin to 3-D multicellular spheroids and tumors in a murine xenograft model using tumor-penetrating triblock polymeric micelles. *Biomaterials* **31**, 7386-7397 (2010).

163. S. K. Baek, A. R. Makkouk, T. Krasieva, C. H. Sun, S. J. Madsen, H. Hirschberg, Photothermal treatment of glioma; an in vitro study of macrophage-mediated delivery of gold nanoshells. *Journal of neuro-oncology* **104**, 439-448 (2011); published online EpubSep (10.1007/s11060-010-0511-3).

164. M.-R. Choi, K. J. Stanton-Maxey, J. K. Stanley, C. S. Levin, R. Bardhan, D. Akin, S. Badve, J. Sturgis, J. P. Robinson, R. Bashir, A cellular Trojan Horse for delivery of therapeutic nanoparticles into tumors. *Nano letters* **7**, 3759-3765 (2007).

165. S. Jin, X. Ma, H. Ma, K. Zheng, J. Liu, S. Hou, J. Meng, P. C. Wang, X. Wu, X. J. Liang, Surface chemistry-mediated penetration and gold nanorod thermotherapy in multicellular tumor spheroids. *Nanoscale* **5**, 143-146 (2013); published online EpubJan 7 (10.1039/c2nr31877f).

166. M. W. Dewhirst, B. L. Viglianti, M. Lora-Michiels, M. Hanson, P. J. Hoopes, Basic principles of thermal dosimetry and thermal thresholds for tissue damage from hyperthermia. *Int. J. Hyperthermia* **19**, 267-294 (2003); published online EpubMay-Jun (10.1080/0265673031000119006).

167. J. R. Lepock, Cellular effects of hyperthermia: relevance to the minimum dose for thermal damage. *International journal of hyperthermia : the official journal of European Society for Hyperthermic Oncology, North American Hyperthermia Group* **19**, 252-266 (2003); published online EpubMay-Jun (10.1080/0265673031000065042).

168. Y. Sakaguchi, L. C. Stephens, M. Makino, T. Kaneko, F. R. Strebel, L. L. Danhauser, G. N. Jenkins, J. M. Bull, Apoptosis in tumors and normal tissues induced by whole body hyperthermia in rats. *Cancer research* **55**, 5459-5464 (1995).

169. S. Bhowmick, J. E. Coad, D. J. Swanlund, J. C. Bischof, In vitro thermal therapy of AT-1 Dunning prostate tumours. *Int. J. Hyperthermia* **20**, 73-92 (2004); published online EpubFeb (10.1080/0265673031000111932).

170. B. Harmon, A. Corder, R. Collins, G. Gobe, J. Allen, D. Allan, J. Kerr, Cell death induced in a murine mastocytoma by 42-47 C heating in vitro: evidence that the form of death changes from apoptosis to necrosis above a critical heat load. *Int. J. Radiat. Biol.* **58**, 845-858 (1990).

171. B. V. Harmon, Y. S. Takano, C. M. Winterford, G. C. Gobe, THE ROLE OF APOPTOSIS IN THE RESPONSE OF CELLS AND TUMORS TO MILD

HYPERTHERMIA. *Int. J. Radiat. Biol.* **59**, 489-501 (1991); published online EpubFeb (10.1080/09553009114550441).

172. T. Walker, P. Rhodes, C. Westmoreland, The differential cytotoxicity of methotrexate in rat hepatocyte monolayer and spheroid cultures. *Toxicology in vitro* **14**, 475-485 (2000).

173. J. Dahm-Daphi, I. Brammer, E. Dikomey, Heat effects on the repair of DNA double-strand breaks in CHO cells. *Int. J. Radiat. Biol.* **72**, 171 (1997).

174. J. R. Lepock, Involvement of membranes in cellular responses to hyperthermia. *Radiation Research* **92**, 433-438 (1982).

175. A. Konings, A. Ruifrok, Role of membrane lipids and membrane fluidity in thermosensitivity and thermotolerance of mammalian cells. *Radiat. Res* **102**, 86-98 (1985).

176. C. A. Vidair, W. C. Dewey, Evaluation of a Role for IntracellularNa+, K+, Ca2+, and Mg2+ in Hyperthermic Cell Killing. *Radiation Research* **105**, 187-200 (1986).

177. T. Nishida, K. Akagi, Y. Tanaka, Correlation between cell killing effect and cell membrane potential after heat treatment: analysis using fluorescent dye and flow cytometry. *International Journal of Hyperthermia* **13**, 227-234 (1997).

178. A. Malhotra, M. L. P. Heynen, J. R. Lepock, Role of extracellular calcium in the hyperthermic killing of CHL V79 cells. *Radiation Research* **112**, 478-489 (1987).

179. J. R. Lepock, Protein denaturation during heat shock. *Advances in Molecular and Cell Biology* **19**, 223-259 (1997).

180. J. R. Lepock, Measurement of protein stability and protein denaturation in cells using differential scanning calorimetry. *Methods* **35**, 117-125 (2005).

181. M. E. Feder, G. E. Hofmann, Heat-shock proteins, molecular chaperones, and the stress response: evolutionary and ecological physiology. *Annual Review of Physiology* **61**, 243-282 (1999).

182. J. Becker, E. A. CRAIG, Heat-shock proteins as molecular chaperones. *European Journal of Biochemistry* **219**, 11-23 (1994).

183. M. Jäättelä, Heat shock proteins as cellular lifeguards. *Annals of medicine* **31**, 261-271 (1999).

184. J. T. Beckham, M. A. Mackanos, C. Crooke, T. Takahashl, C. O'Connell-Rodwell, C. H. Contag, E. D. Jansen, Assessment of Cellular Response to Thermal Laser Injury Through Bioluminescence Imaging of Heat Shock Protein 70¶†. *Photochemistry and Photobiology* **79**, 76-85 (2004).

185. J. A. Pearce, Comparative analysis of mathematical models of cell death and thermal damage processes. *Int. J. Hyperthermia* **29**, 262-280 (2013).

Vita

The author, Varun Pattani, was born in Vancouver, Canada to Paresh and Kalyani Pattani as they were working towards their respective degrees at UBC. After one year, Varun moved with his family to Austin, TX where he stayed for two years until his family moved to The Woodlands, TX where he attended Elementary and Middle School at The John Cooper School. He moved with his family to Beaverton, OR and attended high school at a magnet school, the School of Science and Technology. After high school, the author attended Cornell University in Ithaca, NY where he obtained an Electrical and Computer Engineering undergraduate degree. During the summers of his undergraduate degree, the author held positions in BME research at the Oregon Health Sciences University working for Dr. Tania Vu and in industry at Intel, Corp working in the chip architecture design team. After his undergraduate degree, the author joined the University of Texas at Austin in Biomedical Engineering and received his M.S.E. degree. The author has continued his Ph.D. while conducting research for his advisor, Dr. James Tunnell, focusing on utilizing gold nanoparticles for cancer imaging and therapy and understanding the cellular response.

Permanent email address: varun.pattani@utexas.edu

This dissertation was typed by Varun Pattani.